Bachelorarbeit

Gas Gain Calibration of an ALICE TRD Supermodule Using Cosmic Rays

vorgelegt von

Christian Wittweg

Westfälische Wilhelms-Universität Münster
Institut für Kernphysik

- Juni 2014 -

Erster Gutachter: Prof. Dr. J. P. Wessels
Zweiter Gutachter: Prof. Dr. C. Weinheimer

Contents

1 Introduction 1

2 Theoretical Background and Experimental Environment 3
- 2.1 Quark-Gluon Plasma . . . 3
- 2.2 ALICE at LHC . . . 6
  - 2.2.1 The Large Hadron Collider . . . 6
  - 2.2.2 The ALICE Detector . . . 8

3 The ALICE Transition Radiation Detector 11
- 3.1 Transition Radiation . . . 11
- 3.2 Design of the TRD . . . 12
  - 3.2.1 Readout Chambers . . . 12
  - 3.2.2 Signal Generation in the ROCs . . . 13
  - 3.2.3 Gas Gain in Multi-Wire Proportional Chambers . . . 15
  - 3.2.4 Electronics . . . 18
- 3.3 Calibration Parameters and Motivation for Gain Calibration . . . 19

4 Cosmic Rays and the Experimental Setup in Münster 21
- 4.1 Primary Cosmic Radiation . . . 21
- 4.2 Secondary Cosmic Radiation . . . 22
- 4.3 Experimental Setup in Münster . . . 23
- 4.4 Trigger Configuration . . . 25
- 4.5 Data Acquisition . . . 29

5 Run Reconstruction and Supermodule Calibration with AliRoot 33
- 5.1 The Offline Conditions Database . . . 33
- 5.2 TRD Data Reconstruction . . . 34
  - 5.2.1 Reconstruction Parameters . . . 34
- 5.3 Drift Velocity Calibration . . . 35
  - 5.3.1 Granularity settings . . . 35
  - 5.3.2 Determination of the Drift Velocity . . . 36
- 5.4 Gain Calibration . . . 38
  - 5.4.1 Filling of the Energy Loss Spectra . . . 38
  - 5.4.2 Determination of the Relative Gain Factors . . . 39
- 5.5 Execution of the Calibration Procedure . . . 40
  - 5.5.1 Pass 0 Reconstruction . . . 40
  - 5.5.2 Drift Velocity . . . 41
  - 5.5.3 Pass 1 Reconstruction . . . 41

5.5.4 Gain 42
5.6 Modifications of AliRoot v5-04-Rev-18 42
5.6.1 Custom OCDBs 42
5.6.2 Changes in AliRoot Classes 42

6 Gain Calibration of the TRD Supermodule 45
6.1 Determination of the Relative Gain Factors 45
6.1.1 Comparison with Previous Measurements 47
6.2 Accuracy of the Calibration Procedure 48
6.3 Gain Results for Different Reconstruction Parameters 49
6.4 Anode Voltage Influence on Relative Gain Factors 51
6.4.1 Measurement of Gain Factors for Different Anode Voltages 51
6.4.2 Results 51
6.4.3 Investigation of Exponential Behavior 54
6.4.4 Comparison with Previous Measurements 54
6.5 Determination of the Drift Velocity 56

7 Summary and Conclusion 59

8 Appendix 61
8.1 List of Abbreviations 61
8.2 ALICE Coordinate Systems 63
8.3 List of Supermodule Runs 65
8.4 Gain Calibration Results 66
8.5 Drift Velocity Results 77

9 Bibliography 81

1 Introduction

A Large Ion Collider Experiment (ALICE) is one of the four major experiments at the Large Hadron Collider at the European Organization for Nuclear Research (CERN) in Geneva, Switzerland. It is dedicated to the exploration of an extreme state of matter, the Quark-Gluon plasma. Usually quarks are confined in color-neutral states, but can become deconfined under conditions which have prevailed shortly after the big bang or may still be present in neutron stars. In the laboratory such conditions are recreated by means of heavy ion collisions at high energies.
ALICE is comprised of a set of subdetectors. One of these is the Transition Radiation Detector (TRD) which is assembled and tested at the Institute of Nuclear Physics in Münster. The main tasks of the TRD are electron identification, charged particle tracking and providing a fast trigger on electrons and jets. It is an assembly of 18 supermodules, each containg 30 multi-wire proportional chambers. A charged particle traversing the chambers with a given momentum should generate the same signal in every chamber in order to provide reliable particle identification. However, the amplification of the signal is not identical among the chambers. Differences in the so-called *gain* are mainly determined by the gas amplification in the TRD chambers and the signal amplification of the readout electronics.
Gain differences within the TRD can be corrected by software and by adjustments of the applied anode voltage in the chambers. In this thesis the relative gain in the TRD is examined using cosmic rays as a particle source. The relative gain can be used to calibrate the TRD to a homogenous signal amplification. This is done with a calibration software framework that has been applied in previous calibration activities, of which the latest was completed four years ago. Considering the long hiatus from calibration activities, an extensive part of this thesis deals with the recomissioning of both the analysis software and the cosmic rays trigger hardware. This is done in the interest of providing an accessible framework for future calibration efforts.

The following chapter provides a short overview of the theoretical background and experimental environment of the ALICE experiment. Chapter 3 contains a detailed description of the design and working principle of the TRD. Chapter 4 describes the restart and configuration of the Cosmic Trigger for data acquisition preceded by a brief introduction to cosmic radiation. The reconstruction and calibration software is introduced in chapter 5, where programs, procedures and algorithms are set forth. The actual gain calibration is treated in chapter 6. In addition to the gain results at standard settings, the relative gain's dependence on anode voltage, and the influence reconstruction filters on the gain results are investigated. A summary of the results and a conclusion of this work are given in chapter 7.

2 Theoretical Background and Experimental Environment

This section is intended to provide a short overview of the Large Hadron Collider (LHC) and the associated experiments at CERN[1]. A focus is put on the scientific objectives of the ALICE experiment, with the study of the Quark-Gluon Plasma being the main field of interest.

2.1 Quark-Gluon Plasma

According to the standard model of particle physics [PRSZ09] all matter in the universe is composed of six quarks and six leptons, each group segmented into three generations depicted in figure 2.1.

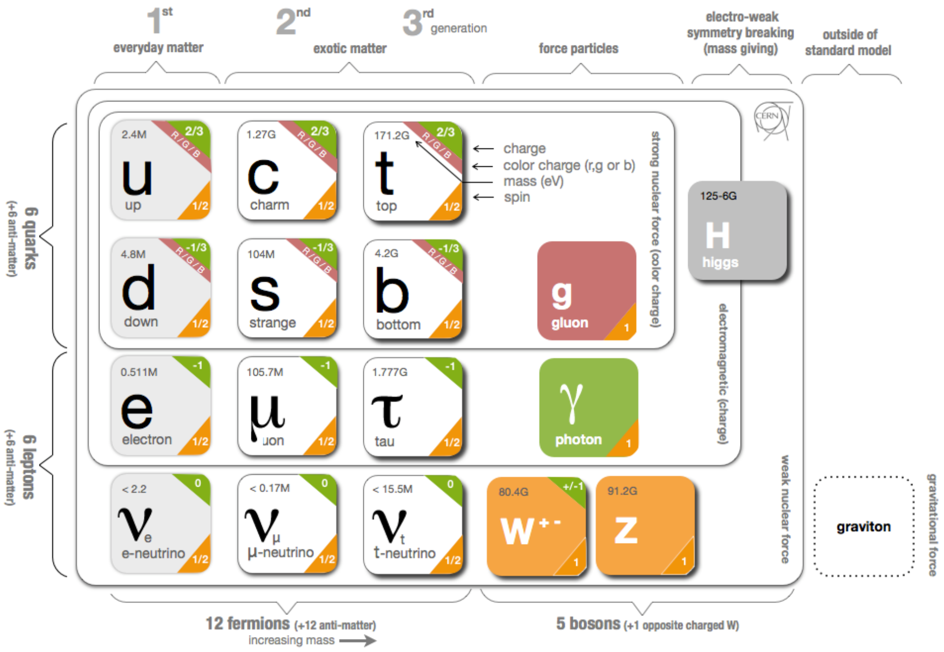

Figure 2.1: Quarks, leptons and bosons with their mass, electric and color charge according to the standard model of particle physics [CERN13].

The forces between these elementary particles are mediated by gauge bosons. The electromagnetic interaction between electrically charged particles is mediated by photons and described by Quantum Electrodynamics (QED). In analogy to this Quantum Chromodynamics was developed in order to characterize the strong interaction between quarks

---

[1] Conseil Européen pour la Recherche Nucléaire (European Organization for Nuclear Research.

mediated by gluons. Both quarks and gluons carry a color charge which was introduced to prevent a violation of the Pauli exclusion principle by the spin 1/2 quarks. To this day free quarks have never been observed. This has lead to the postulate that quarks only exist in color neutral bound states, i.e. the additive mixture of the quarks' color charges either consists of three different colors (baryons) or color and anti-color (mesons). This is due to the fact that the gauge bosons of the strong interaction, the gluons, carry a color/anti-color charge themselves and, therefore, do not only interact with quarks, but with other gluons as well. The potential $V(r)$ between two quarks can be described by [KBö04]:

$$V(r) = -\frac{4}{3}\frac{\alpha_s}{r} + kr. \tag{2.1}$$

Here α_s is the coupling constant of the strong interaction which depends on the momentum transfer Q^2:

$$\alpha_s(Q^2) \approx \frac{12\pi}{(33 - 2n_f) \cdot \ln\left[(Q/\Lambda)^2\right]}. \tag{2.2}$$

In this equation n_f denotes the number of flavors and Λ is the QCD scale parameter which can be determined experimentally. With decreasing momentum transfer, which translates to increasing distances, the coupling constant rises. The resulting strong coupling of the quarks is called confinement. For shorter distances and increasing momentum transfer the coupling constant decreases causing the quarks to behave as quasi-free particles. This is called asymptotic freedom.

QCD predicts a phase transition of nuclear matter, quarks and gluons in bound states, at high temperatures or high baryon densities where confinement is overridden: the quark-gluon plasma (QGP) [ALI04].

The phase transition to a quark-gluon plasma is depicted in figure 2.2. At Baryon densities below a critical point and at high temperatures the medium is expected to undergo a transition through a crossover phase where deconfined quarks and hadrons might coexist. Above the critical point the transition is of first or second order and the system absorbs energy without an increase in temperature [ALI04] [KBö04].

The conditions under which a quark-gluon plasma can form are presumed to have existed shortly after the big bang and may still exist in neutron stars. In the laboratory such conditions are created in heavy ion collisions in particle accelerators like the Relativistic Heavy Ion Collider (RHIC) at Brookhaven National Laboratory, the Facility for Antiproton and Ion Research (FAIR, currently under construction) at GSI[2] in Darmstadt, and the LHC at CERN [ALI04].

---

[2] GSI Helmholtzzentrum für Schwerionenforschung.

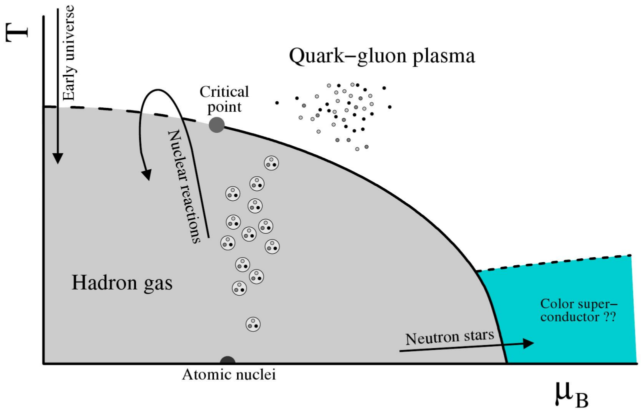

Figure 2.2: QCD phase diagram with temperature T and baryochemic potential μ_b which is a measure for the net baryon density. The net baryon density is the difference between the number of baryons and anti-baryons in a system. The solid line depicts a phase transition of first order, the dashed line at low μ_b marks a crossover phase. The other dashed line at high baryon densities signifies a hypothetical transition to a color superconducting phase [KBö04].

Heavy nuclei (Au at RHIC, Pb at LHC) are collided at relativistic speeds creating a QGP. After the collision the system expands and cools down. Upon reaching a certain temperature a transition from QGP to a hot hadron gas takes place. The energy of the formerly free partons is converted into newly created hadrons and their kinetic energy (freeze-out). Due to the lack of an unambiguous observable the QGP cannot be directly detected. All evidence for the creation of a QGP has to be extracted from the final hadronic state which carries several signatures for its existence described in detail in [KBö04] and [ALI04]. These include:

- J/Ψ suppression: In heavy-ion collisions pairs of charm (c) and anti-charm ($\bar{c}$) quarks are produced. These can form a bound $c\bar{c}$ state, the J/Ψ particle, or combine with more abundant light quarks. It has been found that in heavy ion collisions at RHIC energies the production of J/Ψ mesons is suppressed[3]. It has been suggested that this suppression is a signature of the QGP. The c and $\bar{c}$ quarks are screened by the color charge of the surrounding medium in the QGP phase making them more likely to form D mesons upon hadronization. ALICE measurements of the inclusive J/Ψ production in Pb-Pb collisions at $\sqrt{s_{\mathrm{NN}}} = 2.76$ TeV[4] down to zero transverse momentum in the rapidity range $2.5 < \eta < 4$ have found such a suppression [ALI12].
- Enhanced production of strange quarks: For the creation of a $s\bar{s}$ pair in the QGP phase only the current quark mass of approximately 300 MeV/c^2 is needed. By contrast, in the associated production of strange particles in a hadron gas the larger constituent quark mass of the strange quark becomes important. Therefore, higher energies are needed. The effect should be directly visible in the enhanced production rate of strange particles compared to proton-proton collisions.

---

[3] The production of c and $\bar{c}$ quarks in heavy ion collisions has been compared to the yield in proton-proton (p-p) collisions. The number of produced J/Ψ in p-p collisions is scaled with the number of nucleus-nucleus collisions within a heavy ion collision.

[4] Center of mass energy per nucleon pair.

- Direct photons: Photons which are not produced in decays but directly in the collision are called direct photons. They do not interact strongly and may therefore escape without further interaction carrying unaltered information about the medium they originated from. Direct photons are subdivided into prompt photons from the initial hard scatterings and thermal photons from the QGP phase.
- Jet quenching: In parton-parton collisions high p_{T} partons[5] are created at the early stage of the collision. These partons freeze-out into hadrons which are emitted in a narrow cone, a jet. The higher the parton energy, the more hadrons are formed. Partons that traverse the medium created in the collision have a certain probability of interacting with other partons. The consequent energy loss results in a suppresion of high p_{T} hadrons compared to the jets that have not crossed the medium. The jet structure is also modified. This jet quenching can be used to study the properties of the medium created in the collision.

2.2 ALICE at LHC

The ALICE experiment [ALI08] studies the QCD phase diagram at energy densities of about 1000 GeVfm^{-3} with a particular emphasis on the QGP phase. Accordingly, the ALICE detector has been designed in order to detect, observe and investigate the aforementioned signatures of the QGP. Built as a general purpose heavy-ion detector, it is able to measure, track and identify mid-rapidity photons, leptons and hadrons created in p-p, p-Pb and Pb-Pb collisions. The ALICE detector is located at the instersection point 2 in St. Genis-Pouilly, France. Its location within the LHC is depicted in figure 2.3.

2.2.1 The Large Hadron Collider

The Large Hadron Collider (LHC) [LHC08a] is the world's largest and highest energy particle accelerator located at CERN near Geneva. The synchrotron has been fitted into the already existing underground tunnel formerly used by the Large Electron Positron Collider (LEP) with a circumference of 27 km. In two beam pipes protons or ions are accelerated in opposite directions and kept in their circular motion by 9539 superconducting magnets. The final kinetic energy for protons is 7 TeV. At four interaction points the particles can be collided with a center of mass energy of 5.5 TeV per nucleon pair for lead ions and 14 TeV per proton pair. The luminosity design values are 10^{27} cm^{-2} s^{-1} for lead ions and 10^{34} cm^{-2} s^{-1} for protons.
The LHC has been shut down since February 14, 2013 and is scheduled to resume operation in 2015. In this first long shutdown period, the LS1, infrastructure is modernized and the LHC is prepared for operation at its nominal design energies. This includes the consolidation of connections between the magnets and the replacement of dipole magnets [CERNPub]. The LS1 is also used for upgrades and the ongoing assembly of the detectors.

---

[5] The transversal impulse p_{T} is the particle impulse perpendicular to the beam direction.

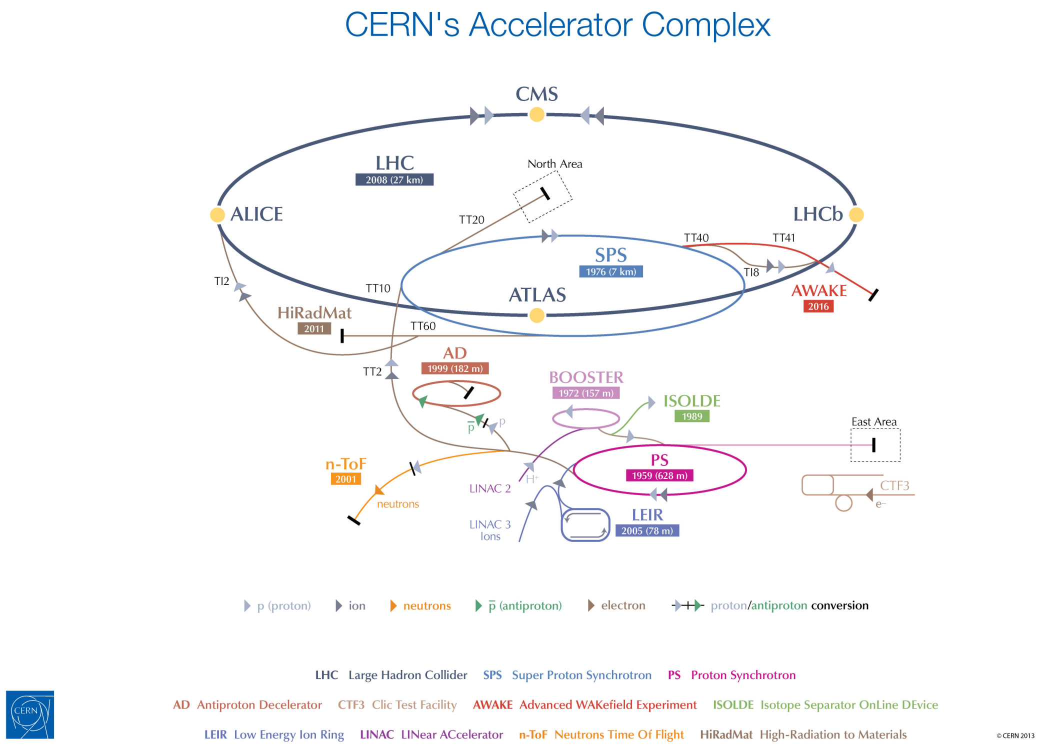

Figure 2.3: The CERN accelerator complex [CERN13].

The experiments at the LHC are installed at the four intersection points depicted in figure 2.3. These are A Large Ion Collider Experiment (ALICE), A Toroidal LHC Apparatus (ATLAS), the Compact Muon Solenoid (CMS) and the Large Hadron Collider beauty (LHCb) experiment, the Large Hadron Collider forward (LHCf) experiment near ATLAS, and the Total Elastic and Diffractive Cross Section Measurement (TOTEM) experiment at the CMS intersection point:

- ALICE is aimed at the study of the quark-gluon plasma utilizing heavy ion collisions. It is presented in greater detail in the next section.
- The main objective of ATLAS and CMS is the search for the Higgs Boson. Both experiments use different physical approarches [LHC08b] [LHC08c].
- The focus of LHCb is directed at the investigation of CP violation and the interaction of hadrons containing beauty quarks [LHC08d].
- LHCf explores neutral particle production in the forward direction in p-p collisions. Additionally, it will test models describing the primary energy of ultra-high energy cosmic rays [LHC08e].
- The TOTEM detector measures elastic scattering, diffractive processes and the cross section of p-p collisions [LHC08f].

2.2.2 The ALICE Detector

A cross section of the ALICE detector [ALI01] [ALI08] with its subdetectors, absorbers and magnets is protrayed in figure 2.4. The entire detector system is 25 m long, 16 m high and has an overall mass of 10,000 t. The subdetectors are organized in three groups: the forward detectors, muon spectrometer (right) and central barrel (inside the red L3 magnet).

The L3 magnet was originally constructed for the L3 experiment at the Large Electron-Positron Collider (LEP). It is the largest dipole magnet ever built and delivers a maximum field strength of about 0.5 T. The central barrel detectors are encased within the magnet and cylindracally arranged around the intersection point.

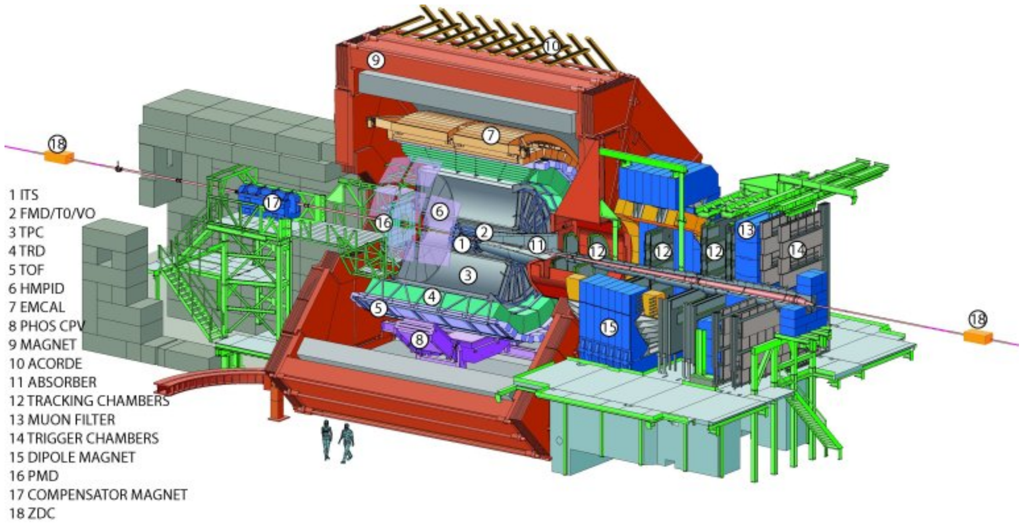

Figure 2.4: The ALICE experiment with its subdetectors [AliPub].

Starting at the intersection point and going outward the subdetectors in the central barrel are the Inner Tracking System (ITS), the Time Projection Chamber (TPC), the Transition Radiation Detector (TRD), the Time of Flight (TOF), the High Momentrum Particle Identification Detector (HMPID), The Photon Spectrometer (PHOS) and the Electromagnetic Calorimeter (EMCAL):

- The ITS consists of six layers of high resolution silicon detectors in three groups: two silicon pixel, two silicon drift and two silicon strip detectors. It is used for precise track finding and detection of the primary vertex. Secondary vertex reconstruction is also performed with the ITS.

- The TPC is the main tracking device in ALICE. It consists of a cylindrical field cage which is read out by multi-wire proportional chambers. It contributes to particle identification, vertex finding, determination of the event plane and track reconstruction.

- The main task of the TRD is electron identification at momenta larger than 2 GeV/c and fast triggering on high p_T particles. It also serves as a tracking device. A detailed description of the TRD is provided in the next chapter.

- The TOF is based on a multi-gap resistive plate chamber detector. Its purpose is particle identification for momenta between 0.3 GeV/c - 3.5 Gev/c.
- The HMPID consists of an array of ring imaging Cherenkov detectors. It can discriminate pions from kaons (kaons from protons) at momenta of up to 3 GeV/c (5 GeV/c).
- The PHOS is a high granularity, high resolution electomagnetic spectrometer consisiting of a charged particle veto detector, an electromagnetic calorimeter and arrays of high-density crystals. Within its limited acceptance range PHOS provides identification of electrons, neutral mesons and photons, including direct photons.
- The EMCAL is a layered lead-scintillator sampling calorimeter. It provides a fast trigger on high energy jets and reduces the measurement bias of jet quenching. A detection of high energy photons and high p_{T} photons is also possible.

3 The ALICE Transition Radiation Detector

The ALICE Transition Radiation Detector (TRD) [AW11] [ALI08] is a gaseous detector capable of detecting charged particles and using transition radiation generated by the former for particle identification. It was introduced to the ALICE experiment for two main tasks: First, it provides efficient electron identification in the central detector barrel for momenta above 1 GeV/c. For $p_t > 3$ GeV a pion rejection factor of 100 is achieved. Second, the TRD is able to provide a fast trigger for charged particles with high momenta, owed to its inherent tracking capability. With the facility of having trigger decisions for electron/positron-pairs with p_{T} above 2 GeV within 6.5 µs, a study of J/Ψ, Υ mesons and jets is possible. Combining particle identification (PID) data from the TRD, ITS and TPC a study of the production of light and heavy vector-mesons and an investigation of the dilepton continuum is possible both in proton-proton and Pb-Pb collisions.

3.1 Transition Radiation

A charged particle crossing the interface between two materials with different dielectric constants can produce transition radiation. This generation of photons can be explained in the model of mirror charges. A particle traveling in a medium of the dielectric number ϵ_1 towards a medium with ϵ_2 causes an electric polarisation in the second medium. It induces a mirror charge. Both charges form a dipole with a changing field strength that ultimately disappears at the boundary [Sch98]. This changing dipole emits radiation with the probability for transition radiation increasing with the Lorentz factor $\gamma = \frac{E}{m_0 c}$. Therefore, the lighter one of two charged particles with the same momentum is more likely to generate transition radiation. This is used in the ALICE TRD to distinguish pions ($m_0 = 139.570$ MeV) from electrons ($m_0 = 0.511$ MeV) [PDG13b].
The TRD can detect transition radiation for relativistic particles with $\gamma \geq 1000$ with radiation energies in the x-ray realm. The spectral dependency of transition radiation is given by [AW11]:

$$\frac{d^2W}{d\omega d\Omega} = \frac{\alpha}{\pi^2} \cdot \left(\frac{\theta}{\gamma^{-2} + \theta^2 + \xi_1^2} - \frac{\theta}{\gamma^{-2} + \theta^2 + \xi_2^2} \right)^2 . \tag{3.1}$$

Here W and ω denote the intensity and frequency of the emitted radiation, $\alpha = 1/137$ is the fine structure constant. The angle of the emission with respect to the particle trajectory is given by θ. $\xi_{1/2}$ are functions of the plasma frequencies $\omega_{1/2}$ of the two different media with $\xi_{1/2} = \frac{\omega_{1/2}^2}{\omega^2} \ll 1$.
The predominant amout of photons is emitted in a cone with the opening angle $1/\gamma$ with

respect to the particle trajectory. The overall emitted radiation intensity upon crossing a single surface is roughly proportional to γ [ESA00]:

$$W = \frac{\alpha\hbar}{\pi} \cdot \frac{(\omega_1 - \omega_2)^2}{\omega_1 + \omega_2} \cdot \gamma. \tag{3.2}$$

3.2 Design of the TRD

The TRD [ALI08] is located between the TPC and TOF. The detector has a mass of about 30 tons and is segmented into 18 supermodules (SMs) which are supported by the so-called spaceframe. The TRD covers the full azimuth and a pseudorapidity[1] range of $|\eta| \leq 0.9$. Each supermodule consists of 6 (0, 1, 2, 3, 4, 5) layers of readout chambers (ROCs) in radial direction which are segmented into 5 stacks (0, 1, 2, 3, 4) in beam direction. Altogether the TRD comprises 522 readout chambers with stack 2 left out in three supermodules (sectors 13, 14, 15) in order to minimize radiation length in front of PHOS [ALI01]. The final design of the TRD is depicted in figure 3.1.

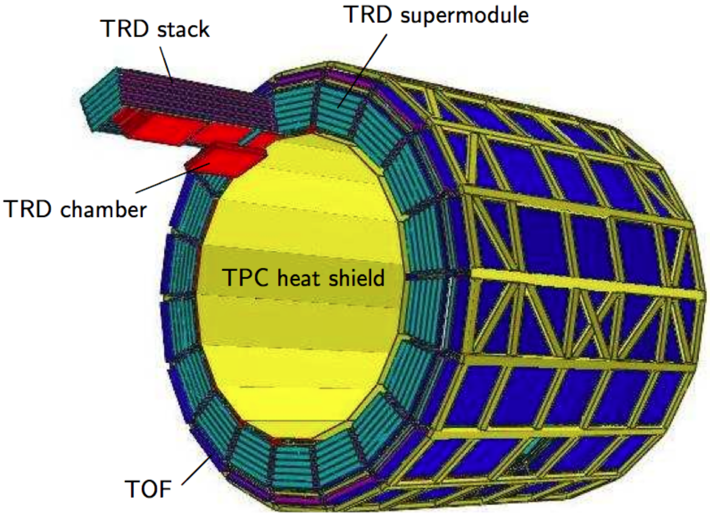

Figure 3.1: Schematic drawing of the ALICE TRD [ALI08].

The active length in longitudinal direction is 7 m, with an overall length of 7.8 m and a mass of 1.7 tons for each SM.

3.2.1 Readout Chambers

Each readout chamber consists of three main parts: A multi-wire proportional drift chamber, a radiator and the readout electronics.

The radiators consist of polypropylene fiber mats of 32 mm thickness sandwiched between two Rohacell plates adding 16 mm in thickness. The multi-wire proportional chamber is installed on top of the radiator and consists of a 30 mm drift region right after the radiator

---

[1] In particle physics the pseudorapidity $\eta = -\ln(\tan(\theta/2))$ is used to measure the angle of an emerging particle jet with respect to the beam axis. Here θ denotes the center of mass scattering angle of the particles. It is Lorentz-invariant under longitudinal boosts and, in hadron-hadron collisions, the particle flux in different pseudorapidity intervals is roughly equal [Bet12].

and a 7 mm amplification region. The design of a chamber is shown in figure 3.2. In the final ALICE configuration the chambers are filled with a Xe/CO_2 (85/15) mixture. The drift cathode is set to -2.1 kV. The drift and amplification region are divided by a grounded cathode wire plane providing a homogenous electric drift field. The anode wires are centered between the readout pads and cathode wires, and set to a potential of 1.5 kV. The SM setup for testing in Münster is different from the one in ALICE regarding voltages and gas mixture, and is presented in chapter 4.3.

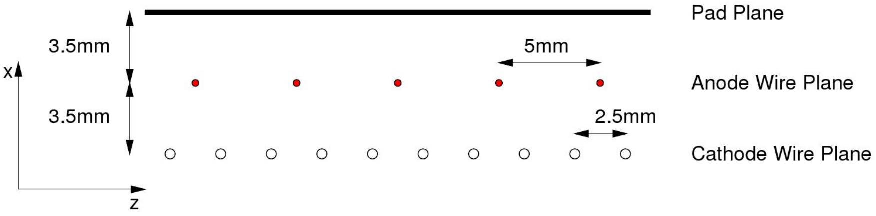

Figure 3.2: Geometry of a readout chamber with respect to local tracking coordinates (see section 8.1) [ALI01].

The readout pads in the direction parallel to the beam axis (z-direction) are larger than in the perpendicular direction (y-axis). This design decision is based on the desired momentum resolution (bending direction) and the capability to identify and track electrons throughout the detector (longitudinal direction) [AW11]. The watercooled readout electronics are mounted atop the chambers.

Due to the shape of the SMs the length and width of the chambers increase from layer 0 to 5, with stack 2 being the exception. Here the chambers only vary in width between 922 mm to 1144 mm. The length in the other stacks varies between 1220 mm and 1450 mm. The number of readout channels in the stack 2's C0 chambers is smaller than in the other stacks' C1 chambers [ALI01].

3.2.2 Signal Generation in the ROCs

A charged particle crossing the chambers ionizes gas atoms along its way creating primary electron clusters and gas ions. These charge carriers move along the lines of the 700 V/cm drift field: electrons to the anode wires and ions to the cathode pads. Due to the homogenous field in the drift region the electrons are expected to drift at a constant velocity of around 1.5 cm/µs. Upon entering the amplification region they are accelerated towards the anode wires gaining enough energy in order to cause an electron avalanche. As those electrons are created in the vicinity of the anode wires they are collected in less than a nanosecond [ALI01]. By reason of their larger mass the gas ions drift slower than the electrons. Therefore, they remain around the anode wire for a longer time forming a space charge which lowers the gas gain. As the electrons are created close to the anode wire, their contribution to the overall signal is much smaller than that of the ions.

Figure 3.3 illustrates the signals generated by charged particles traversing the detector:

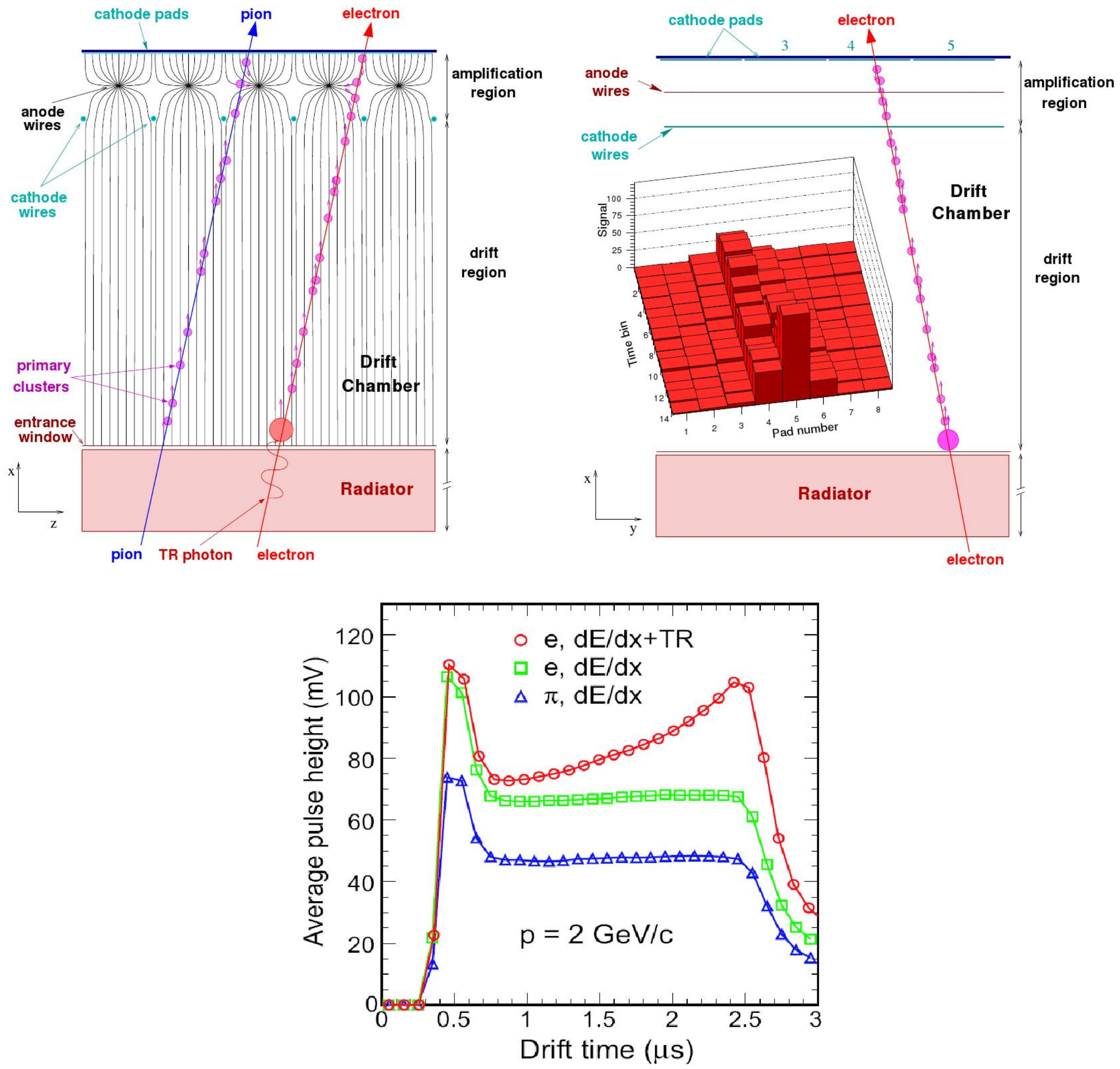

Figure 3.3: Top left: Cross section of a readout chamber crossed by a pion and an electron (with transition radiation) in local tracking coordinates. Top right: Illustration of the resulting signal over 14 timebins and 8 different cathode pads of one readout chamber. Bottom: Average pulse height as a function of drift time for electrons with transition radiation (red), electrons without transition radiation (green) and pions (blue) [ALI08].

The top left panel shows an electron and a pion with the same impulse $p = 2$ GeV$/c$ crossing the radiator and the ROC. With its higher Lorentz factor only the electron generates transition radiation. Due to the large absorption cross section of xenon the TR photons are absorbed close to the boundary between radiator and drift region. Both charged particles generate primary electron clusters along the whole track [ALI08].

The bottom panel shows the corresponding signals' evolution over time. The first characteristic peak at 0.5 μs in all three signal curves is generated by charges from the amplification region with the ionization happening closest to the anode wires. The curve with the blue triangles is a pulse height plot for pions with a Lorentz factor of $\gamma = 10$ expected in ALICE. As no transition radiation is produced by the pions, only the ionization clusters from the drift region contribute to the signal after the first peak resulting in a plateau. This also holds true for the green curve for electrons without transition radiation. In the red curve the absorbed transition radiation photons from the start of the drift region generate a

second peak giving the electron signal a distinctly different shape [ALI08].
The top right panel shows the detected signal over 8 adjacent pads over 14 timebins for an electron with transition radiation. It can be seen that the time bins correspond to the x-positions of the particle track while the pad numbers correspond to the y-positions in the local tracking coordinate system described in section 8.1 [Gat10].

3.2.3 Gas Gain in Multi-Wire Proportional Chambers

A charged particle crossing the chambers deposits energy in the detector by ionizing gas atoms along its way. The energy loss per unit length of heavy charged particles due to ionization is expressed by the Bethe-Bloch equation [PRSZ09]:

$$\frac{dE}{dx} = -\frac{4\pi n Z^2}{m_e c^2 \beta^2}\left(\frac{e^2}{4\pi\varepsilon_0}\right)\left[\ln\left(\frac{2m_e c^2 \beta^2}{I\cdot(1-\beta^2)}\right) - \beta^2\right]. \tag{3.3}$$

Here n depicts the electron density of the medium, I is its mean ionization potential, $\beta = \frac{v}{c}$ is the fraction of lightspeed the particle is traveling at, m_e is the electron mass, and eZ stands for the charge of the particle. The particle's energy loss is mostly determined by its velocity, but not by its mass.
Figure 3.4 shows the energy loss per unit length for different particles in the ALICE TPC.

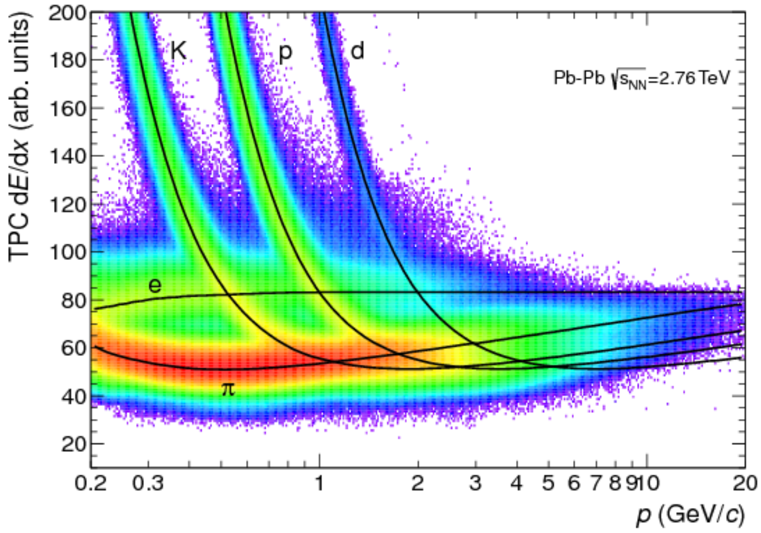

Figure 3.4: Specific energy loss dE/dx in the TPC vs. particle momentum in Pb-Pb collisions at $\sqrt{s_{nn}} = 2.76$ TeV. The lines show the expected mean energy loss from the Bethe-Bloch (hadrons) and Berger-Seltzer (electrons). [CERN13].

The black lines give the expected energy loss from the Bethe-Bloch formula for pions, kaons, protons, deuterons and electrons[2]. For momenta above 1 GeV the hadrons (pion, kaon, proton, deuteron) lose nearly the same amount of energy making them difficult to

---

[2] The Bethe-Bloch formula does not apply to electrons. Due to their low mass bremsstrahlung has a stronger effect on their energy loss which, accordingly, differs from that of the hadrons in the TPC. In analogy to Bethe-Bloch this can be described by the Berger-Seltzer formula [BS64].

distinguish from one another. The energy loss saturates at higher energies.

By applying the Bethe-Bloch formula one can estimate that an ionizing particle creates about 850 electron/ion pairs in the drift region. Given a readout pad capacity of 20 pF the deposited charge creates a signal amplitude of 2.56 μV [Bai09] which is too small for an analysis. Hence, the primary ionization electrons are multiplied in the amplification region. This is done proportionally to the primary signal.

For a cylindrical coaxial proportional counter the strength of the electrical field $E(r)$ is given by:

$$E(r) = \frac{\lambda}{2\pi\varepsilon_0 r} \tag{3.4}$$

In this equation λ is the linear charge density and ε_0 the vacuum dielectric constant. For a strong electric field thin anode wires have to be used which is realized in the ALICE TRD with a $r = 20$ μm wire. The primary electrons are accelerated in the electric field and ionize gas atoms. The deposited charge is therefore amplified by creating an electron avalanche which is proportional to the original charge deposit. The gas gain g in the ROCs is the ratio of the number of secondary electrons to the number of primary electrons from the ionization clusters:

$$g = \frac{N_{primary}}{N_{secondary}} \tag{3.5}$$

Most gas detectors are operated with noble gases in order to achieve high gas gains with comparatively weak electric fields. Noble gases have less degrees of freedom compared to complex molecules which would facilitate the absorption of energy without ionization. In addition to being ionized the noble gas is excited and emits photons when returning into the ground state. The photons can lead to ionization of the metal electrodes causing an undesired second electron avalanche. This effect is suppressed by adding a quenching gas consisting of more complex molecules. This quenching gas (CO_2 in the TRD) can absorb the photons without ionization due to the additional degrees of freedom.

The amplification factor of the chambers in proportional mode can be determined from the first Townshend coefficient α. This coefficient is a function of the electric field strength E and the particle density ρ. It depends on the electric field and gas type, and has a value of 0 for electric fields before a specific threshold voltage is reached at which electron avalanches can occur. The increase of the number of electrons dn for a traveled path dx is given by [Kno89]:

$$\frac{dn}{dx} = \alpha n \tag{3.6}$$

The solution of this differential equation leads to an exponential law predicting that the number of electrons will grow exponentially in the direction of avalanche progression.

The integration of equation 3.6 between the anode and the position of ionization gives the amplification factor g, as it was defined earlier:

$$g = \exp\left(\int_{x_0}^{x_a} \alpha(x)dx\right) = \frac{n(r_a)}{n(r_0)}. \tag{3.7}$$

The Townshend coefficient α's dependency on the electron energy is nearly linear for moderate gas gains. Thus, the gas gain shows an exponential dependence on the anode voltage, so variations of the anode voltage over time have to be avoided. For the TRD the anode voltage can be controlled with a precision better than 1 V [Bai09] [ALI01].

The total energy loss of particles in the chambers fluctuates as a variable number of interactions between the charged particles and the gas inside the detector takes place. The distribution of energy loss can be described with a Landau function [Gat10]:

$$f(\lambda) = \frac{1}{\sqrt{2\pi}} \cdot e^{-\frac{1}{2}(\lambda + e^{-\lambda})}. \tag{3.8}$$

In this distribution λ denotes the normalized deviation of the most probable energy loss $(\Delta E)_{\mathrm{mp}}$:

$$\lambda = \frac{\Delta E - (\Delta E)_{\mathrm{mp}}}{\langle E \rangle}. \tag{3.9}$$

Here ΔE is the actual energy loss of a particle and $\langle E \rangle$ is the average energy for a particle traveling a given path in the chamber. Simulations and measurements of the corresponding energy distributions for the ALICE TRD are depicted in figure 3.5. The long tail of the distribution is caused by high energy δ-electrons which can ionize further gas atoms. The mean value of the distribution is a measure for the average energy loss. Due to the distribution's shape it does not correspond to the peak which is the most probable value. As a result of the energy loss fluctuations, calculations of the gas gain have to be performed with large numbers of events for sufficient statistics [Gat10] [Alb10].

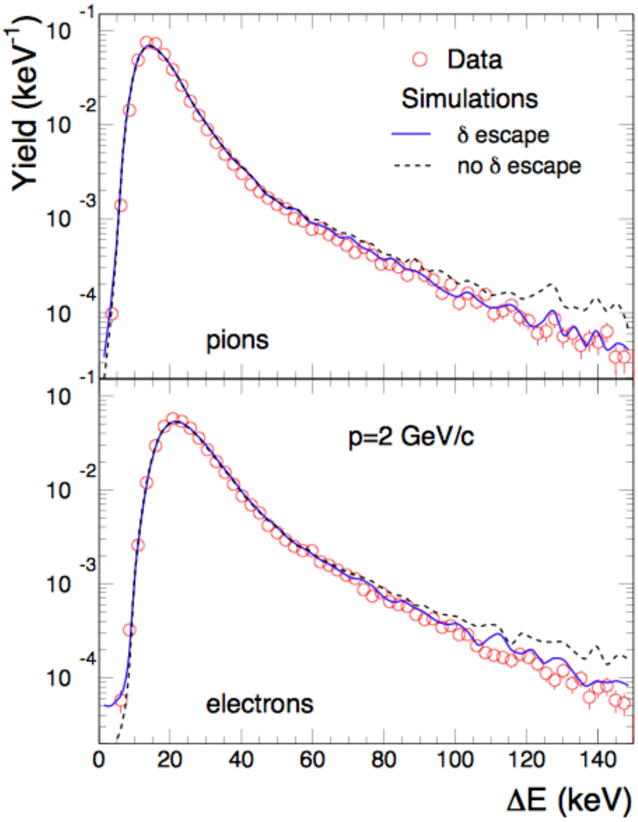

Figure 3.5: Measurement and simulations of the energy deposit of pions (top) and electrons (bottom) in the ALICE TRD. δ escape denotes the realistic treatment of δ-rays. [AW11].

3.2.4 Electronics

Figure 3.6 presents a schematic overview of the ALICE TRD readout electronics [AW11] [Gat10]. The Front-End Electronics (FEE) can be subdivided into two parts: the Front-End Readout Electronics (FERO), which are mounted directly on top of the ROCs, and the Global Tracking Unit (GTU).

The FERO includes Multi Chip Modules (MCMs) performing the pad readout, the Optical Readout Interface (ORI) boards which transfer the data from the MCMs to the GTU via optical fibres, and Detector Control System (DCS) boards which control and configure the MCMs and ORI boards.

In order to provide fast trigger decisions for high p_{T} electrons within 6.5 μs data has to be processed right after a collision. Consequently, a first analysis is performed locally in the MCMs. The signal path in an MCM can be seen in figure 3.6.

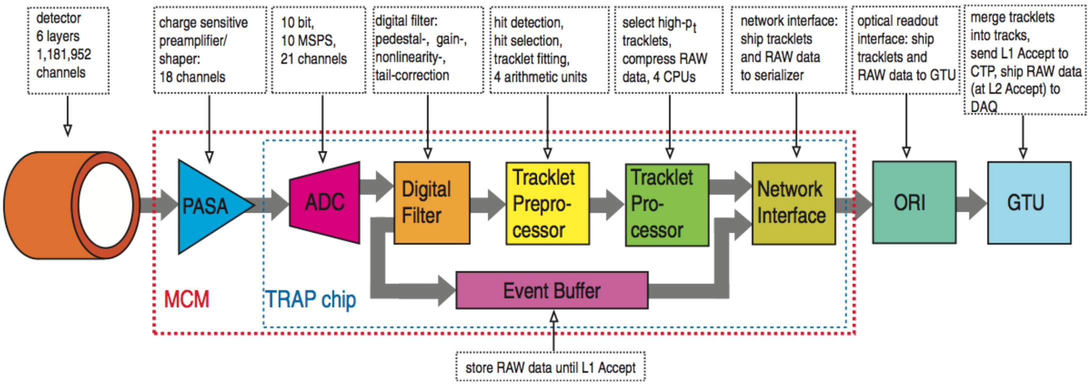

Figure 3.6: Overview of the readout electronics of the ALICE TRD [ALI08].

A charge sensitive Preamplifier and Shaper (PASA) and Tracklet Preprocessor (TRAP) are integrated into one MCM. The PASA has 18 input channels and 21 output channels. 18 pads are read out by one MCM, so the 144 pads in each column are managed by 8 MCMs. The extra output channels are used for charge sharing between TRAPs across MCM boundaries [AW11]. The TRAP itself consists of the Tracklet Preprocessor (TPP), an Analog to Digital Converter (ADC), an event buffer and four Multiple Instruction Multiple Data Central Processing Units (MIMD CPUs).
For each channel the incoming signal is shaped and amplified by the PASA and digitalized by the ADC. The conversion rate of the ADC is 10 MHz with a resolution of 10 bits. Then the raw data is stored in the event buffer for a potential readout after a positive L1 trigger decision[3]. The amplified signal is filtered and the TPP searches possible hits, parametrizes the clusters and fills hit registers. The MIMD CPUs subsequently use this data to determine tracklets by fitting straight lines through clusters presumably belonging to the same particle track. This is only for clusters within the same ROC. Thereafter, the tracklet information is shipped to the GTU which matches the tracklets from the individual ROCs within one stack and derives an L1 trigger decision.

3.3 Calibration Parameters and Motivation for Gain Calibration

Three crucial calibration parameters can be determined directly in Münster: the supermodule alignment, drift velocity and gas gain:

- The final geometry of the ALICE TRD does not match its design geometry due to deformations, and a limited accuracy in production and assembly. The relative alignment of the chambers in one supermodule or of the supermodules in the TRD with respect to each other can be corrected by determining the deviations from ideal

---

[3] As the ALICE detectors have different readout times, an identification and selection of interesting events is mandatory. This is achieved via a multi stage trigger system. A detailed discription of this system can be found in [Ani11]: Each trigger sequence consists of a pretrigger (PT), the L0, L1, L2 and the High Level Trigger (HLT). The PT is a fast trigger for activating the TRD electronics. The L0, L1 and L2 are generated by a Central Trigger Processor (CTP) using 50 trigger contributions from the ALICE subdetectors. The HLT is a software trigger running an online analysis and reconstruction. After the HLT the events are passed to the Data Acquisition-System (DAQ) and stored permanently.

geometry. This calibration will not be performed in this thesis, but is carried out in [Sic09] and [Gat10].

- The drift velocity determines the position resolution in the TRD as it influences the reconstructed x-position of a particle track [Gat10]. Accordingly, the measurement of the drift velocity is crucial in order to achieve the desired position resolution.
- The knowledge of the precise gas gain in the ROCs is important for particle identification for it is directly linked to the energy deposition in the chambers [Wil10]. The gas mixture in the chambers, temperature, pressure, wire sagging, and anode and drift voltages affect the number of secondary electrons created by primary ionization electrons [Gat10]. Mechanical deformations of the chambers also have a noticable effect. The angle of the track with respect to the axis perpendicular to the wire plane also has to be taken into account, as the amount of deposited energy increases with a longer distance traveled inside the detector, i.e. for large angles [Alb10].

4 Cosmic Rays and the Experimental Setup in Münster

Tests of the TRD supermodules in Münster utilize cosmic radiation as a high energy particle source. Particles and atomic nuclei which originate in stars - the primary cosmic radiation - interact with atoms of the earth's atmosphere causing particle showers. These particles can be detected at sea level as secondary cosmic radiation.

4.1 Primary Cosmic Radiation

Products of stellar nucleosynthesis accelerated by cosmic sources and traversing interstellar space are referred to as primary cosmic radiation. This radiation mainly consists of free protons (approx. 79 %) and helium nuclei (approx. 15 %) [PDG13a], with other common particles being electrons and virtually all atomic nuclei abundantly synthesized in stars. Neutrinos and photons are present as decay products.

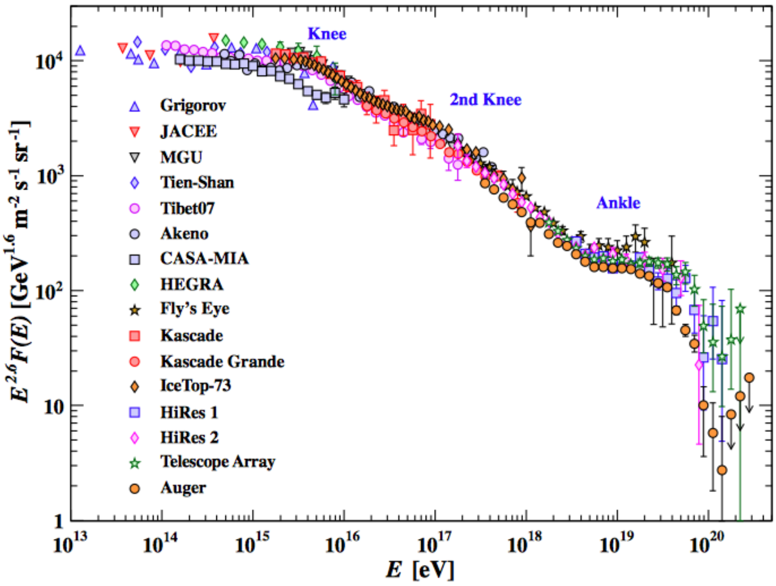

Figure 4.1: The all-particle spectrum of cosmic rays as a function of the energy per nucleus from air shower measurements [PDG13a].

The energy spectrum of cosmic rays extends from several 10^9 eV to around 10^{20} eV [PDG13a]. The particle flux decreases with higher particle energies. At 10^{15} eV (*knee*), 10^{17} eV (*2nd knee*) and 10^{19} eV (*ankle*) the flux spectrum shows kinks. These abrupt variations in particle flux are attributed to the dependence of the particle energies on the processes they originate from and are not yet fully understood. Those generating particles with extremely high energies around the *ankle* are a field of particular interest in current research. As primary cosmic radiation interacts with interstellar gas and magnetic fields, its particles are deflected causing a loss of directional information[1]. Therefore cosmic radiation is isotropic up to energies of 10^{14} eV. The influence of perturbations is less significant for particles with higher energies [Gru05]. The flux is also influenced by solar wind which can prevent low energy primary cosmic particles ($E < 10^9$ eV) from reaching earth depending on solar activity.

4.2 Secondary Cosmic Radiation

Cosmic radiation at sea level is almost entirely produced in interactions of primary cosmic rays in the air. Primary protons interact with atmospheric nuclei at altitudes of typically 15 km producing mostly pions and kaons with a pion to kaon-ratio of 10:1 due to the lower mass of the pion. Muons and neutrinos emerge from decays of charged mesons, while the decays of neutral mesons and subsequent electromagnetic showers generate photons, electrons and positrons [PDG13a]. Muons comprise the most common charged secondary particles at sea level as shown in figure 4.2 and are, therefore, most relevant for experiments with cosmic rays in Münster. Before reaching the ground they lose about 2 GeV due to ionization and radiative processes which reduces their relativistically expanded decay length.

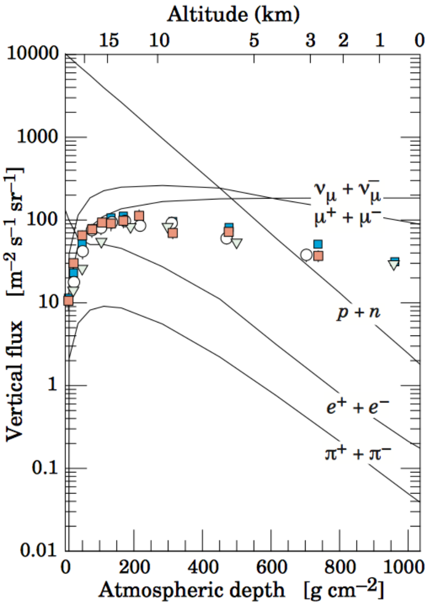

Figure 4.2: Estimated vertical fluxes of cosmic rays in the atmosphere with $E > 1$ GeV. The points show measurements of negative muons with $E_{mu} > 1$ GeV [PDG13a].

The mean energy of muons at the ground is ≈ 4 GeV. The overall angular distribution for muons at sea level is $\propto \cos^2 \theta$, with θ being the zenith angle, for energies around the mean energy. At large angles low energy muons decay before reaching the surface due to a longer

---

[1] With respect to this the term "primary" can be misleading. Technically almost none of the particles hitting the earths atmosphere are primaries because they are products of the interaction of primaries with interstellar matter. The question whether there is a small fraction of truly primary particles among those colliding with the earths atmosphere is of current interest [PDG13a].

path in the atmosphere which results in an increasingly steep angular distribution for low energies. Thus the distribution flattens for higher energy muons. The integral intensity of vertical muons above 1 GeV at sea level is $I_\mu \approx 1\ \text{cm}^{-2}\text{s}^{-1}$ [PDG13a]. The bottom layer of the cosmic trigger in Münster covers an area of $\approx 3{,}8\ \text{m}^2$ which corresponds to ≈ 633 muons hitting the bottom trigger per second. For the top layer of a TRD supermodule with an area of $\approx 7{,}9\ \text{m}^2$ one would expect about 1300 hits per second [Alb10].
With a Lorentz factor of $\gamma \approx 38$ at 4 GeV muons do not generate transition radiation. Furthermore, in Münster the detector is oriented upside-down with respect to the actual particle incidence in ALICE causing cosmic rays to traverse the drift volume before the radiator [Ani11]. Nevertheless, muons can be used for detector calibration and alignment:

- The charge deposit of crossing $\mu^\pm$ in the chambers of the supermodule can be used for gain calibration.
- Muon tracks are straight due to the muons' high energy and the absence of strong magnetic fields. This can be used to correct misalignments of the chambers in Münster or the alignments of whole supermodules with respect to each other in the final ALICE TRD.
- The entire supermodule's readout chain can be tested with real particle tracks [Ani11].

4.3 Experimental Setup in Münster

The gain calibration is carried out for standalone supermodules (SM) in Münster utilizing mostly cosmic muons ($\mu^\pm$), which emulate signals of pions ($\pi^\pm$) in ALICE [Alb10] due to their similar mass.
The trigger system of the ALICE detector is substituted by a custom trigger system, the Cosmic-Trigger (CT) which provides a trigger signal to the SM in case of the passage of a charged cosmic ray particle. The CT is comprised of 90 scintillation counters each consisting of a scintillator and a photomultiplier. These are installed above and underneath the SM as depicted in figure 4.3. While the bottom layer of scintillators stretches along the whole length of the supermodule the top part can be moved alongside the SM's z-axis. The top layer of scintillators is comprised of 4 groups with 10 scintillators per group, the bottom layer consists of five groups, also with 10 scintillators each. The signal thresholds and supply voltages for the counters can be adjusted individually for each group in order to achieve a uniform distribution of trigger signals with adequate noise suppression.

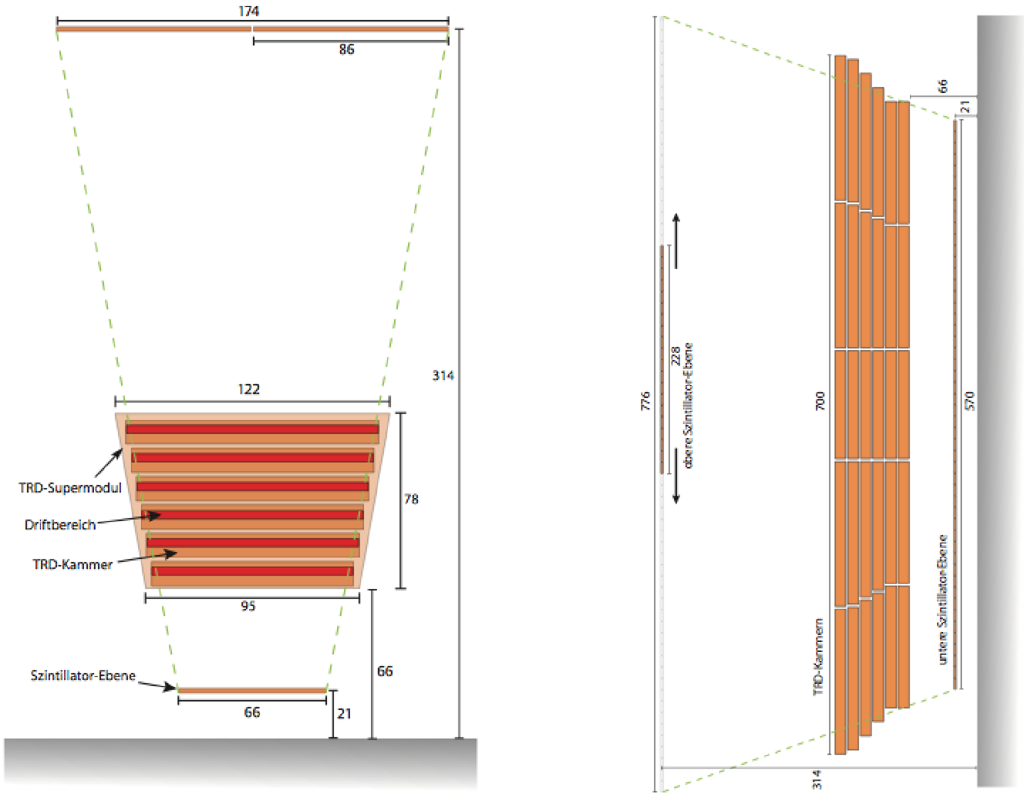

Figure 4.3: Front and side view of the trigger system used in Münster with a supermodule installed between top and bottom layer. All dimensions given in centimeters. Taken from [Bat07].

The CT can be run in two different modes: coincidence mode or bottom trigger only. In coincidence mode a positive trigger signal is given if both planes of the CT detect a particle in a short timeframe. After a positive trigger a full read out of the SM is carried out. Due to the CT's design a particle creating a coincidence signal has crossed all six layers of the SM. In coincidence mode this limits the acceptance of particles in φ- and z-direction. The maximum acceptance angle is $\varphi \approx 26°$ which makes it unlikely to detect particle tracks at the chamber edges [Alb10]. For calibration at high granularities the resulting lack of statistics at the chamber edges is a problem.

In the second trigger mode a so-called pretrigger is sent to the SM when the bottom scintillation counters detect a hit of a cosmic particle. Subsequently, the SM ships the tracklets to the Global Tracking Unit (GTU), which decides to store the event if at least four tracklets are found in one stack. This increases the angular acceptance to $\varphi \approx 58°$ [Alb10]. Almost all runs in this thesis were recorded with a combination of both trigger modes.

Considering that the angular distribution of the tracks is a superposition of the trigger's acceptance angles and the cosmic rays' angular distribution, the recorded tracks are not evenly distributed within the chambers. The incidence angles of the tracks become exceedingly limited the closer they are registered at the chamber edges. Particles crossing intermediate frames between the stacks rarely create a signal because the GTU only stores tracks with at least four tracklets per stack. Accordingly, tracks should be found mostly in the center of the chambers.

The supermodules in Münster are tested with a gas mixture different from the one in the final ALICE assembly. While the ALICE TRD is operated with a Xe/CO_2-Mixture the assembly and testing in Münster are carried out with an Ar/CO_2-mixture (82/18 %) for economic reasons. The use of Ar instead of Xe leads to different characteristics of the chambers regarding drift velocity and gas gain while simultaneously changing both properties' susceptibility to contaminations of the chambers with O_2 and N_2 [And04]. Per default the drift and anode voltage in the chambers are set to 1.5 kV, although different voltages have been investigated in this thesis.
Three pairs of consecutive layers are connected to one gas input via three "mix lines". The composition of the filling gas which is consequently the same in all mix lines can be chosen. While the gas mixture is the same for all chambers the gas flow and resulting pressure in the chambers can be adjusted for each mix line and are monitored by an optical sensor for one mix line at a time [Alb10].

4.4 Trigger Configuration

Each scintillation counter group of the CT is attached to a TREFI-08 module which serves as a preamplifier and discriminator. An output signal from the TREFI-08 module is generated when a chosen threshold voltage is exceeded by the input signal from at least one counter in a group [Bat07]. A CAEN V1495 board is the central trigger unit. It processes the scintillator signals from the TREFI-08 modules and the GTU and generates trigger sequences (pre-trigger, L0, L1) that are directed to the SM and the GTU via optical fibers. A detailed explanation of the trigger system can be found in [Bat07] and [Ani11].

The trigger is configured in order to maximize its sensitivity for cosmic particles while providing adequate noise suppression. The threshold voltages for the top and bottom scintillator groups have to be chosen accordingly. This is achieved by investigating the trigger rates' dependance on the threshold voltage of the discriminators. Although this procedure has been performed before, there is no recent exertion of the cosmic trigger setup for calibration purposes. Therefore, changes of the scintillation counters' properties needed to be identified and corrected comprehensively.

The trigger rate's dependence on the threshold voltage is a superposition of noise and actual cosmic ray signals. Ideally, at a certain threshold noise is fully suppressed without vetoing real physical signals which are significantly stronger. This results in a plateau with a nearly constant trigger rate over a certain threshold range. If the threshold voltage is raised beyond this range, cosmic signals are progressively rejected causing a visible drop in the trigger rate [Bat07]. For lower voltages an exponential increase in the trigger rate due to noise is expected.
The individual scintillation counters differ in quality and signal strength. The fact that only one uniform threshold voltage can be chosen for a whole group connected to one discriminator exacerbates the task of setting the threshold voltage in the plateau region.

In order to facilitate this task, counters of similar quality were initially grouped together. The threshold for one group is determined by using the scintillator providing the weakest signal in a group at a given default voltage. The weakest scintillation counter corresponds to the lowest counting rate in the group.

The counting rate is measured by resetting the scintillator counters and having the signals of the individual groups with only a single scintillator attached to the TREFI counted for one minute. The counting rate is then obtained by dividing the total signal count by 60 seconds. The relative uncertainty for the total count N is

$$\sigma_{N_{rel}} = \frac{\sigma_N}{N} = \frac{\sqrt{N}}{N} \tag{4.1}$$

and decreases with time as N increases with time. One minute is a sufficient measurement interval if the resulting uncertainty of the counting rate

$$\sigma_f = \frac{\sqrt{N}}{60}\ \text{Hz} \tag{4.2}$$

is of a similar order of magnitude as the differences in the counting rate for different thresholds. The voltages set in the prior configuration are used as default values for finding the weakest counter per group. Its counting rate f is plotted at different threshold voltages U_{th} in order to identify the plateau region. This method prevents a cutoff of any physical signals for any of the other scintillators in the group. Recorded data for the weakest scintillators of the cosmic trigger is depicted in figure 4.4 for the bottom layer and in figure 4.5 for the top layer. The new threshold voltages are marked by vertical lines and given in table 4.1.

Group	U_{th} [mV]	Counts/min
B1	137	11304 ± 107
B2	105	10419 ± 103
B3	100	10234 ± 102
B4	110	8401 ± 92
B5	70	3344 ± 58
T1	143	19715 ± 141
T2	145	24055 ± 156
T3	146	23883 ± 155
T4	145	26316 ± 163

Table 4.1: New threshold voltages and trigger rates of the five groups of scintillation counters in the bottom layer and the four groups in the top layer.

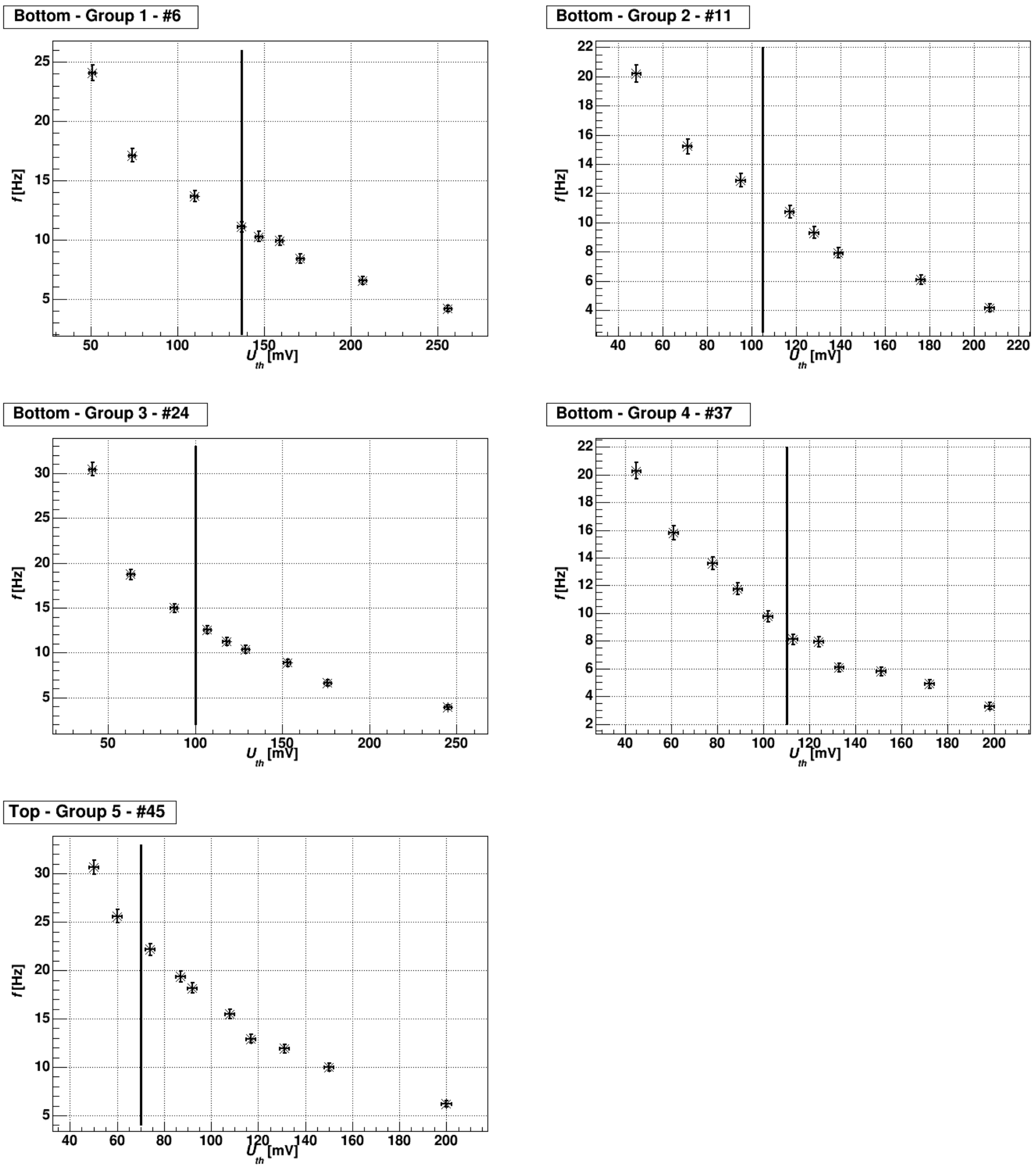

Figure 4.4: Counting rate in dependence of threshold voltage for the weakest scintillators in the bottom groups. The vertical error bars are given by σ_f, the horizontal error bars are given by the reading accuracy of the used multimeter. The new threshold voltages are marked by vertical lines.

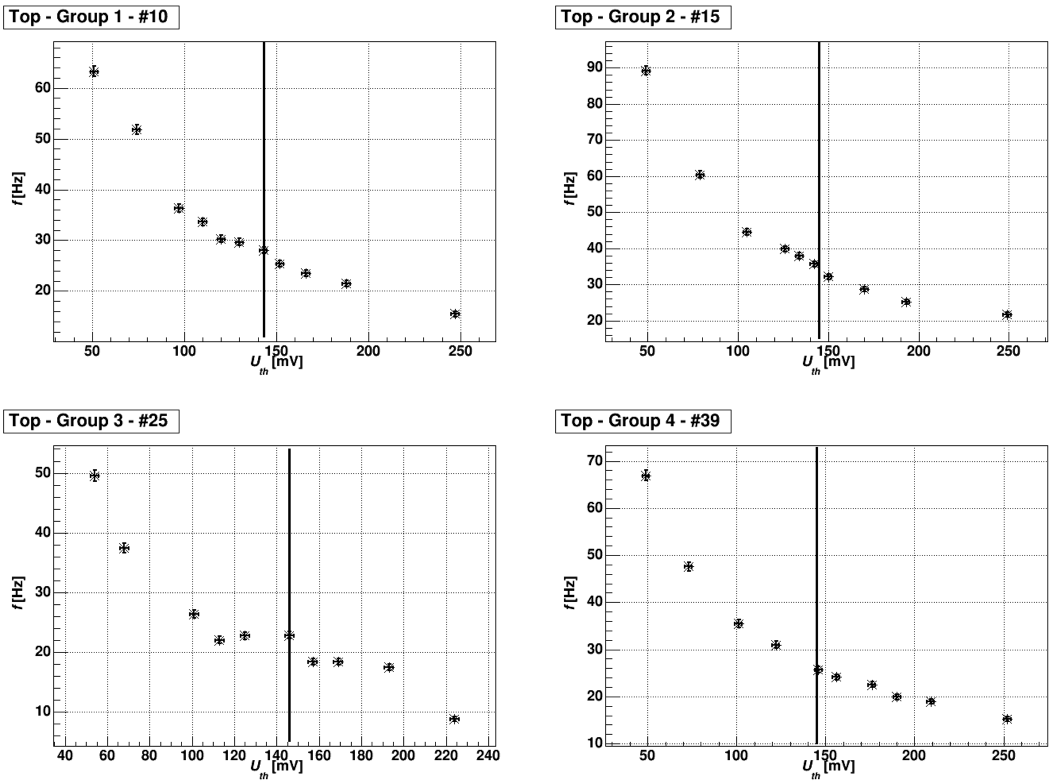

Figure 4.5: Counting rate in dependence of threshold voltage for the weakest scintillators in the top groups. The vertical error bars are given by σ_f, the horizontal error bars are given by the reading accuracy of the used multimeter. The new threshold voltages are marked by vertical lines.

Top group 3 scintillator #25 shows a prominent plateu region. Yet, for most scintillators it is difficult to make out. This has two main reasons:

- In theory the threshold can be chosen freely which would allow for small variations. In practice the setting of the thresholds at the TREFI modules, carried out with a screwdriver, allows for variations of only a few mV in one voltage region while denying steps below 15 mV in others. This behavior is different for each discriminator and limits the choice of threshold voltages, which is especially unfavourable in narrow plateau regions. Such a plateau region could have been found in the bottom groups 1 and 2 and the top group 4.

- The #45 scintillator of bottom group 5 showed a very weak signal throughout the voltage range making it necessary to set low threshold in order to obtain usable counting rates. In this voltage region real physical signals can hardly be distinguished from noise. This can be shown by applying an exponential fit to the data points as such a signal curve would be expected for a pure noise signal.

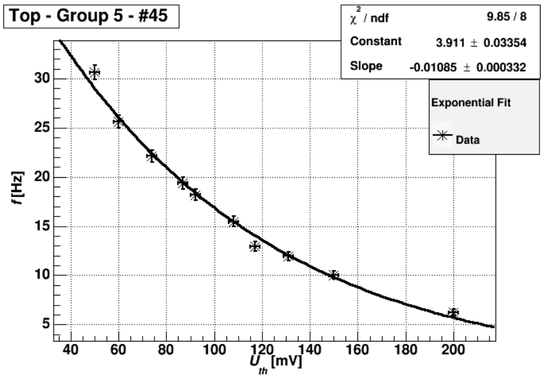

Figure 4.6: Exponential fit of the counting rate against threshold voltage diagram of bottom group 5 scintillator #45.

The new threshold voltage is roughly set at the low voltage end of the plateau region in order to increase the counting rate. In earlier configurations it was set at the high voltage for noise suppression. Due to the aging of the scintillators the counting rates are significantly lower than in earlier operation. For example bottom group 2 achieved trigger rates of up to 250 Hz [Ani11] while, with the current settings, the counting rate dropped to about 174 Hz. Subsequently, it is necessary to lower the thresholds in order to keep run durations in reasonable timescales.
This approximate setting is possible because the coincidence condition and the 4-tracklet criterium of the GTU contribute to noise suppression. With a signal width of 20 ns and typical trigger rates of 1300 Hz for the top and 300 Hz for the bottom plane of the trigger the number of random coincidences can be estimated with [Bat07]:

$$N_{random} \approx 20 \cdot 10^{-9}\ \mathrm{s} \cdot 1300\ \mathrm{s}^{-1} \cdot 300\ \mathrm{s}^{-1} = 7{,}8 \cdot 10^{-3}\ \mathrm{s}^{-1} \tag{4.3}$$

Therefore, priority can be given to the equalization of counting rates over all sections of the cosmic trigger. This could be achieved in most cases with the exception of the weaker bottom 4 and 5 scintillator groups, as can be seen in table 4.1.

4.5 Data Acquisition

The aim of the calibration procedure is a calibration of the relative gain factor for each single cathode pad in the supermodule. This requires the accumulation of enough statistics per run. The required run-time can be estimated by making the following assumptions: each event should contain at least 4 tracklets in one stack and for a given event it is assumed that just one pad is read out per tracklet. Thus, adjacent pads with smaller amplitudes are neglected. For a reliable calibration between 100 and 1000 tracklets should be found for every pad. This is further discussed in section 6.2.

Assuming a total of 144 pad rows, 64 pad columns[2], 6 layers and 4 tracklets per event, roughly $13.82 \cdot 10^6$ events are needed. The maximum trigger rate achieved in bottom

---

[2] Supermodule XVI does not contain a stack 2 which would add a further 12 columns.

trigger mode is about 140 Hz. With this recording rate runs need to last approximately 28 hours. Taking into account that the tracks are unevenly distributed in the chambers, runs have to last at least 3 or 4 times longer for sufficient statistics at the chamber edges. Figure 4.7 shows data from run 3075 with 8,426,617 recorded events after about 24 hours.

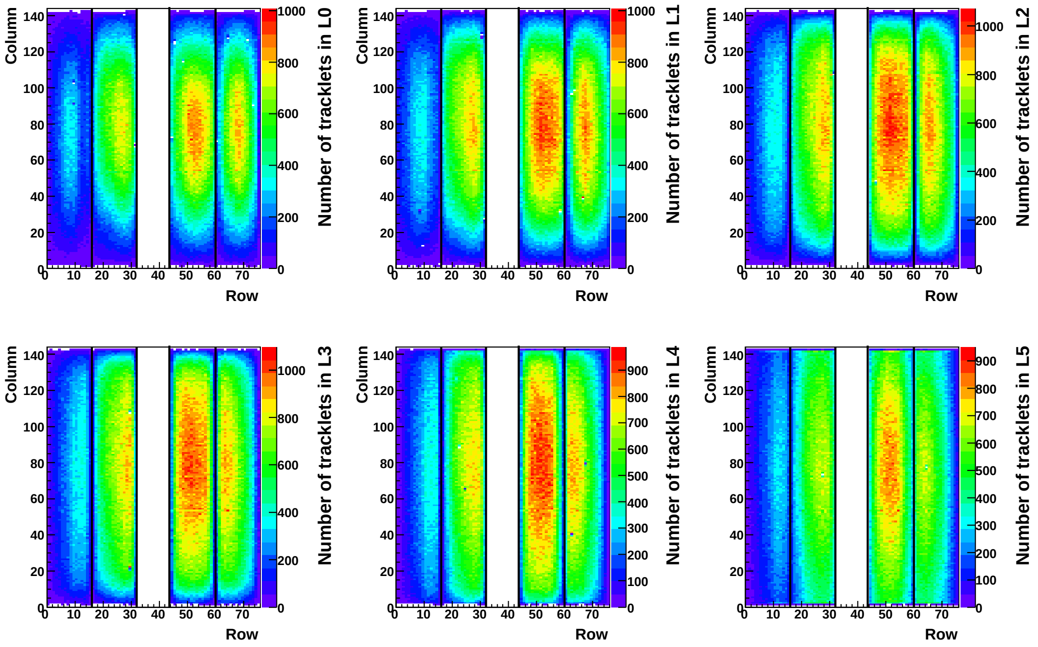

Figure 4.7: Tracklets per group for run 3075 with 8,426,617 events. Each calibration group (cell in the plot) corresponds to one cathode pad.

Most tracks are found around the center of the chambers, with up to 1000 entries per calibration group. Groups at the chamber edges contain 200 tracks or even less. Additionally, fewer tracks are found in the chambers above the weaker scintillator groups: group B5 is located below stack 0 which shows low track counts in all layers.

The maximum trigger rate while recording deviates from the values that were found during the configuration of the trigger. The readout rate was limited by data suppression and storage. The amount of data in SM-XVI was significantly higher than usual due to a higher noise level and, accordingly, less sufficient zero suppression[3].The data volume lead to computer overloads, so in early runs the trigger rate frequently dropped to zero, effectively cutting the average recording rate in half and doubling the needed runtime. This problem was amended by running the recording stream on two CPU cores instead of one.

Ultimately, most runs were recorded with a combination of coincidence and bottom trigger

---

[3] The amount of data is usually limited by activating a noise suppression (zero suppression) in the FEE configuration. The FEE configuration states which trigger system, trigger mode, filters and number of timebins are used for data acquisition.

mode with zero suppression engaged (FEE tag: 311). Run durations ranged between 1 and 47 hours at recording rates of about 140 Hz. Although longer runs would have been favoured, the assembly and testing schedule of the SM combined with the fixed shipping date to CERN did not allow for longer runs. Therefore, data of different runs with the same settings have to be combined and shorter runs with different parameters are investigated at smaller granularities[4].

---

[4] Table 8.1 in the appendix contains a list of all recorded runs and the settings used.

5 Run Reconstruction and Supermodule Calibration with AliRoot

The particle identification (PID) algorithms in the TRD are based on the energy loss of particles traversing the readout chambers. This energy loss is derived from the shape of the signals provided by the cathode pads of the chambers, as discussed in chapter 3.3. With the shape of the signals being largely dependent on the signal amplification, a gain calibration for each individual pad is necessary, in order to provide a fast trigger on electrons in the entire supermodule. The gain calibration procedure is subdivided into four steps: pass0-reconstruction, determination of the drift velocity, pass1-reconstruction and determination of the gain factors in the chosen calibration groups.

The particular steps of the calibration are implemented in the AliRoot framework. AliRoot is based on the ROOT data analysis software which uses C++ as a command language [Roo07]. The AliRoot package expands the ROOT data analysis framework with ALICE-specific classes for event simulation, reconstruction and calibration purposes [AliOff]. The macros that were used in this thesis were subject to a PhD thesis [Bai09] and used in two diploma theses [Alb10] [Gat10]. The code has been used for the reconstruction of raw data, gain calibration and the determination of average drift velocities, signal time offsets and the width of pad response functions. Since last use of the code for calibration tasks in Muenster in 2010 it has been extensively modified by various users. These modifications and the deployment of newer AliRoot versions required several revisions of the provided code in order to assure functionality and compatibility with the current AliRoot. The fixed macros were cleaned up and collected in order to provide an accessible framework for future calibration efforts. In this chapter the different steps of the calibration procedure are presented. Additionally, a brief overview of the applied algorithms is given.

5.1 The Offline Conditions Database

All calibration and alignment parameters of a TRD supermodule are stored in the Offline Conditions Database (OCDB). The OCDB is not literally a database like, for instance, MySQL, but a set of entries in the AliEn[1] file catalog which point to the ROOT files containing the calibration parameters [AliOff]. The OCDB is used for the reconstruction of the raw-files created from the GTU data. OCDB files are also created in the course of the calibration procedure in order to store the determined values for the drift velocity and gain factors.

The nomenclature for OCDB files is `Run<range>_<version>_<subversion>` with the range

---

[1] **Ali**ce **En**vironment is a lightweight Open Source Grid Framework built around other Open Source components using the combination of a Web Service and Distributed Agent Model [AliEn].

being the run range for which the OCDB object is valid and the version and subversion numbers [Gat10]. By default AliRoot uses the newest OCDB files denoted by higher version and subversion numbers [AliOff]. The ROOT-files for the different calibration parameters are stored in subfolders with the respective names, such as `TRD/Calib/ChamberGainFactor` [Gat10].

5.2 TRD Data Reconstruction

In the pass0-reconstruction [Gat10] the raw data is reconstructed using expected values of the calibration parameters stored in a default OCDB. For initial calibration in Münster, the OCDB is comprised of the standard AliRoot OCDB and supplemented by custom files. This is done for two reasons: First, custom OCDB entries allow the choice of different drift verlocity values for the reconstruction. Second, the default OCDB of the current AliRoot version is designed for the reconstruction of raw data with 24 timebins while the raw data from the MCMs in Münster contains 30 timebins. This requires adaptions of specific default OCDB files. The default values used for the pass0 are a drift velocity $v_{\text{drift}} = 1.5$ cm/µs and a uniform relative gain $g = 1$ for all readout pads.

The reconstruction is performed on the raw-files which are converted into different objects in the course of the analysis. Signals from adjacent pads within a timebin are most likely generated by the same particle and are collected in clusters. The identification of the clusters is followed by the determination of the space points where the particle has crossed the detector. The space points contain three coordinates with errors and the index of the subdetector where the particle was found. The possible particle trajectories, the tracks, are reconstructed by fitting lines to the space points. These lines are defined by five parameters which are the coordinates of one track point and the angles θ and ϕ in the global ALICE coordinate system[2].

The reconstruction output is then stored in `AliESDs.root` containing the main information which is used by common physics analyses and `AliESDfriends.root`, which provides additional information for debugging and detector calibration [Gat10]. Detailed information on the reconstruction and track-fitting algorithms can be found in [Bai09] and [AliOff].

5.2.1 Reconstruction Parameters

For offline reconstruction it is possible to set reconstruction parameters [AliOff] for different run and event types[3] in the reconstruction macro `rec_new.C`. Among other things, these parameters define filters [Fas08] [Ras10] for track-fitting which are used by the track-finding class `AliTRDtrackerV1`. The reconstruction in this thesis has been performed using cosmic test parameters:

- The χ_y^2 and χ_z^2 filters are applied during the identification of track seeds. Different seeding configurations for the clusters belonging to the same track are investigated. Within a window defined by two angles helix fits are applied to the various combina-

---

[2] An overview of the ALICE coordinate systems can be found in section 8.1 in the appendix.

[3] The run and event types and the corresponding parameters are described in detail in [AliOff].

tions of seeding clusters. Those fits with χ^2 exceeding the reconstruction parameter value for y and z are dropped.

- The track likelihood is a cumulative value based on the total number of clusters associated to a tracklet and the χ^2_y and χ^2_z values. It serves as the main quality criterion for track selection.

By default all three filters are activated for reconstruction. This led to an empty reconstruction output in early attempts, as the likelihood filter caused a universal track rejection. In earlier theses this has not been an issue and can be attributed to the newer AliRoot version v5-04-18 used in this thesis. Furthermore, the χ^2 cuts eliminated about 50 % of the track candidates. In turn only half of the recorded events in a run can be used for calibration. This is also mentioned in [Alb10]. A function for toggling the filters on and off in `rec_new.C` has been implemented into AliRoot by B. Bathen in order to enable reconstruction and investigate the influence of the χ^2 filters on the reconstruction results.

5.3 Drift Velocity Calibration

The drift velocity value used for reconstruction directly influences the x-position of a particle which is determined as a function of time by

$$|x(t)| = \int_{t_0}^{t} v_{\text{drift}}(t)dt = v_{\text{drift}} \cdot (t - t_0) \tag{5.1}$$

where t_0 denotes the time of the particle reaching the pad plane and v_{drift} is the drift velocity. Under the assumption that the electric field of the drift region is homogenous the drift velocity is constant. The choice of incorrect values of the drift velocity leads to errors in the reconstruction of the x-position. Thus, a precise knowledge of the drift velocity is crucial for further analysis [Bai09] [Gat10].

5.3.1 Granularity settings

The drift velocity and relative gain factors can be determined for different levels of precision. At the finest granularity a pad-wise calibration can be carried out or adjacent pads can be summarized to form calibration groups. The numbers of columns and rows in one calibration group are defined by nz and $n\phi_r$. In order to determine the calibration parameters of the single readout chambers, the granularity settings are set to $(nz, n\phi_r)$ = (0,0). A calibration per readout pad is carried out with $(nz, n\phi_r)$ = (4,6). The different granularity options are given in table 5.1.

nz / $n\phi_r$	1	2	3	4
1	$2 \cdot 2$	$2 \cdot 4$	$2 \cdot (N_{\text{row}}/2)$	$2 \cdot N_{\text{row}}$
2	$4 \cdot 2$	$4 \cdot 4$	$4 \cdot (N_{\text{row}}/2)$	$4 \cdot N_{\text{row}}$
3	$8 \cdot 2$	$8 \cdot 4$	$8 \cdot (N_{\text{row}}/2)$	$8 \cdot N_{\text{row}}$
4	$16 \cdot 2$	$16 \cdot 4$	$16 \cdot (N_{\text{row}}/2)$	$16 \cdot N_{\text{row}}$
5	$36 \cdot 2$	$36 \cdot 4$	$36 \cdot (N_{\text{row}}/2)$	$36 \cdot N_{\text{row}}$
6	$144 \cdot 2$	$144 \cdot 4$	$144 \cdot (N_{\text{row}}/2)$	$144 \cdot N_{\text{row}}$

Table 5.1: Number of calibration groups per chamber according to the choice of nz and $n\phi_r$ with N_{row}=12 for the chambers of stack 2 and $N_{\text{row}} = 16$ for the other stacks [Bai09].

5.3.2 Determination of the Drift Velocity

The mean drift velocity in a calibration group is calculated by dividing the length of the drift region l_{drift} by the travel time t_{drift} of the electrons through this region:

$$v_{\text{drift}} = \frac{l_{\text{drift}}}{t_{\text{drift}}} = \frac{3 \text{ cm}}{t_{\text{D}} - t_{\text{A}}}. \tag{5.2}$$

The times t_{A} and t_{D} can be identified in the pulse height spectra. These times which correspond to the start and end of the drift region are extracted from the spectra in the following way (see figure 5.3):

- The first peak in the spectrum is caused by ionization electrons from both sides of the anode wires. Thus the amplification region starts with the start of the signal at t_0.
- With the maximum of the peak at t_{A} the amplification region ends. The falling flank of the amplification peak is a result of the detector's time response and does not belong to the signal created in the amplification region.
- The flat plateau is caused by electrons from the drift region and ends at t_{D}. A long ion tail can be seen at the end of the signal.

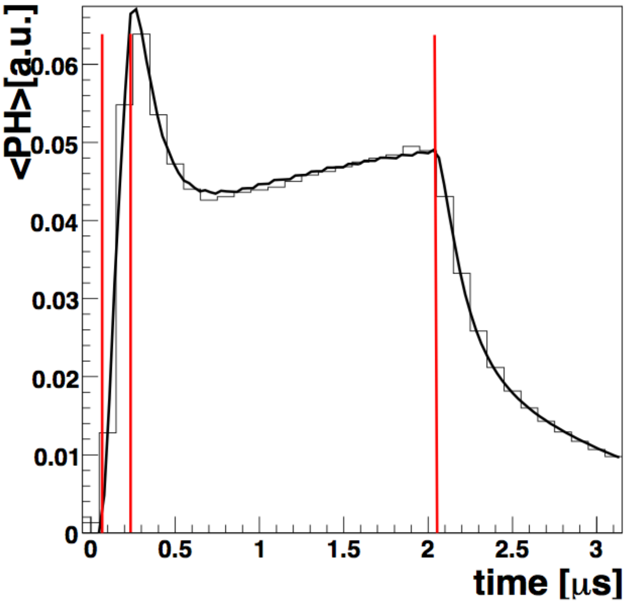

Figure 5.1: Simulation for $\langle PH \rangle$ for $\pi^{\pm}$ at 1 GeV. The vertical red lines signify the determined t_0, t_A and t_D [Bai09].

The macro `runTask.C` creates a calibration task on raw data for a chosen granularity (nz,$n\phi_r$) and executes the analysis task. This task is defined in `AliAnalysisTaskTRDCalib.cxx`. Using the class `AliTRDCalibraFillHisto.cxx` it fills the pulse height spectra for each calibration group of the detector. The spectra are then written into a file named `TRDCalibration.root`. Simulated pulse height spectra from a set of calibration groups are shown in figure 5.2. The y-axis shows the time in μs, the x-axis is for the calibration groups. A projection of the spectra to the x-axis gives a pulse height plot. The macro `determineCoeff.C` is then used to evaluate the spectra making use of the classes `AliTRDCalibraFit.cxx`, `AliTRDCalibraVector.cxx` and `AliTRDCalibraMode.cxx`.
The times t_0, t_A and t_D have to be determined with a precision better than one timebin. This is done by determining the respective timebins and interpolating the signal with a polynomial [Gat10]. Then t_A is determined as the maximum of the polynomial. The reversal points of the polynomial give t_0, the maximum of the first derivative, and t_D, its minimum. For each cathode pad v_drift is stored in an OCDB as discussed in section 5.1. If not enough statistics were accumulated or the determination of the values failed, a default value of 1.5 cm/μs is assumed for the pads of a group [Gat10][4]. The new drift velocity OCDB is then used for a second reconstruction, the pass1 which is essentially similar to the pass0, but offers better detector resolution owed to the precise knowledge of v_drift.

---

[4] This is the drift velocity in the final ALICE assembly with the Xe/CO_2 gas mixture.

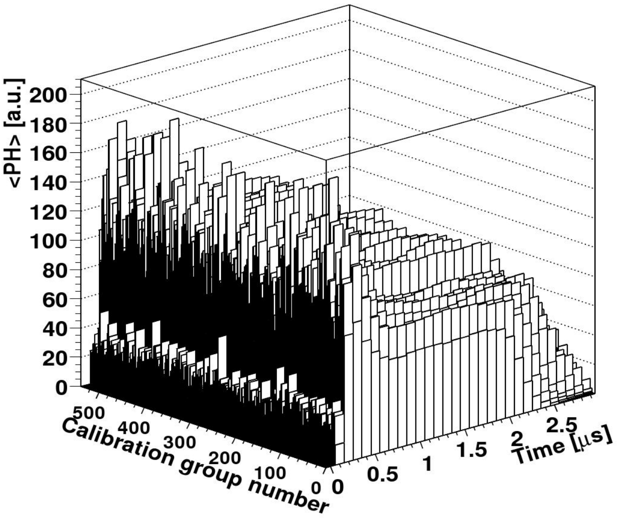

Figure 5.2: Simulation of the average pulse height $\langle PH \rangle$ for the whole TRD where each calibration group corresponds to one readout chamber [Bai09].

5.4 Gain Calibration

The relative gain factors can either be determined by a comparison to a default ideal gain factor or to previously determined gain factors from earlier caibrations. This approach allows for monitoring changes of the gain over time. Moreover, it can be used to suppress systematic errors and uncertainties. The relative gain factors are retrieved from dE/dx spectra for the chosen calibration groups. The spectra for the calibration groups according to the chosen granularity settings are generated by the same macros and classes that are used to determine v_{drift}.

5.4.1 Filling of the Energy Loss Spectra

The dE/dx distribution is filled for each calibration group by `AliAnalysisTaskTRDCalib.cxx` which calls the class `AliTRDCalibraFillHisto.cxx`. This is done by determining the energy loss per unit length from information stored in `AliESDs.root`. Such a dE/dx distribution (proportional to deposited charge normalized with dx) is shown in figure 5.3. The x-axis shows the energy loss distribution, the calibration groups can be found on the y-axis. A projection of the spectra on the x-axis gives the dE/dx distribution. The spectra are also stored in `TRDCalibration.root` [Gat10].

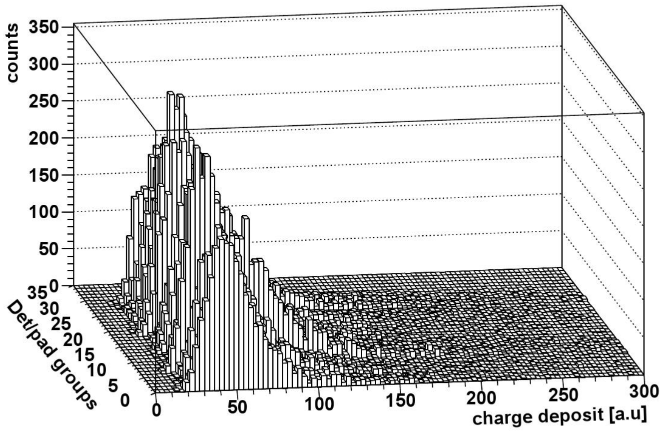

Figure 5.3: A 2D histogram containing the dE/dx distributions (charge deposit normalized by distance traveled) of 30 calibration groups (readout chambers in SM-II) taken from run 1899 [Alb10].

Gain factors of either the default OCDB value $g = 1$ or the previously determined gain factors are taken into account for raw data reconstruction. As these factors influence the reconstruction output, they also influence the gain calibration. Consequently, the path of the OCDB that was used for reconstruction has to be stated during calibration [Gat10]. As mentioned in sections 5.1 and 5.3.2 the pass0 and pass1 reconstruction deploy different OCDBs.

The incidence angle of the particle with respect to the sensitive plane influences the amout of energy loss in the chambers. This means that particles with a flat polar angle θ deposit more energy in the gas because they travel a longer distance in the detector. Accordingly, the dE/dx spectra are corrected for the determined track angle [Gat10].

5.4.2 Determination of the Relative Gain Factors

The macro `determineCoeff.C` is again used to process `TRDCalibration.root` and calculate the gain factors by using the same classes as before.

The distribution of the particle energy loss in the chambers has the form of a Landau distribution, as discussed in section 3.5. The gas gain can be characterized by its most probable value which is, in contrast to its mean value, less susceptible to the long ion tails at the end of the pad signals [Gat10]. Various gain calibration methods are implemented in the macros. In this thesis the weighted mean method was chosen because it provides a high accuracy combined with the shortest CPU time of all available methods [Gat10].

The dE/dx distribution is evaluated as a function $N(\Delta E)$ which is the number of tracks (particles) having deposited the energy ΔE in the readout chamber. The weighted mean M_w is defined as:

$$M_w = \frac{\sum_i f_w(\Delta E_i) \cdot N(\Delta E_i) \cdot \Delta E_i}{\sum_i f_w(\Delta E_i) \cdot .N(\Delta E_i)} \tag{5.3}$$

In this equation $f_w(\Delta E_i)$ denotes the positive weight function with $0 \leq f_w(\Delta E_i)$. For $f_w(\Delta E_i) = 1$ the weighted mean would equal the mean energy loss. The weight function has to be determined once from a typical dE/dx spectrum. For this purpose a function

$g(\Delta E)$ is parametrized with the values a, b, c, d, e to

$$f_w(\Delta E) = a + b \cdot g(\Delta E) + c \cdot g(\Delta E)^2 + d \cdot g(\Delta E)^3 + e \cdot g(\Delta E)^4 \tag{5.4}$$

with $g(\Delta E)$ defined as

$$g(\Delta E) = \frac{\sum_{i=bin(0)}^{bin(\Delta E)} N(\Delta e_i)}{\sum_i N(\Delta e_i)} \qquad \epsilon\ [0,1]. \tag{5.5}$$

An energy loss ΔE is chosen and the number of particles depositing an amount of energy equal to or lower than this value is determined. This number is divided by the total number of particles. The procedure is repeated for all possible ΔE. The determined $g(\Delta E)$ is then inserted into equation 5.4. The parameters a, b, c, d, e are adjusted to achieve the same result of M_w as for the most probable value with a convolution of Landau distribution and Gaussian fits [Bai09]. The weighted mean function has been determined and stored in an AliRoot class. In order to achieve an acceptable error of $\sigma_{\text{relative}} \leq 5\%$, at least 100 tracklets per calibration group have to be reconstructed (cf. section 6.1). The determined gain factors are stored in an OCDB file.

5.5 Execution of the Calibration Procedure

The macros and OCDB objects needed for the calibration and alignment procedure are located in the folder `reco_and_calib` on the MAF computer cluster in Münster. This folder contains subfolders for the four calibration steps and analysis macros for the determined calibration parameters. The pass0 subfolder also includes a `fake_objects` folder with global run parameter objects needed during the calibration. The subfolder `default_OCBDs` contains OCDBs with different drift velocities and general information for each run which is used for reconstruction. The order of the calibration should be:

1. Pass0 reconstruction with the default OCDB.
2. Calibration of the drift velocity.
3. Pass1 reconstruction using the OCDB created in the former calibration step.
4. Calibration of the gain factors.

The calibration data is stored in the folder `/gluster/c_witt19/data/SM16/<run>` with `<run>` being the run number. This folder contains subfolders for pass0, drift velocity, pass1 and gain calibration.

5.5.1 Pass 0 Reconstruction

Before the start of the pass0 reconstruction settings in the shell script `start_pass0.sh` have to be adjusted. The environment variables for the supermodule (`sm=16`) and run number (e.g. `run=3085`) have to be changed and the numbers of the files that shall be reconstructed have to be specified (e.g. `file=1,fileend=33`). Then the macro can be executed.

Folder for the reconstructed files are created if they do not already exist. A single file with raw data contains up to 150000 events and is reconstructed in intervals of 2500 events. For each interval `start_pass0.sh` creates a job by submitting the executable script `pass0_resolution_tmp.sh` to the batch server. The scripts are then stored until they are executed. This happens as soon as enough computing resources are available on the computer cluster. The script creates a subfolder for its assigned interval in the file folder and starts the reconstruction by calling the reconstruction macro `rec_new.C`. The standard output and error messages are recorded in the files `outRES.bz2` and `errRES.bz2` and saved in the interval subfolders together with the rest of the reconstruction output.

5.5.2 Drift Velocity

After the first reconstruction of a run the drift velocity can be determined. The macros needed for the drift velocity calibration can be found in the `v_drift_new` subfolder. Again the supermodule and run numbers have to be changed in the shell script `start_vdrift`. Additionally, the desired granularity (nz,$n\phi_r$) has to be specified. If the number of tracklets per calibration group is smaller than 100 tracklets the drift velocity is set to the default value of 1.5 cm/µs which can differ from the actual value to a great extent depending on the drift voltage in the chamber. As the precise knowledge of the actual drift velocity is crucial for the pass1-reconstruction, the granularity should be chosen accordingly.

The shell script `start_vdrift` submits `vdrift_tmp.sh` to the batch server. A text file with a list of all `AliESDs` and `AliESDfriends` from the pass 0 reconstruction is created by the macro `CreateTextFileESD.C`. This list is passed to `runTask2.C` which fills the histograms of pulse height spectra and stores them in the file `TRDCalibration.root`. The standard as well as the error output are stored in the output folder `/gluster/c_witt19/data/SM16/<run>/v_drift` as `outRT.bz2` and `errRT.bz2`. The `TRDCalibration.root` is then processed by `determineCoeff.C` which retrieves the drift velocity values from the spectra. The standard output `outDC.bz2` and error outputerrDC.bz2 are saved in the drift velocity folder. The determined values of v_{drift} are stored in a local OCDB in the subfolder `TRD/Calib` [Gat10].

5.5.3 Pass 1 Reconstruction

The pass0- and pass1-reconstruction use the same scripts and macros. The only difference to the first reconstruction is that the path of the `V_drift_OCDB` is set to the one created in the drift velocity calibration, which is stored in the folder `/gluster/c_witt19/data/SM16/<run>/v_drift/TRD/Calib`. The reconstruction output is saved in the folder `/gluster/c_witt19/data/SM16/<run>/pass1` with the respective subfolders for the different files.

5.5.4 Gain

The gain calibration uses the same macros as the drift velocity calibration and utilizes similar shell scripts. As stated before the histograms with the dE/dx spectra are also filled when running the `runTask2.C` macro that uses `determineCoeff.C` to obtain the relative gain factors for the calibration groups. The output of the gain calibration is stored in `/gluster/c_witt19/data/SM16/<run>/gain` with the gain factors being saved in an OCDB in the subfolder `TRD/Calib`. The size and shape of the calibration groups should be set by changing the granularity settings (nz,$n\phi_r$) [Gat10].

5.6 Modifications of AliRoot v5-04-Rev-18

The previous run calibration was carried out four years ago using Root v5-26-00 and AliRoot v4-18-Rev-01. Initially none of the four calibration steps produced results using the current Root v5-34-18 and AliRoot v5-04-Rev-18. Employing an older AliRoot version for this thesis was not an option as it was not compatible with the recorded raw data. Several code revisions had to be applied in the reconstruction and calibration macros, but most importantly the used AliRoot version required modifications. This section will highlight a few of the compatibility issues that have been encountered and fixed in the course of this thesis.

5.6.1 Custom OCDBs

The standard AliRoot comes equipped with default OCDB files for all detectors that can be used for offline reconstruction and analysis. However, the reconstruction had to be performed using a custom OCDB. As stated before this has been done for two reasons: First, it enabled the choice of different default values for parameters such as the drift velocity during reconstruction. For this purpose a macro for creating dummy OCDBs was provided. Second, it was necessary as the provided default OCDBs were incompatible with the raw data recorded in Münster. The amount of timebins in the TRD raw-files in ALICE has been reduced to 24 timebins while the raw data recorded in Münster still uses 30 timebins. For this reason the functionality of the macro `CreateDummyOCDB.C` had to be enhanced in order to create a full set of OCDB files needed for reconstruction and calibration. This was aided to a great extent by B. Bathen.

5.6.2 Changes in AliRoot Classes

In addition to the creation of a set of new OCDB files code lines in a few classes had to be changed. The alterations include:

- `AliTRDtrackerV1` and `AliTRDRecoParam`: The χ^2_y-, χ^2_x- and likelihood filters can now be switched on and off for reconstruction.
- `AliTRDCalibraFillHisto`: Initializations for some histograms have been inserted. The lack of these caused the macro to crash. Also commands for using the correct OCDB have been added.

- `AliTRDCalibraFit`: The histograms from the debug output of `determineCoeff.C` are now saved in files. This way the functioning of the fitting algorithm applied to the energy loss- and pulse heigt-spectra can be investigated.

With these changes in place the reconstruction and calibration macros show the desired functionality. The calibration results are presented in the next chapter.

6 Gain Calibration of the TRD Supermodule

In this section the calibration results for the relative gain factors for SM-XVI[1] are presented and discussed. This is done both for the standard voltages used during testing in Münster and for different voltages in order to assess their impact on the relative gain. In pursuance of improving tracklet counts in the calibration groups the impact of reconstruction filters on the calibration output is investigated. In the last section difficulties with the determination of the drift velocity are discussed.

6.1 Determination of the Relative Gain Factors

The relative gain factors determined in a pad-wise calibration are displayed for all six SM layers in figure 6.1.

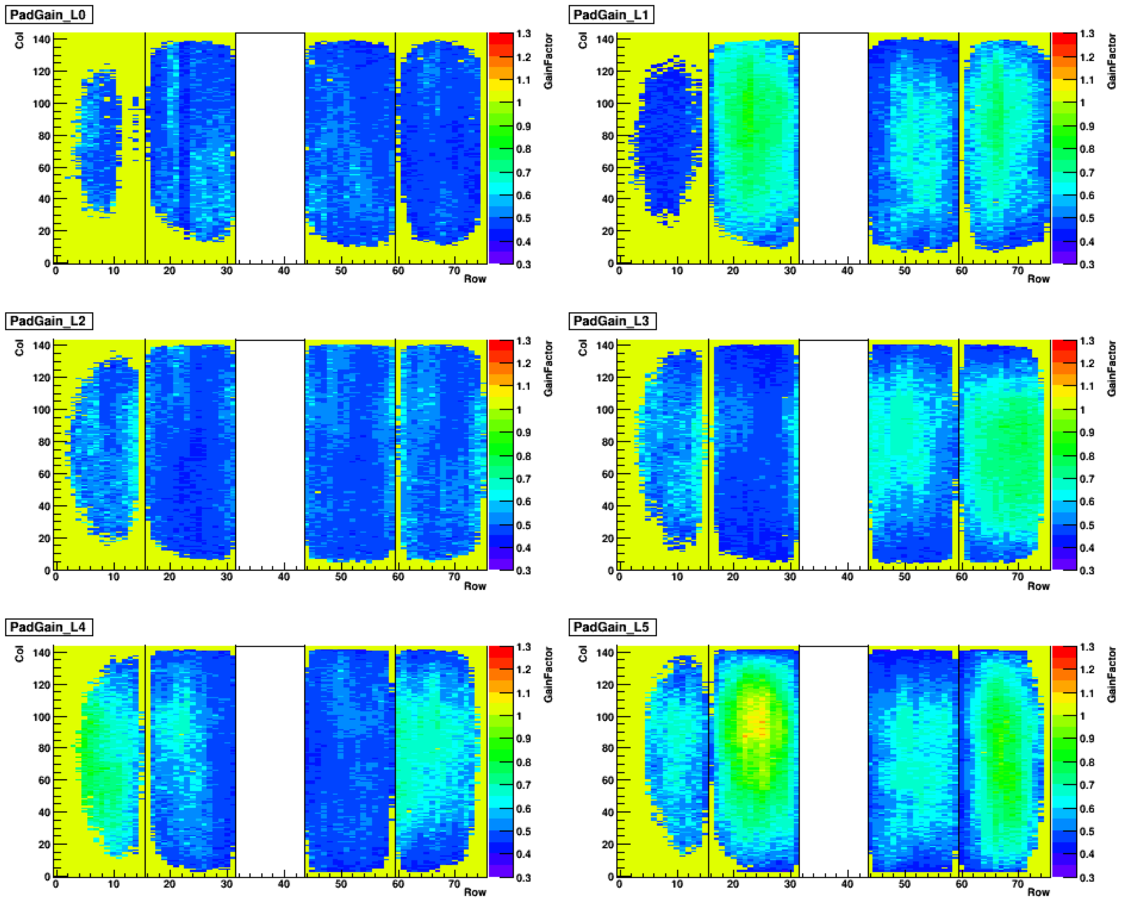

Figure 6.1: Relative gain factors for run 3075 with 8,426,617 events at $(nz,n\phi_r) = (4,6)$. Each calibration group (bin in the plot) corresponds to one cathode pad.

---

[1] SM-XVI underwent final assembly in Münster from February to April 2014.

This run used the standard voltage settings for an Ar/CO$_2$ gas mixture of $U_{\text{Anode}} = 1500$ V and $U_{\text{Drift}} = 1500$ V. The gain factors are shown for the six layers of the supermodule starting with layer 0 in the top left and ending with layer 5 in the bottom right corner. Chamber borders are indicated by vertical lines. Stack 2 is left blank because it is not installed in SM-XVI which is located in front of PHOS in ALICE.
The large yellow areas of $g = 1$ are due to insufficient statistics which match the illumination scheme from figure 4.7. The calibration groups with less than 100 tracklets were excluded from the analysis and set to $g = 1$ by the software. This makes the affected calibration groups unavailable for analysis. Given that the statistics cannot be increased, smaller granularities have to be chosen. For long runs with more than 10^6 events $(nz, n\phi_r) = (4,3)$ has been proven reasonable. At this granularity each calibration group consists of 1 pad in row direction and 18 pads in column direction, so every group is read out by one MCM. Shorter runs with about 10^5 events have been examined chamber-wise with $(nz, n\phi_r) = (0,0)$.

The same run is depicted in figure 6.2 now at (4,3) granularity. At this granularity the only calibration group having been set to default values is located in layer 4, stack 0, columns 0-17, row 0.

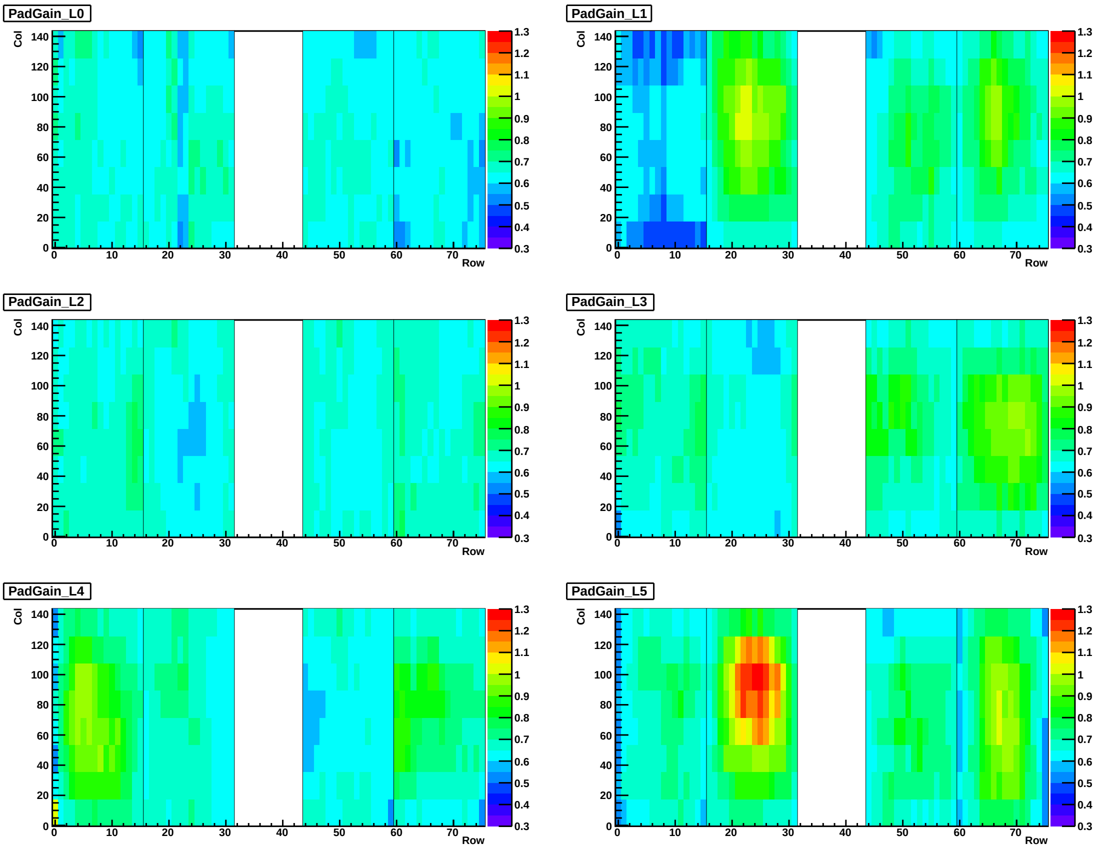

Figure 6.2: Relative gain factors for run 3075 with 8,426,617 events at $(nz, n\phi_r) = (4,3)$. Each calibration group comprises 1 row and 18 columns.

Several observations have been made in the results of the calibration procedure. Run 3075 has been chosen as an example for its high event count with more than $8 \cdot 10^6$ events. The observations from this run have also be made in other runs.
Most ROCs show a higher relative gain in the center than at the chamber edges. Prominent

examples are stacks 1, 3 and 4 in layer 1, or stack 4 in layer 5. It has been suggested that this is due to a rise of the electric field towards the center of the chambers [Gat10]. The electrostatic attraction between the positively charged anode wire and the grounded pad plane and cathode wires causes the wire to bend towards both components. The anode and cathode wires are less stable then the pad plane causing both to bend in the pad plane direction.

The gain factors which were determined by the calibration software are unexpectedly low. The relative gain ranges between 0.5 and 1.3 with a mean gain of 0.692 over all calibration groups. This has been found to be the case for almost all runs[2]. At the chamber edges relative gain factors of 0.5 or lower have been observed. In the center of the chambers values of 1.0 or higher can be achieved, for example in stack 1 and 4 in layer 1 or stack 4 in layer 3 and 5. Stack 1 in layer 5 shows unusually high gain factors of up to 1.3. In layer 2 relative gain factors do not exceed 0.7.

The gain calibration is a relative calibration. The energy loss in the chambers is compared with an energy loss reference value. This value is given by the OCDB used in the calibration. If the used reference value corresponds to simulated proton-proton events the overall relative gain can be systematically lower. This would be due to the fact that dE/dx is smaller for cosmic particles than for particles created in pp-collisions [Bai14]. Further investigation is needed in order to test whether the observation is caused by an actual low gain in the ROCs or by pp-reference values.

A low gas gain in the chambers can be caused by several factors:

- A contamination of the Ar/CO_2 mixture with air leads to a lower gas gain because it acts as an additional quenching gas in the chambers [And04].
- The differential pressure between the gas in the chambers and the atmosphere. It has been predicted by [ALI01] and shown in [Alb10] that an overpressure inside the chambers causes a drop of gas gain. This is a result of the pad plane bending outwards due to the pressure gradient. An overpressure of 1.0 mbar results in a $5-7$ % decrease in gain.

As both effects are relatively small they are not sufficient to account for overall low gains. A systematic effect caused by the calibration software has to be considered. In this case the gain results for the ROCs should show the same behavior as in previous works with the absolute values deviating.

6.1.1 Comparison with Previous Measurements

A calibration of the relative gain factors using the same reconstruction and analysis framework has been performed previously in Münster by H. Gatz and B. Albrecht for their diploma theses [Gat10] [Alb10]. Both used an older version of AliRoot (AliRoot v4-18-Rev-01) and looked at different supermodules, but essentially put the same methods and macros to use.

In [Gat10] SM-VI was examined at a (3,4) granularity. It was also observed that the

---

[2] For a few early runs shortly after the installation of layer 5 unusually high gain values were determined for this layer. The results for these runs can be found in the appendix section 8.4.

relative gain factors in the entire supermodule were systematically too low. The gain profile of the chambers also showed a rise towards the center of the chambers. Similar explanations have been suggested, but the OCDB reference values have not been taken into account. An unusually high gain was found in layer 4, stack 4. An explanation for this behavior was not found.
In [Alb10] the relative gain for SM-I was determined at a (4,5) granularity, i.e. 1 pad in row and 4 pads in column direction. This could be achieved by acquiring more statistics owed to a 300 Hz recording rate and a presumably longer measurement period. For layers 0 to 4 gain factors of 0.7 to 1.4 have been found in the analysis, also with the tendency towards a rise to the chamber center. Problems with the tracking software have lead to unlikely gain factors higher than 2.0 in layer 5, so it has been excluded from the analysis. A mean relative gain $M_{1a} = 1.077$ of all pads was found. Further analysis in [Alb10] included investigations of the effect of anode voltage and differential pressure on the gas gain. Together with tests of the calibration software the concordance of these investigations' results with theoretical predictions served as a positive test of the calibration software.

The results obtained for the SM studied in this thesis are in good concordance with results from H. Gatz' thesis [Gat10] with systematically too low gain factors and rising relative gain towards the chamber centers. The observation regarding the gain profile was also made in [Alb10]. For this reason it is likely that the low relative gain determined in this thesis is caused by the reference value from the used OCDB. Still, it has to be investigated whether the calibration software produces reliable results with a newer AliRoot version that needed to be heavily modified in order to get the reconstruction and analysis to work. This is attempted by examining the dependence of the relative gain on anode voltage and comparing the found dependence with previous works.

6.2 Accuracy of the Calibration Procedure

It has been shown that the accuracy of the weighted mean method for gain calibration scales with the number of analyzed tracklets per calibration group [Bai09]. This is due to the fact that the dE/dx distributions are more accurate for large numbers of entries. The relative standard deviation of gain factors that were determined using the weighted mean method have been estimated by cosmic ray measurements [Alb10]. It was found that the relative standard deviation ranges between $1 - 4$ % for small numbers of entries and saturates at $0.5 - 1.0$ % for more than 40,000 entries per calibration group. A further analysis had to be carried out with simulated data because only then stable gain factors could be achieved. These are crucial for such an analysis as a variation of gain over time also leads to deviating gain factors. The variations are then not only caused by the calibration software, but by gas pressure changes or chamber deformations due to a drop of ambient temperature.
An empirical formula for the relative error σ_{relative} has been derived [Bai09] in the analysis

based on simulated data:

$$\sigma_{\text{relative}}(n) = \frac{\sigma_g}{g} = \begin{cases} \left(\frac{41.428}{\sqrt{n}} + 0.685\right) \% \text{ for } n \geq 100, \\ 0\,\% \text{ else.} \end{cases} \tag{6.1}$$

The standard deviation was defined as 0 for $n \leq 100$ in order to avoid unrealistic error bars for small numbers of events. Accordingly, a calibration should only be performed with at least 100 events. For the calibration in this thesis $n = 100$ has been chosen as the threshold for the minimum number of tracklets contained in each calibration group. This translates to a maximum $\sigma_{\text{relative}} \approx 4.83$ %. Groups with less tracklets have been set to default values in the calibration.

6.3 Gain Results for Different Reconstruction Parameters

It has been stated before that the cut on track likelihood rejects 100 % of the cosmic TRD tracks in Münster, which makes an offline calibration impossible. For this reason the cut on track likelihood has been switched off. The χ_x^2 and χ_y^2 cuts have been left active for reconstruction, which caused an overall track rejection of about 50 % of all recorded events. This limited the available statistics for gain calibration. It would be desirable that all recorded events actually produced tracks usable for an analysis. This motivated an analysis of the impact, the filters have on the calibration output.

Ten files from run 3072 have been reconstructed with four different filter combinations (both, none, χ_x^2 on and χ_y^2 off, and vice versa). The numbers of reconstructed tracks that were analyzed in the calibration have been extracted from the `TRDCalibration.root` and are given in table 6.1.

Configuration	Activated Filters	Analyzed Tracks
1	χ_z^2, χ_y^2	427790
2	χ_y^2	539836
3	χ_z^2	492641
4	none	384774

Table 6.1: Number of analyzed TRD tracks in the calibration of 10 files from run 3072. The configuration numbers give the different filter combinations in reconstruction and correspond to the ones in figure 6.3.

Switching off either the χ_z^2- or χ_y^2-filter adds about 15-27% more tracks available for calibration compared to the number available with both filters turned on. In turn, one would expect to have roughly 40% additional tracks with both filters switched off. However, this is not the case. For some reason the number of analyzed tracks even drops from 427,790 to 384,774. Although the reason for this has not been found yet, it appears reasonable to switch off the χ_z^2 filter for reconstruction, provided this does not change the calibration results.

The relative gain is determined at (0,0) granularity for the four different sets of reconstructed data. The results can be seen in figure 6.3. The numbers on the x-axis correspond to the filter combinations used in the reconstruction: Both filters engaged (1), χ^2_z off (2), χ^2_y off (3), and both filters off (4). The errors for the relative gain and the mean gain were determined with equation 6.1, but are not visible in the plots.

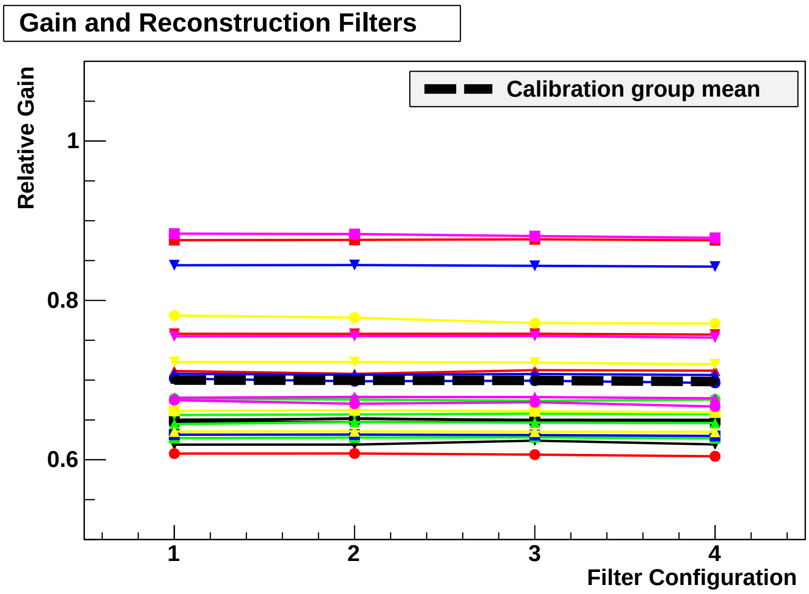

Figure 6.3: Relative gain for different filter combinations used in the raw data reconstruction. Numbers on the x-axis correspond to the filters: both filters engaged (1), χ^2_z off (2), χ^2_y off (3), and both filters off (4). The gain was determined at (0,0) granularity for ten raw files from run 3072. Errors for the gain factors were left out while errors for the mean gain are not visible in the plot.

It can be seen that a few calibration groups show slight variations for different filter combinations. However, the mean gain for all 24 chambers is stable. The variation in gain for the different filter combinations is smaller than the assumed errors caused by the calibration software. The values can be found in table 6.2.

Configuration	Engaged Filters	SM Mean
1	χ^2_z, χ^2_y	0.7000 ± 0.0022
2	χ^2_y	0.6998 ± 0.0022
3	χ^2_z	0.6996 ± 0.0022
4	none	0.6982 ± 0.0022

Table 6.2: Mean Gain of all calibration groups (24 chambers of the SM) for different filters used during the reconstruction of run 3072. The errors for the mean gain were calculated using equation 6.1 and Gaussian error propagation.

It is concluded that the χ^2_z- and χ^2_y-filters do not have a noticeable effect on the calibration output when analyzing cosmic ray data. Thus, the number of tracks available for calibration can be boosted by switching off one of the filters, with the χ^2_z-filter having a greater effect. Switching both filters off leads to an undesirable drop in usable tracks found in the reconstruction. The reason for this remains to be investigated.

6.4 Anode Voltage Influence on Relative Gain Factors

The relative gain in the ROCs is highly dependent on the applied anode voltage, as outlined in section 3.2.3. An exponential dependence of gain on the anode voltage is expected from electrostatic calculations [ALI01] and has been shown by B. Albrecht in [Alb10]. This measurement has been carried out with an older version of AliRoot. Several compatibility issues have emerged in the recomissioning of the analysis framework with a recent AliRoot version. The investigation of the relative gain as a function of anode voltage can serve as a verfication of the correct functioning of the analysis framework.

6.4.1 Measurement of Gain Factors for Different Anode Voltages

The calibration for this analysis was carried out chamber-wise with (0,0) granularity. Higher granularities could not be investigated because these measurements were conducted last and time was limited due to the shipping date of SM-XVI. For anode voltages of 1400 V (Run 3094), 1460 V (Run 3095), 1480 V (Run 3093), 1500 V (Run 3071) the gain factors were determined with the calibration software. It has been observed that the trigger rate dropped for lower anode voltages. The minimum energy needed for signal generation in the chambers increases with a lower anode voltage. Therefore, tracks of cosmic particles below this energy are not registered.

Passing a default OCDB to the calibration software was required in order to compare different runs [Alb10]. In addition to being mutually calibrated the relative gain factors of every calibration group are compared to previous signal amplitudes. These previous amplitudes have to be the same for all compared runs. This is achieved by using a default OCDB with a homogenous gas gain of $g = 1$ for a standard signal amplitude.

6.4.2 Results

Figure 6.4 shows the relative gain as a function of anode voltage U_{Anode} for the investigated calibration groups at a (0,0) granularity (24 chambers in 6 stacks). Each colored line corresponds to one calibration group. The dotted line is the mean of all calibration groups. The errors of the gain factors are computed according to the empirical formula from section 6.2. All analyzed calibration groups contained more than 2000 events, hence the highest relative errors had a magnitude of 1.5 % which is too small to be visible in the plots. This also holds true for the errors for U_{Anode}, as it can be chosen with a precision better than 1 V.

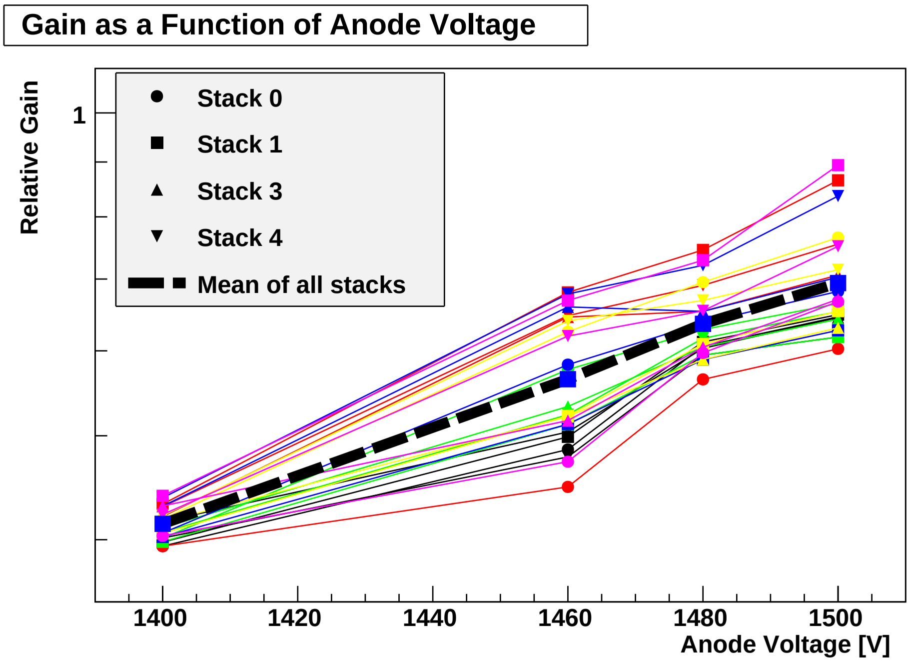

Figure 6.4: Gain as a function of anode voltage on a logarithmic scale for 24 calibration groups. The relative gain was determined at (0,0) granularity (6 chambers in each of 4 stacks) for four runs with different anode voltages (1400 V, 1460 V, 1480 V, 1500 V). The dotted line represents the mean of all chambers.

Looking at figure 6.4 one can distinguish two trends. For 16 of the 24 calibration groups the relative gain shows the expected exponential dependence on anode voltage, although the increase seems to level off slightly between 1480 V and 1500 V. In earlier measurements from [Alb10] the increase between 1400 V and 1500 V was stronger than exponential. This was attributed to a sagging of the anode wires towards the pad plane. The divergence from earlier measurements can have several reasons:

- The relative standard deviation of the gain factors might be higher with the new AliRoot version due to probable systematic errors in the determination of the relative gain. Such errors are not accounted for by the assumed standard deviation of about 1.5 %.

- Run durations ranged between 1 and 11 hours, so for the longer runs variations of gain over time might have had an effect, which has not been incorporated in the error bars. An additional investigation of gain variation over time might be of future interest in order to assess its impact on the results.

- In a previous measurement by B. Albrecht a finer (3,3) granularity and more calibration groups were used. The resulting higher statistics helped to keep an impact of deviating calibration groups on the mean value low. This could not be achieved with a (0,0) granularity. Furthermore, the higher granularity could be used in order to investigate local differences. Although it has been shown that the dependence of gain on the anode voltage is not influenced by the pad position, large gain differences within a chamber can have an effect on the cumulative chamber result. In order to assess this, an investigation at higher granularity would be needed. Yet, it is not possible with the recorded data.

For half of the groups the relative gain is lower than expected at 1460 V. It could not be found that a certain stack or layer is affected, but rather those calibrations groups with overall lower g.
Run 3095 was recorded over night and lasted 11 hours making it the longest of the investigated runs. The deviating relative gain in this run is possibly a result of gain variations over time. As the run was recorded over night a drop of ambient temperature with the associated drop of air pressure could have lead to an overpressure in the chambers causing the pad plane to bend outwards. For a 1.0 mbar drop in pressure an expected gain of 0.50 would decrease to about 0.47. The actual values range between 0.42 and 0.46, which is too low to be caused only by a pressure gradient. So far, it is under investigation why only certain groups are affected.

In order to review the gain's stability the relative gain for three different periods of run 3095 were determined. Five files from the beginning, middle and end of the run were calibrated at (0,0) granularity with the result shown in figure 6.5.

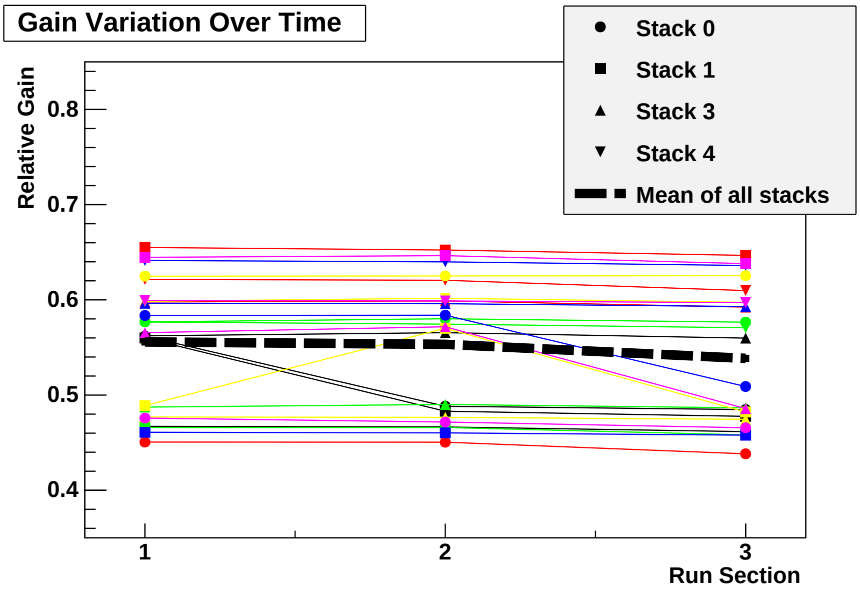

Figure 6.5: Variation of the relative gain factors in 24 calibration groups over time taken from run 3095. The variation of the gain is plotted at three points in time from the beginning (1), through the middle (2) and end (3) of the 11 hour run. The mean gain is indicated by the black dashed line.

With the exception of five chambers all calibration groups show a slight decline in relative gain, with the mean gain decreasing from 0.56 ± 0.01 to 0.53 ± 0.1. This is a $5 - 9$ % drop, a value of the scale that would be expected for a continuously decreasing ambient pressure. As the mean gain for the whole run is a mean over all files the effect should be considerably smaller for the whole run. Therefore, it is not sufficient to account for the unexpectedly low gain values. The deviating chambers are located in layer 0 (stack 0, stack 1), layer 3 (stack 0), layer 4 (stack 1) and layer 5 (stack 3). These chambers are among those that show unexpectedly low gain values in figure 6.4. The reason for the strong variations over time in these groups is not clear at this point.

6.4.3 Investigation of Exponential Behavior

The mean gain of 24 calibration groups for 1400 V, 1460 V, 1480 V and 1500 V has been fitted with an exponential function. The result is depicted in figure 6.6.

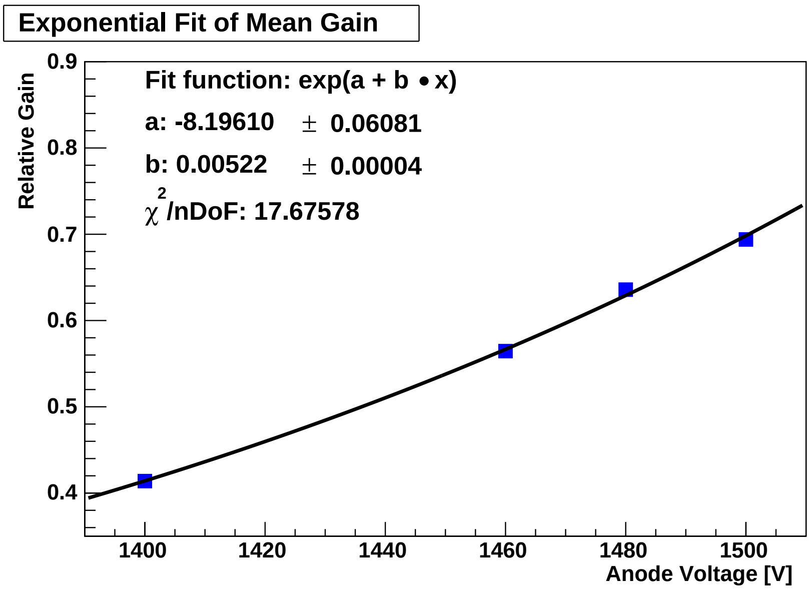

Figure 6.6: Exponential fit of mean relative gain against the applied anode voltage in 24 calibration groups (chambers) in SM-XVI. The dots represent the mean values of all calibration groups, the black line is the exponential fit.

The expected exponential dependence of g on U_{Anode} can be observed, although the fit function barely crosses all points and their small error bars. As stated before, it has to be assumed that the errors were assumed lower than they actually are. Additionally, it has been found in previous works that the dependence is not perfectly exponential [Alb10]. The fit function

$$g(U_{\text{Anode}}) = \exp\left[(-8.20 \pm 0.07) + (5.22 \cdot 10^{-3} \pm 0.04 \cdot 10^{-3}) \cdot \frac{1}{\text{V}} \cdot U_{\text{Anode}}\right] \tag{6.2}$$

has been found with $\chi^2/\text{nDoF} = 17.68$. The relative rise in gain for a 1 V increase of U_{Anode} can be calculated by deriving the fit function:

$$\frac{dg}{dU} = (0.52 \pm 0.01)\,\frac{\%}{\text{V}} \quad \text{for } \Delta U = 1\,\text{V}. \tag{6.3}$$

6.4.4 Comparison with Previous Measurements

The influence of the applied anode voltage on gain in the TRD chambers has been investigated before with electrostatic calculations [ALI01] and by experiments with cosmic rays in Münster [Bai09] [Alb10]. Further measurements utilizing radioactive sources and their concordance with cosmic ray data are described in [Alb10] and will not be discussed here.

Work	Voltage Range [V]	Gas Mixture [%]	Granularity
Own	1400 - 1500	Ar/CO$_2$(82/18)	(0,0), 24 calibration groups, whole SM
[Alb10]	1400 - 1500	Ar/CO$_2$(83/17)	(3,3), 384 calibration groups, one stack
[Bai09]	1420 - 1600	Ar/CO$_2$(63/37)	Whole SM

Table 6.3: Different measurements of the relative gain factors as a function of anode voltage in the TRD chambers.

An early version of the calibration software was used for the measurements carried out by R. Bailhache and less data was calibrated than in this thesis. Measurements were performed with the whole SM as a calibration group. The measurements by B. Albrecht utilized a newer version of the software, the investigated datasets were larger and the analysis could be carried out at a higher (3,3) granularity. All three measurements used different gas mixtures. In order to compare the results of the measurements carried out with different supermodules and versions of the software, the relative gain factors have been normalized to $g(1500\text{ V}) = 1$. The comparison of the $g(U)$ results is displayed in figure 6.7.
The uncertainties in both other works are similar to the ones in this thesis which is not surprising given that the same formula for error estimation was used. This makes the error bars too small to be visible. While the results from [Bai09] and [Alb10] comply well, the current results do not match both previous measurements. The exponential increase of the voltage shows a much lower slope. This becomes evident when looking at the relative rise dg/dU in gain for $\Delta U = 1$ V which was calculated for different measurements in [Alb10]. The comparison is depicted in figure 6.8.

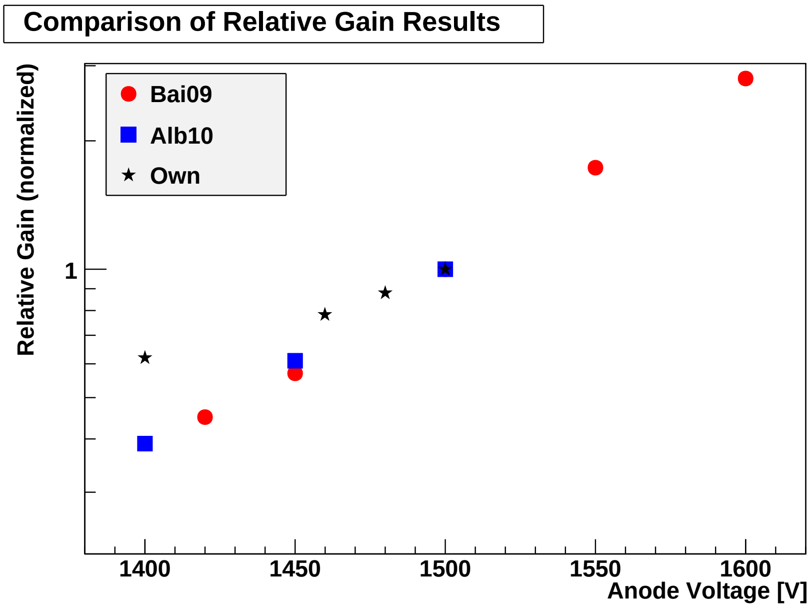

Figure 6.7: Comparison of the $g(U)$ results with previous measurements taken from [Alb10] and [Bai09]. Each measurement was normalized to $g = 1.0$ for $U = 1500$ V.

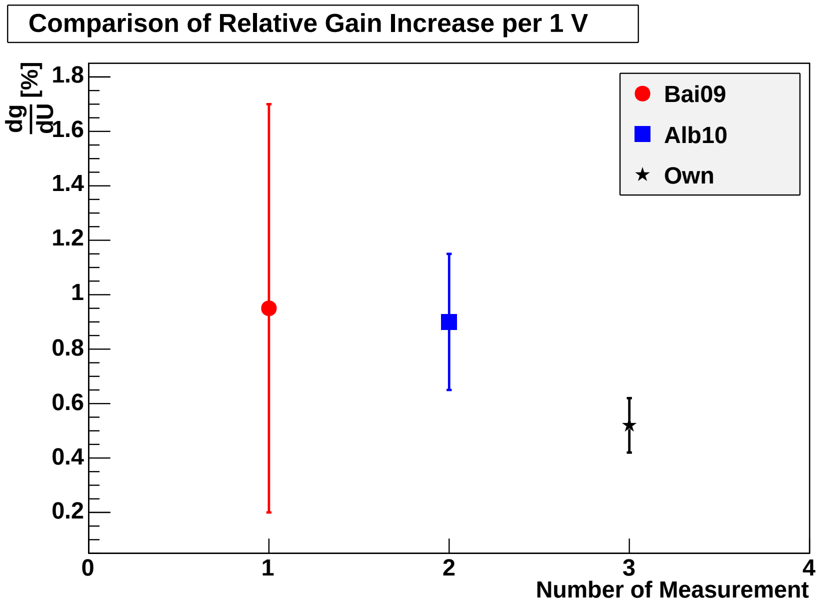

Figure 6.8: Comparison of relative gain increase for $\Delta U = 1$ V with previous measurements taken from [Alb10]. Here dg/dU was calculated from the fit functions to the respective measurements. The errors are a result of uncertainties of the fit parameters.

Although the error bars of all three values overlap, dg/DU is about 50% lower in this thesis than in the other works. In addition to being mutually compatible the results from [Bai09] and [Alb10] comply with electrostatic calculations from [ALI01] and results acquired by different experimental approaches [Alb10]. This has been regarded as a positive test of the analysis software. The deviation of the values in this thesis might be a result of the overall lower relative gain determined by the software. Regardless, if only systematic effets play a role, the results should be comparable after the normalization. As the change of the mean relative gain in the whole supermodule was inspected, discrepancies between chambers might have affected the result. In this case a chamber-wise investigation might be of interest.

6.5 Determination of the Drift Velocity

An examination of the drift voltages' effect on the drift velocities has been carried out for several runs at different voltages. This analysis has shown that the software algorithm for determining v_{drift} does not produce reliable results. The drift velocities for run 3075 ($U_{\text{Drift}} = 1500\,\text{V}$) are shown in figure 6.9[3].

---

[3] The drift results for more runs and different granularities can be found in section 8.5 in the appendix.

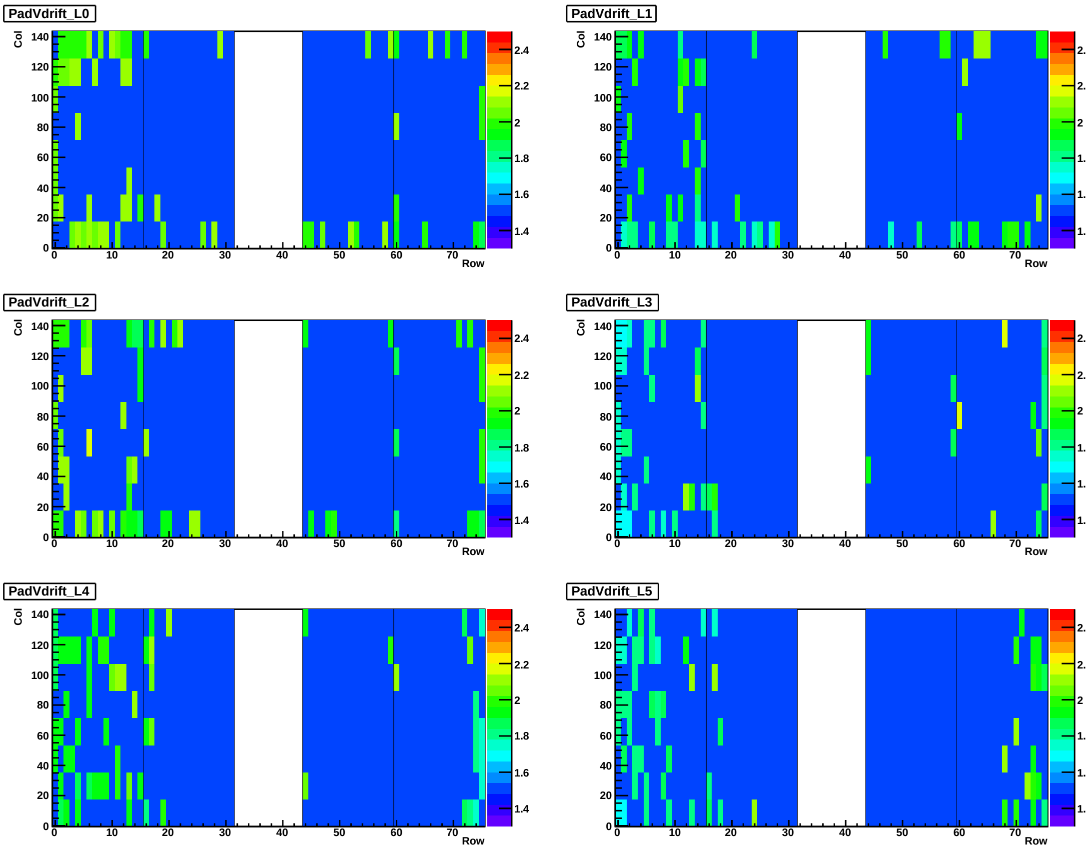

Figure 6.9: Drift velocity for run 3075 determined at (4,3) granularity.

Nearly all calibration groups are set to the default value $v_{\mathrm{drift}} = 1{,}5$ cm/µs with only few groups being set to reasonable values of around $2 - 2.5$ cm/µs [Alb10] [Gat10]. This is caused by a failure of the fitting algorithm used on the pulse height spectra. As described in section 5.3.2, the beginning of the signal, as well as the start and end of the drift region are determined by fitting a polynomial to the the pulse height spectra. The beginning t_{A} of the drift region is found at the maximum of the polynomial. The start of the signal t_0 and the end of the drift region t_{D} are found at the reversal points. By looking at the debug output of the calibration macro `determineCoeff.C` it has been found that the algorithm identifies $t_{\mathrm{D}} = 0$ µs which causes the calculated drift time to be negative. In this case the default value for the drift velocity is set.

Figure 6.10 shows the debug output with the fitted pulse height spectra of `determineCoeff.C` for run 3093 and 3095. The runs show the same irregularities as run 3085 and were chosen because of their different pulse height spectra. In figure 6.10 these are indicated by blue crosses with the red line being the polynomial fit. The red vertical lines signify t_0, t_{A} and t_{D}. The x-axis shows the time in μs and the y-axis is the pulse height in arbitrary units. The algorithm should have found t_{D} at around 1.6 µs (left) and 1.4 µs (right) in the spectra. With t_{A} at about 0.4 µs in both spectra drift velocities of $2.5 - 3.0$ cm/µs should have been found.

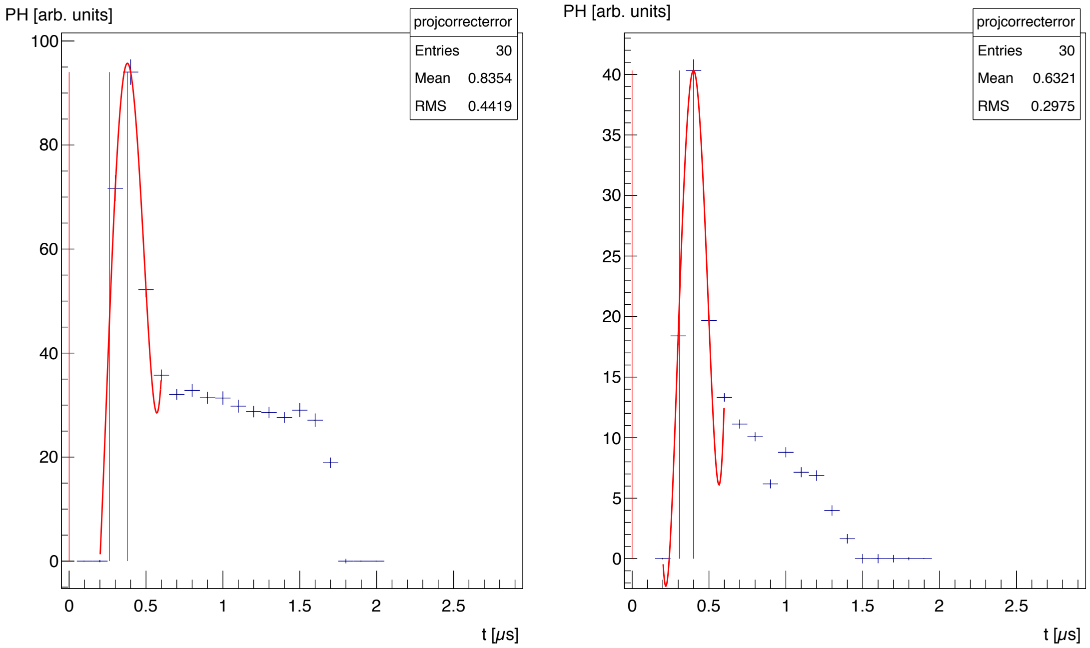

Figure 6.10: Fitted pulse height spectra from the debug output of `determineCoeff.C` for runs 3095 (left) and 3093 (right). Spectra are indicated by blue crosses, the red line is the polynomial fit. The times t_0, t_A and t_D are indicated by red vertical lines. The unit of the x-axis is μs, the pulse height on the y-axis is given in arbitrary units.

It can be seen that the fit was not successful. At first, it was suspected that this is due to large fluctuations of the pulse height in the plateau after the peak of the signal. Such fluctuations can be seen for the spectrum of run 3093, but are not present for run 3095. As both runs show the same problem these fluctuations cannot be the cause. It is counterintuitive that calibration groups with high statistics tend to be set to the default value while groups with fewer entries, for example those in stack 0, get reasonable values. Usually, a fit should rather fail when the pulse height spectra contain few entries causing the spectra to be less smooth.

The fact that the determination of the drift velocity failed was found at the end of the analysis. As the gain results were taken from the pass1 reconstructions, which use the drift velocity OCDB created in the second calibration step, all previous results are affected by this. In [Alb10] it has been found that incorrect values for the drift velocity have an influence on the determined relative gain. The actual drift velocity in $\mathrm{Ar/CO_2}$ is about 2 cm/μs. This results in an inferior determination of tracklets with the default value compared to the actual one. Fortunately this shifts all relative gain values to the same degree. The values differ from the actual ones while the shapes of the gain profiles and differences between calibration groups are conserved. Therefore, the wrong drift velocity could be one of the reasons for the systematically low relative gain factors found in the calibration.

7 Summary and Conclusion

The objective of this thesis was a gas gain calibration of an ALICE Transition Radiation Detector supermodule. This has been performed using the AliRoot Software Framework and macros which have been used in previous works.

A long hiatus from calibration activities necessitated major changes in the macros and the used AliRoot version, as well as a recomissioning of the cosmic trigger. Regarding the trigger hardware, the threshold voltages for the scintillation counters of the cosmic trigger have been optimized in order to obtain a homogenous event distribution over the whole supermodule. Further work is needed in order to restore the trigger rates that could be achieved in earlier analyses, as these have decreased over time.
Concerning the software, the existing framework has been brought to a state where a reconstruction and calibration can be performed again. All macros, scripts, OCDB files and calibration objects needed for the process have been cleaned up and collected in a folder on the local computer cluster. This work can be used as an updated manual on carrying out the reconstruction and calibration procedure with detailed descriptions of the algorithms being available in [Bai09] and the previous version in [Gat10].

Using the updated software, the calibration of the relative gain factors has been carried out. The determined gain factors are lower than expected in most cases. Comparisons with previous calibration results hinted at a systematic effect of the calibration software, as the shape of the gain profile was compatible with earlier observations. Two possible explanations have been found for this:
First, the chamber gain reference value, which is stored in the default OCDB used during calibration, is a value for the energy loss of particles created in proton-proton collisions at the LHC. This value might be higher than the one for cosmic events resulting in an overall lower relative gain.
Second, the algorithm for the determination of the drift velocity from the pulse height spectra does currently not produce reliable results in calibration groups with high tracklet counts. Thus, most groups are set to a drift velocity default value which does not match the actual drift velocity. This results in an overall shift of the gain factors, as the determination of tracklets is less precise during reconstruction.

Furthermore, the deactivation of filters on tracklet quality in the tracking procedure as a means of increasing statistics for calibration has been explored. Calibrations have been carried out for different sets of filters applied in the reconstruction of a given number of files from the same run. It has been found that switching off one of the filters boosts the total count of tracklets by about 27% without a significant change in the calibration output.

The reliability of the reconstruction has been discussed by examining the relative gain as a function of anode voltage. An expected exponential dependence has been found. Nonetheless, this dependency deviated from previous measurements. The question whether this is caused by the uncalibrated drift velocities, the overall low relative gain or problems with the calibration software requires further investigation.

This leads to the conclusion that the reactivation of the calibration software framework was successful. A gain calibration of the entire supermodule could be carried out making the work performed in this thesis a stepping stone for subsequent calibration activities. However, the reason for the incorrect functioning of the drift velocity algorithm, as well as the incompatibility of the gain results at different anode voltages with other works need further investigation.

8 Appendix

8.1 List of Abbreviations

ADC	Analog to Digital Converter
ALICE	A Large Ion Collider Experiment
ATLAS	A Torodial LHC Apparatus
CERN	Conseil Européen pour la Recherche Nucléaire (European Organization for Nuclear Research)
CMS	Compact Muon Solenoid
CT	Cosmic Trigger
CTP	Central Trigger Processor
DAQ	Data Acqusition-System
DCS Board	Detector Control System Board
EMCAL	Electromagnetic Calorimeter
FEE	Front-End Electronics
FERO	Front-End Readout Electronics
GSI	Gesellschaft für Schwerionenforschung (Association for Heavy-Ion Research)
GTU	Global Trigger Unit
ITS	Inner Tracking System
HLT	High Level Trigger
HMPID	High Momentum Particle Identification Detector
LHC	Large Hadron Collider
LHCb	Large Hadron Collider beauty
LHCf	Large Hadron Collider forward
MCM	Multi Chip Module
MIMD CPU	Multiple Instruction Multiple Data Central Processing Units

OCDB	Offline Conditions Database
ORI	Optical Readout Interface
PASA	Preamplifier and Shaper
PHOS	Photon Spectrometer
PID	Particle Identification
PRF	Pad Response Function
QCD	Quantum Chromo-Dynamics
QED	Quantum Electro-Dynamics
QGP	Quark Gluon Plasma
ROC	Read Out Chamber
SM	Supermodule
TOF	Time of Flight
TOTEM	Total Elastic and Diffractive Cross Section Measurement
TPC	Time Projection Chamber
TR	Transition Radiation
TRAP	Tracklet Processor
TRD	Transition Radiation Detector
TPP	Tracklet Preprocessor

8.2 ALICE Coordinate Systems

Several different coordinate systems are present in ALICE including the global ALICE coordinate system, the local tracking coordinate system of the TRD supermodules, and the local alignment coordinate systems of the TRD.
The global ALICE coordinate system is a right-handed Cartesian coordinate system displayed in figure 8.1. The z-axis points in beam direction opposite to the muon arm, the y-axis points upwards and the x-axis points to the LHC center. Positions can also be given in spherical coordinates z, r, and θ or ϕ. Here r is the radius and θ the angle of counterclockwise rotation of r around the z-axis. A rotation around the x-axis is described by ϕ. The origin is in both cases defined by the intersection point of the TPC central membrane and the z-axis [BC03].

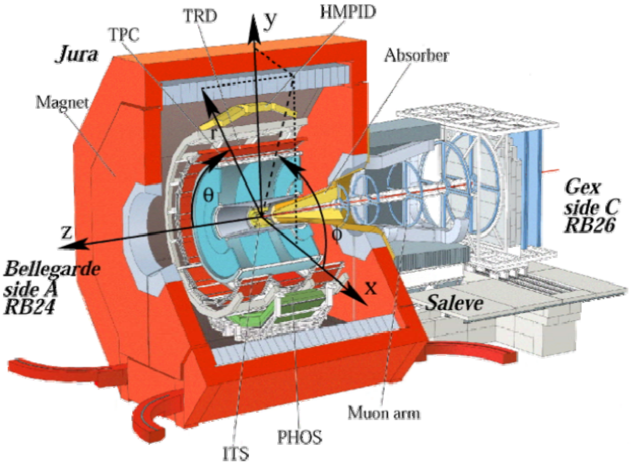

Figure 8.1: Cross section of the ALICE detector with the Global Coordinate System in Cartesian and Spherical Coordinates [BC03].

In addition to the global coordinate system a local coordinate system for the individual TRD supermodules was introduced. It is a right handed Cartesian coordinate system (x,y,z) sharing its origin with the global ALICE coordinate system. The z-axis is the same in both coordinate systems, while x rises with increasing layer number. As shown in figure 8.2 the local tracking coordinate system of each supermodule can be converted into global tracking coordinates by a rotation of the x-axis around the z-axis [Sic09].

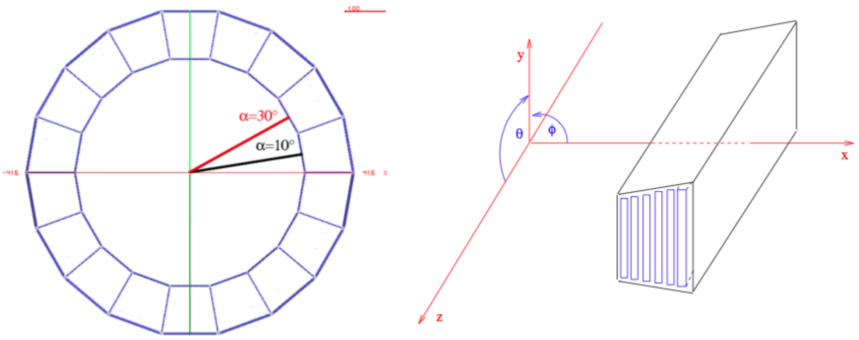

Figure 8.2: Schematic view of the installation slots of the 18 TRD supermodules and the conversion of local tracking coordinates to global ALICE coordinates [Sic09].

In local alignment coordinates r, z and ϕ_r each chamber gets its own coordinate system with the chamber midpoint as its origin. The r axis corresponds to the x-axis of the local tracking coordinate system and points in the same direction. The ϕ_r-axis is congruent to the y-axis, but points in the opposite direction [Gat10].

8.3 List of Supermodule Runs

Run	FEE	U_{Drift} [V]	U_{Anode} [V]	Remarks
3049	311	1500	1500	5 layers
3053	311	1500	1500	5 layers
3055	311	1500	1500	5 layers, high gain layer 4
3062	311	1500	1500	High gain layer 5
3063	311	1500	1500	High gain layer 5
3066	311	1500	1500	High gain layer 5
3067	313	1500	1500	Low voltage trip
3068	313	1500	1500	Low voltage trip
3071	311	1500	1500	
3072	311	1500	1500	Investigation of reconstruction filters
3075	313	1500	1500	Relative gain and tracklet thresholds
3077	311	1500	1500	
3079	311	1500	1500	
3080	311	1500	1500	
3081	311	1500	1500	
3082	311	1500	1500	Used for $g(U)$
3083	311	1400	1500	23 h, $v_{\text{drift}}(U)$
3084	311	1300	1500	24 h, $v_{\text{drift}}(U)$
3085	311	1095	1500	47 h, $v_{\text{drift}}(U)$
3086	311	1200	1500	23 h, $v_{\text{drift}}(U)$
3093	311	1500	1480	6 h; 130 Hz, $g(U)$
3094	311	1500	1400	1 h; 50 Hz, $g(U)$
3095	311	1500	1460	11 h; 100 Hz, $g(U)$
3096	311	1500	1510	1 h; 150 Hz; U_{Anode} unstable

Table 8.1: Run numbers, FEE configuration, and drift and anode voltages for the recorded runs. All runs used a combination of bottom and coincidence trigger mode together with the GTU cosmic trigger.

8.4 Gain Calibration Results

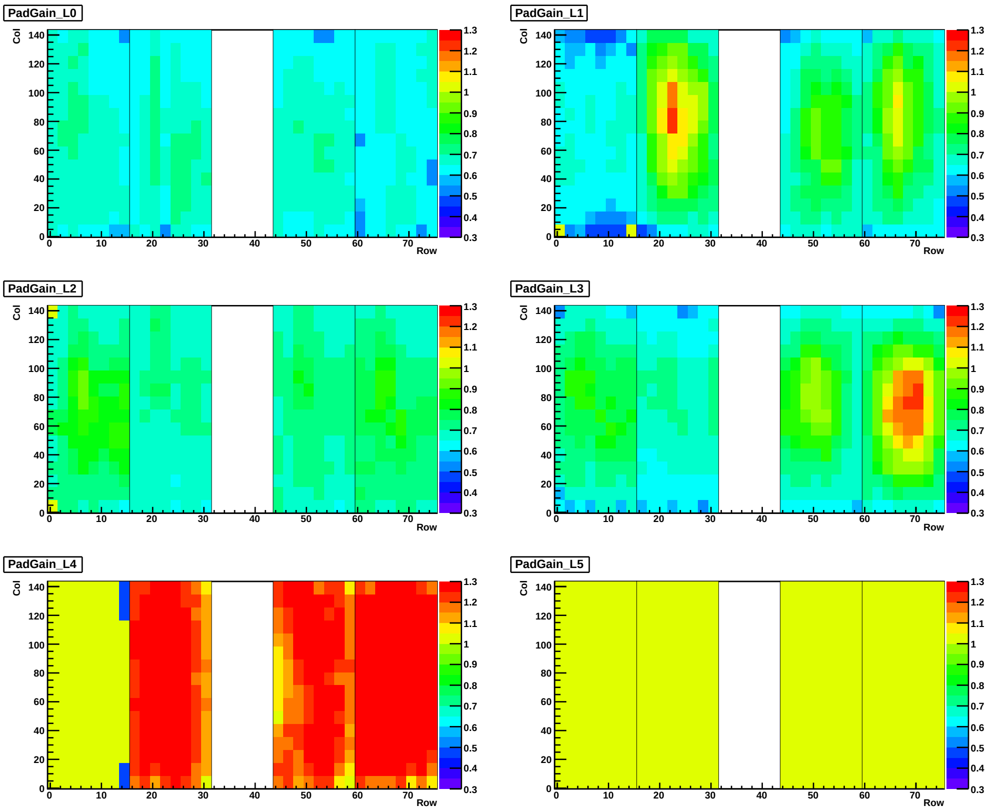

Figure 8.3: Relative gain factors from run 3055 at (3,4) granularity.

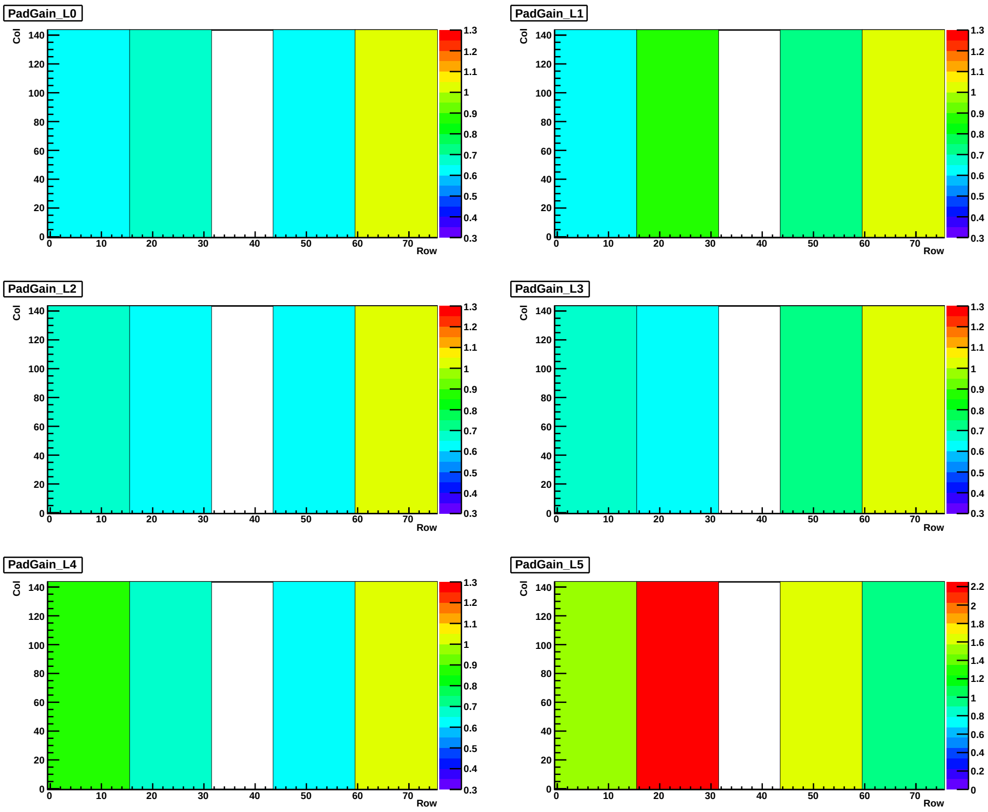

Figure 8.4: Relative gain factors from run 3062 at (0,0) granularity.

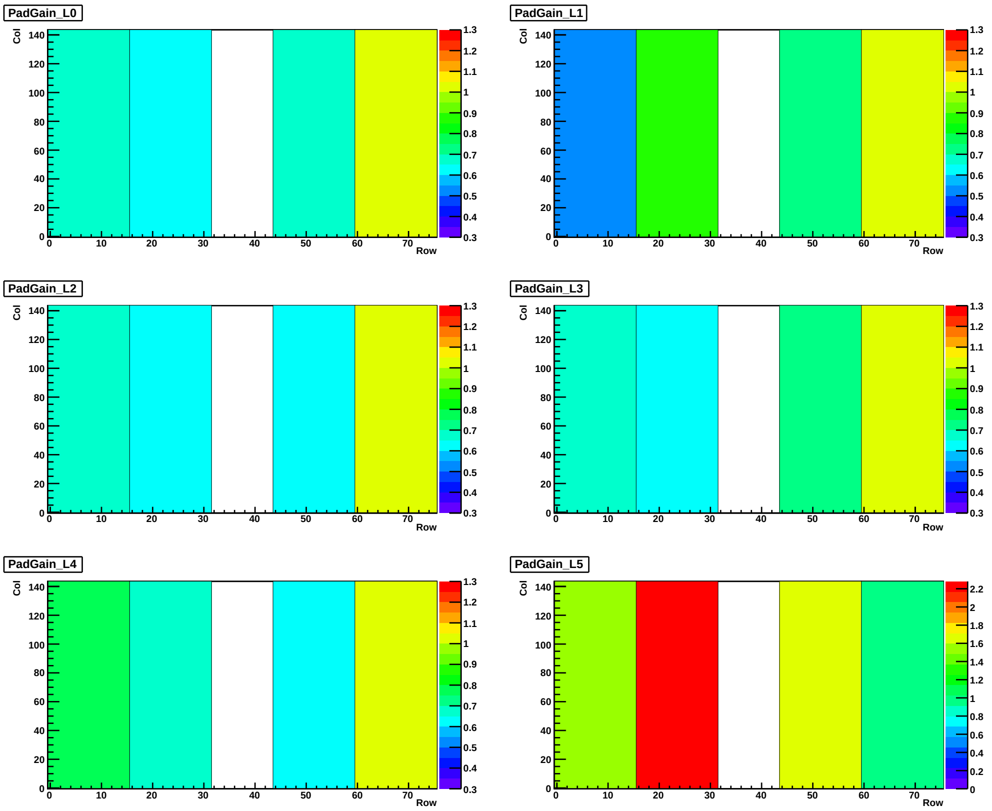

Figure 8.5: Relative gain factors from run 3063 at (0,0) granularity.

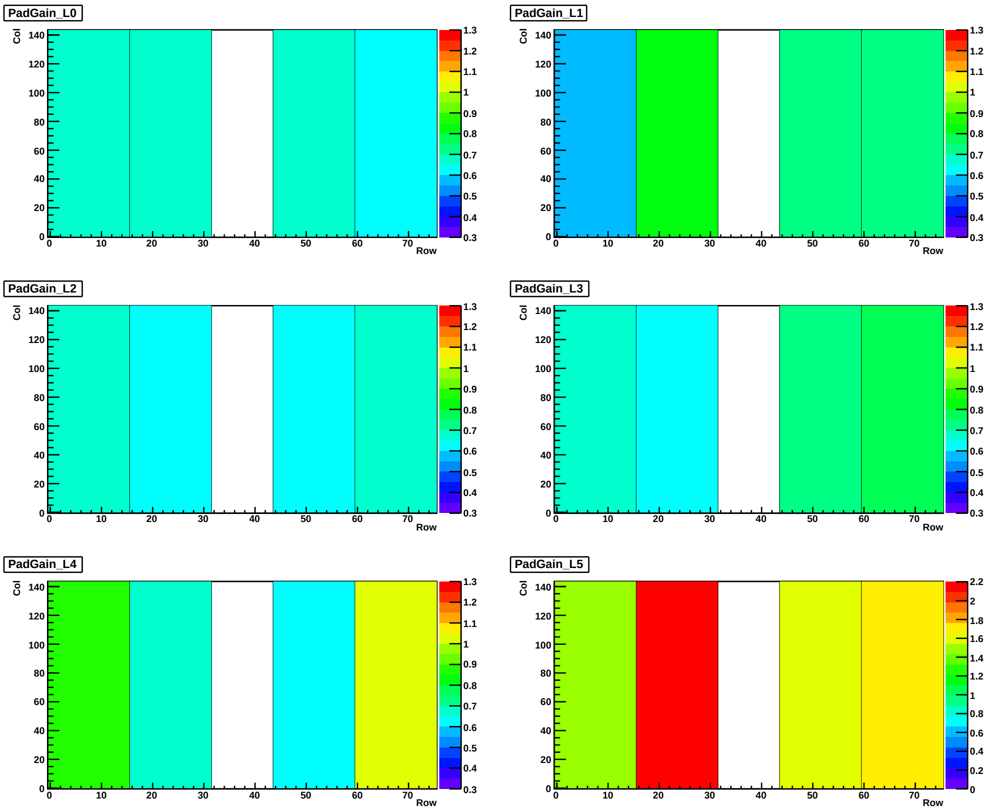

Figure 8.6: Relative gain factors from run 3064 at (0,0) granularity.

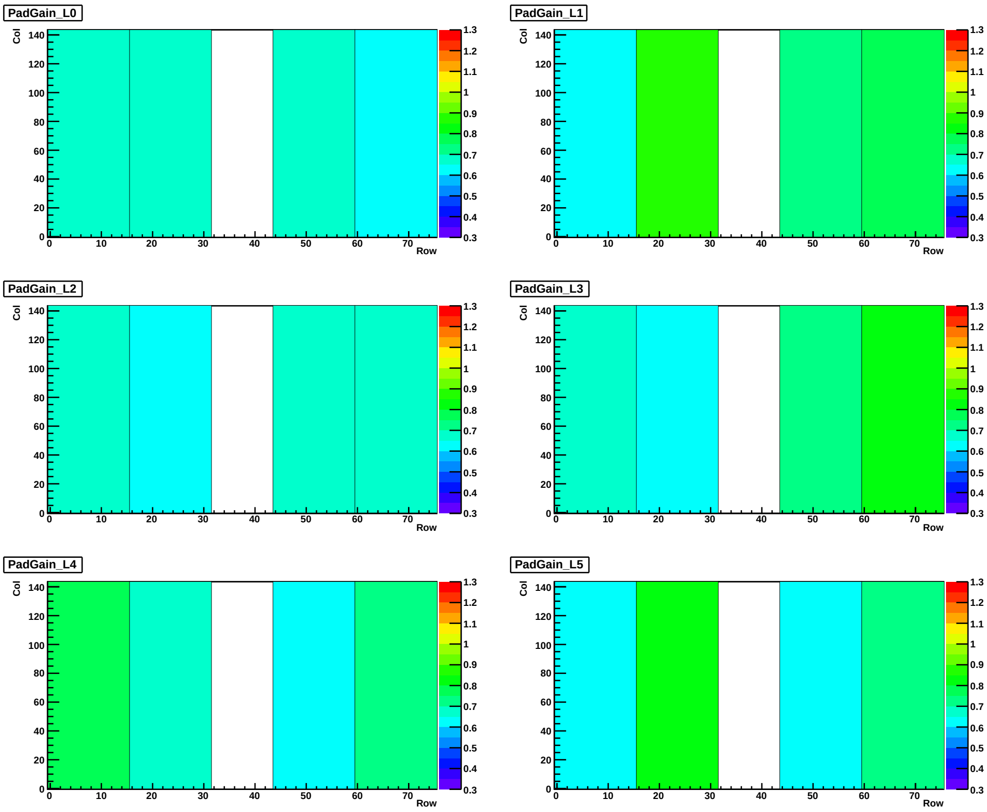

Figure 8.7: Relative gain factors from run 3066 at (0,0) granularity.

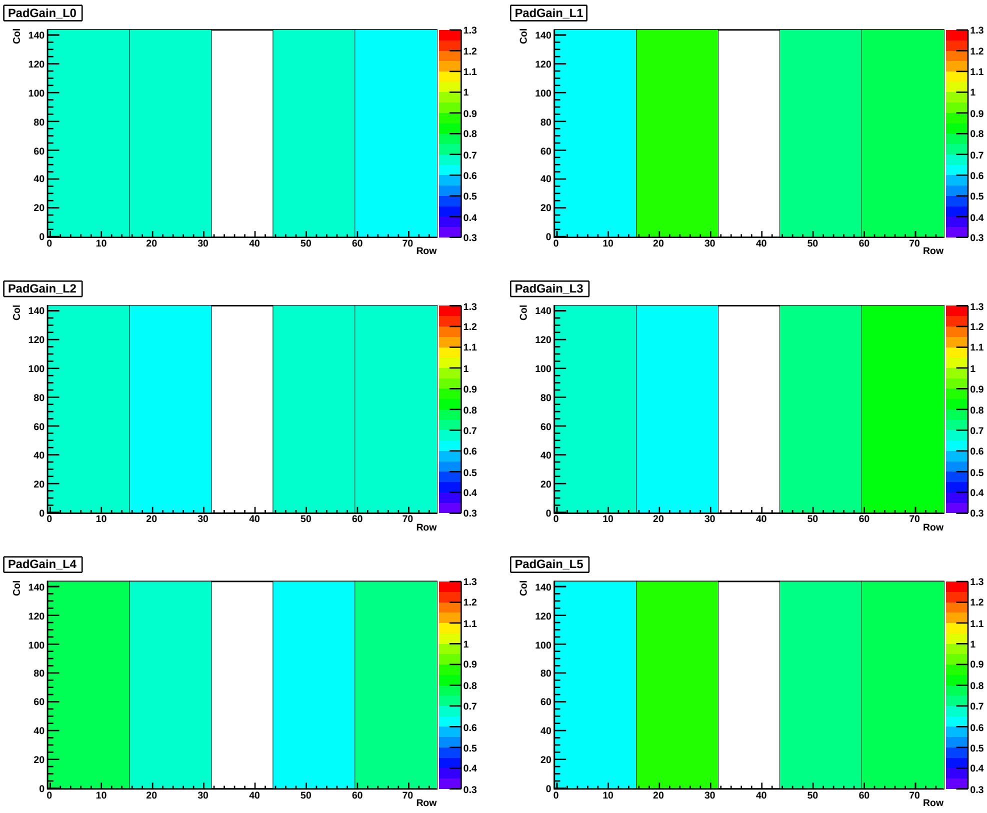

Figure 8.8: Relative gain factors from run 3067 at (0,0) granularity.

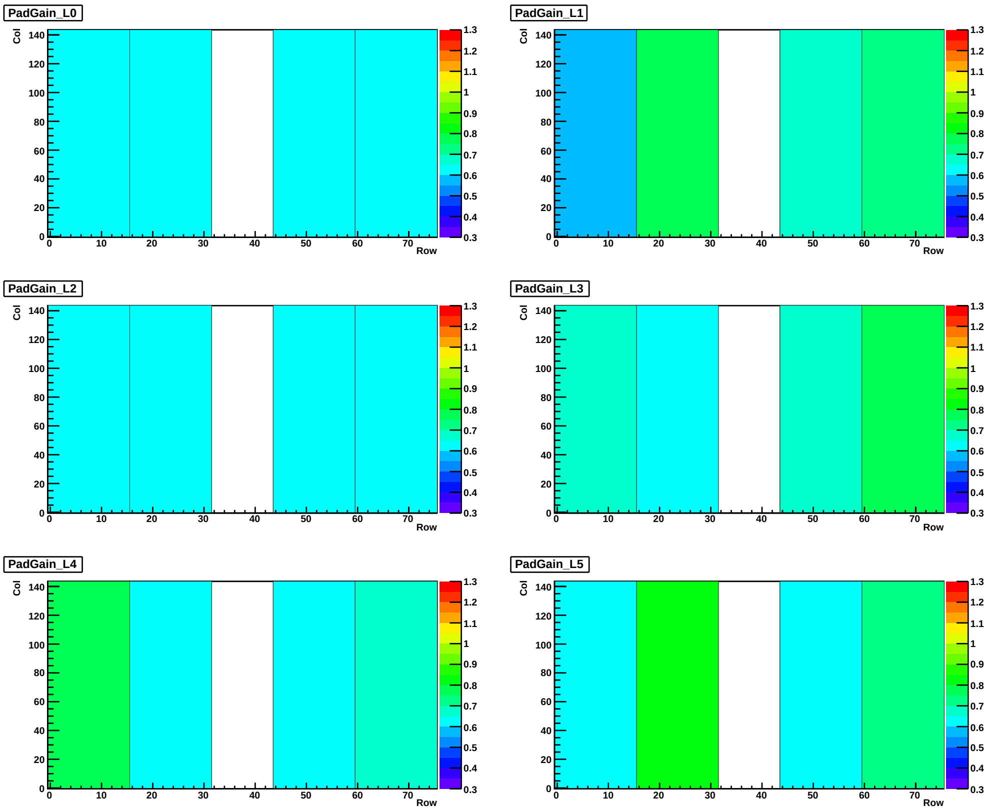

Figure 8.9: Relative gain factors from run 3068 at (0,0) granularity.

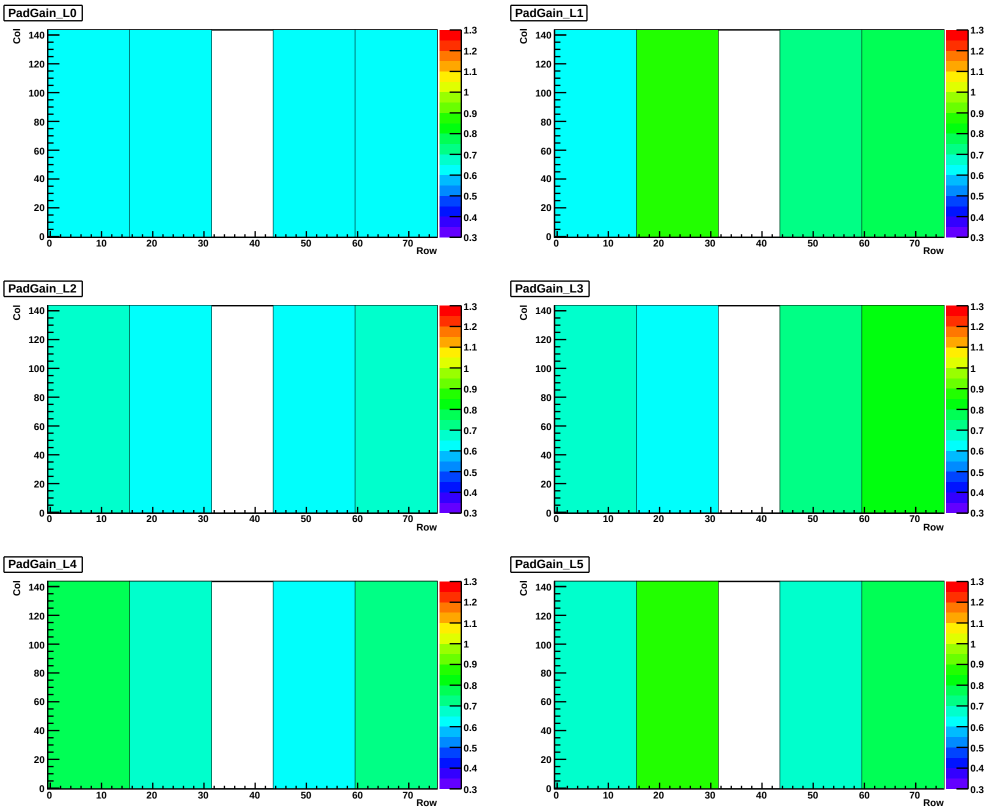

Figure 8.10: Relative gain factors from run 3071 at (0,0) granularity.

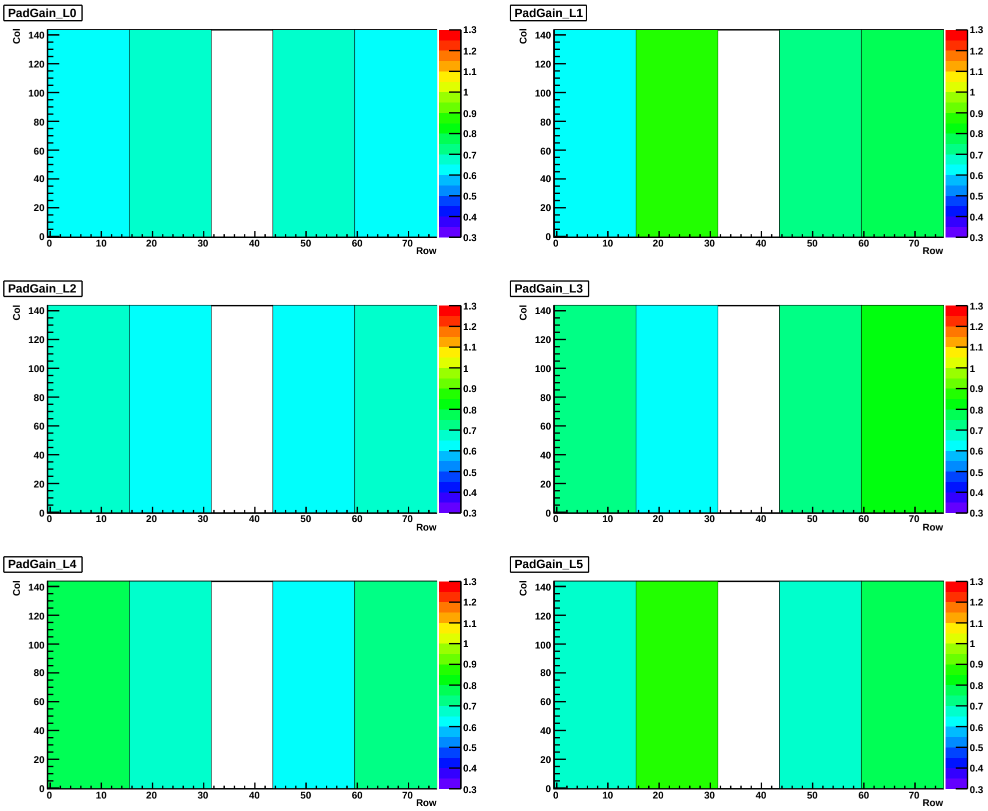

Figure 8.11: Relative gain factors from run 3072 at (0,0) granularity.

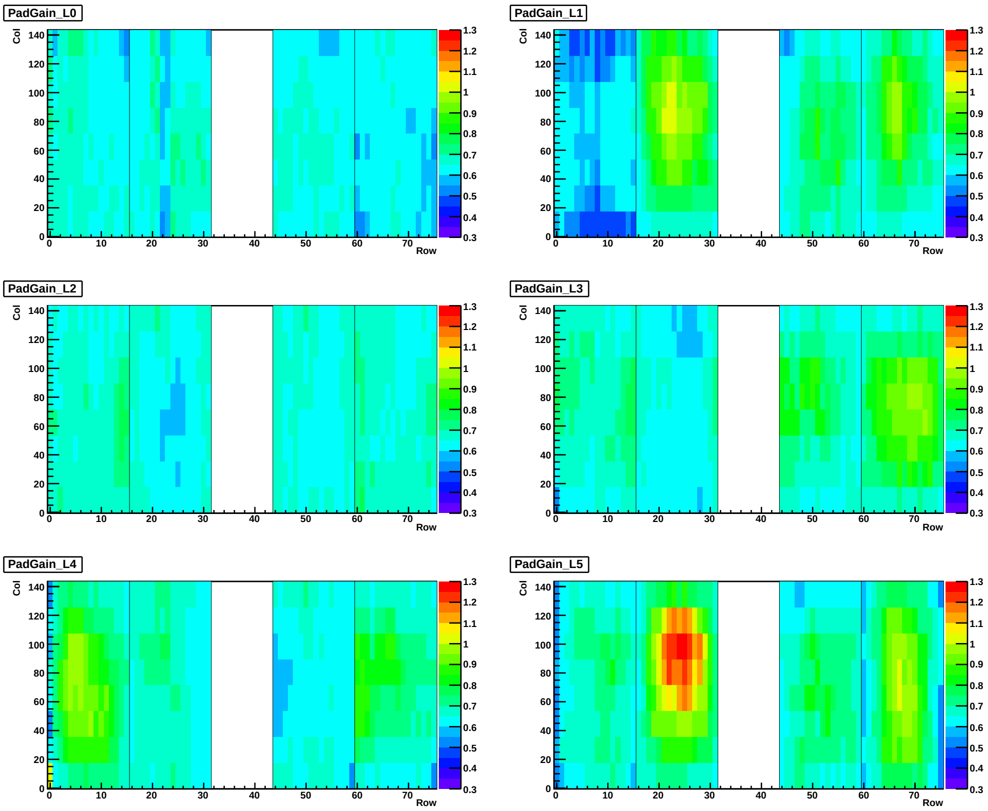

Figure 8.12: Relative gain factors from run 3075 at (4,3) granularity.

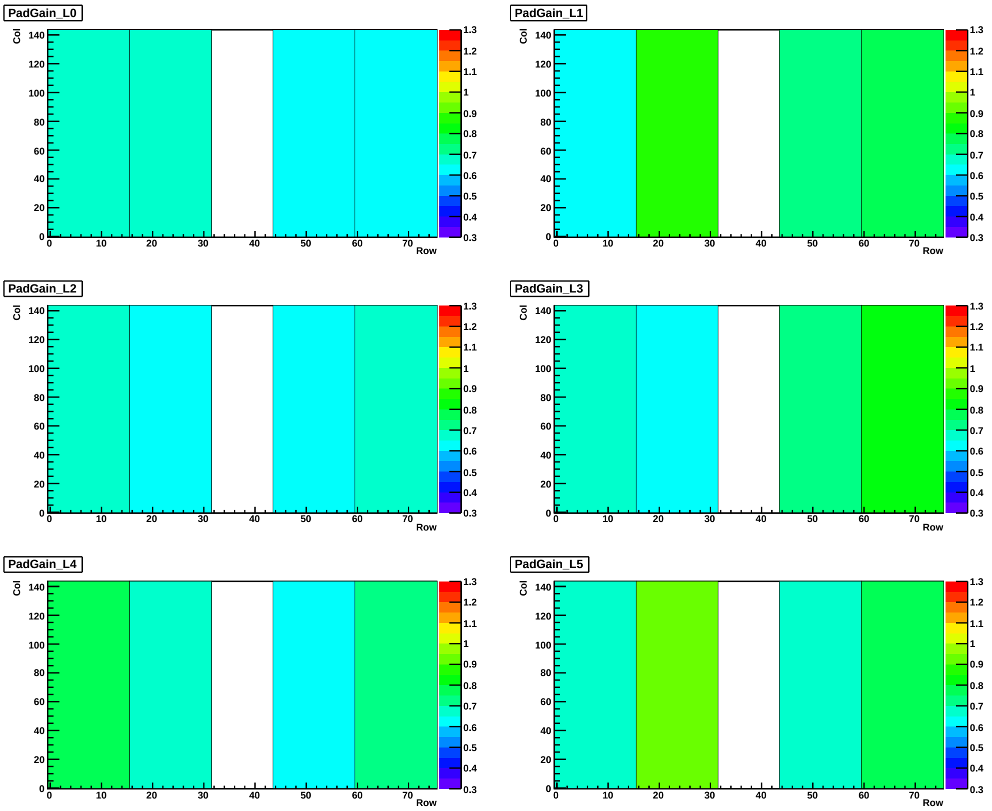

Figure 8.13: Relative gain factors from run 3077 at (0,0) granularity.

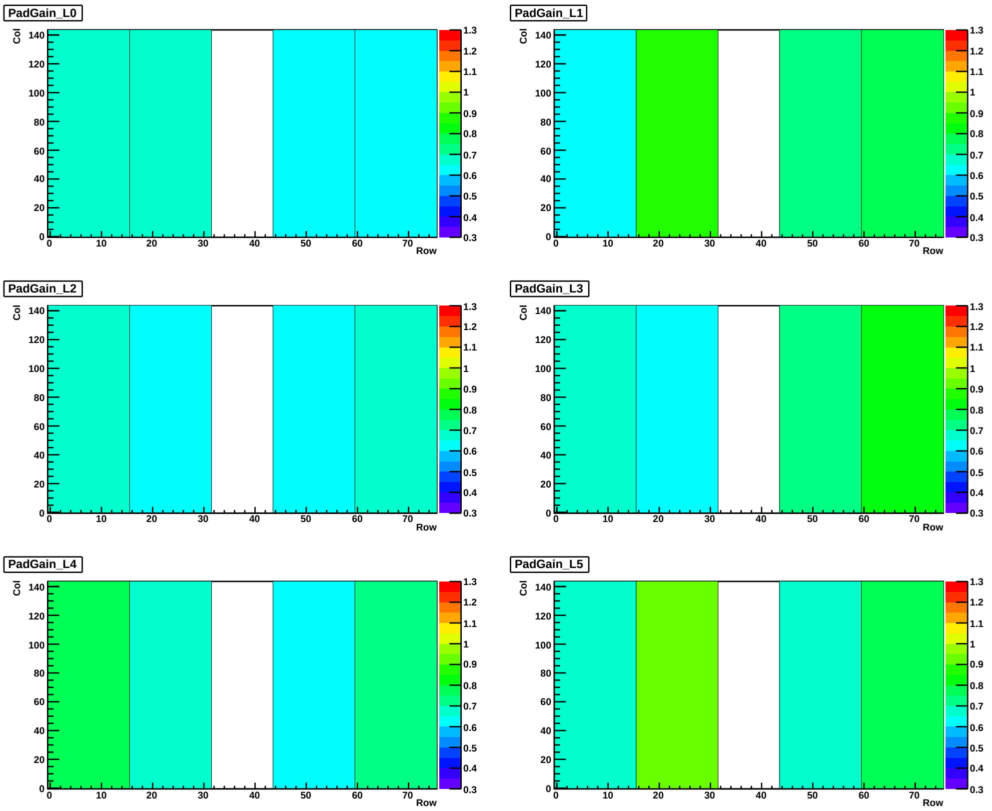

Figure 8.14: Relative gain factors from run 3079 at (0,0) granularity.

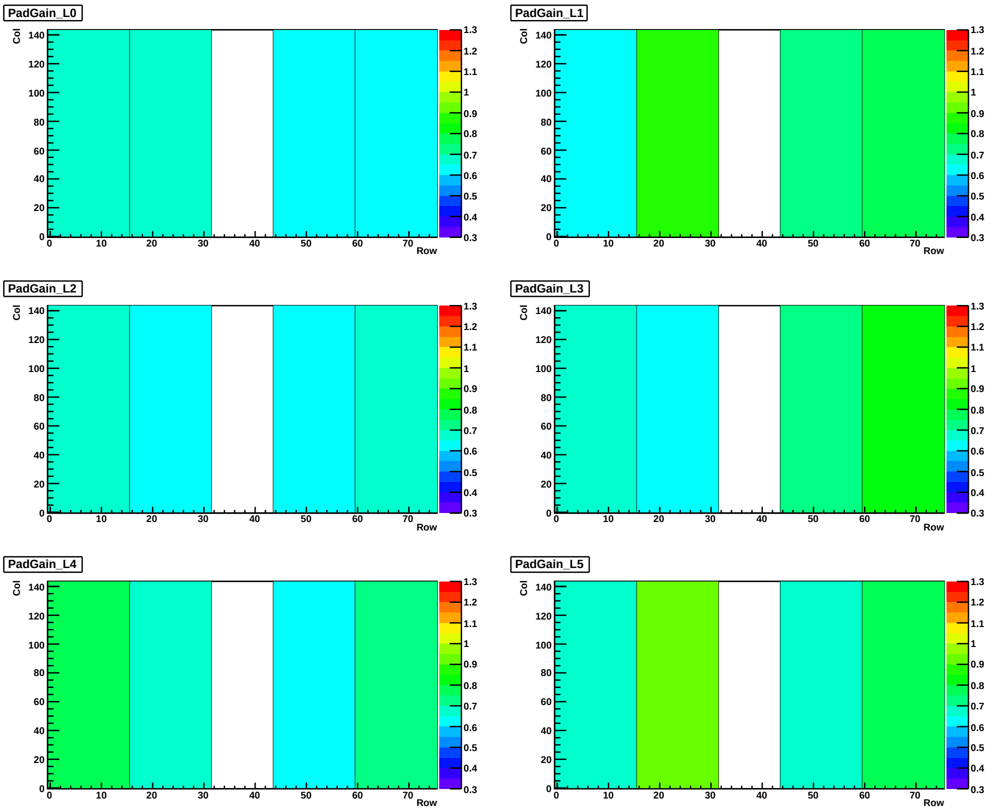

Figure 8.15: Relative gain factors from run 3081 at (0,0) granularity.

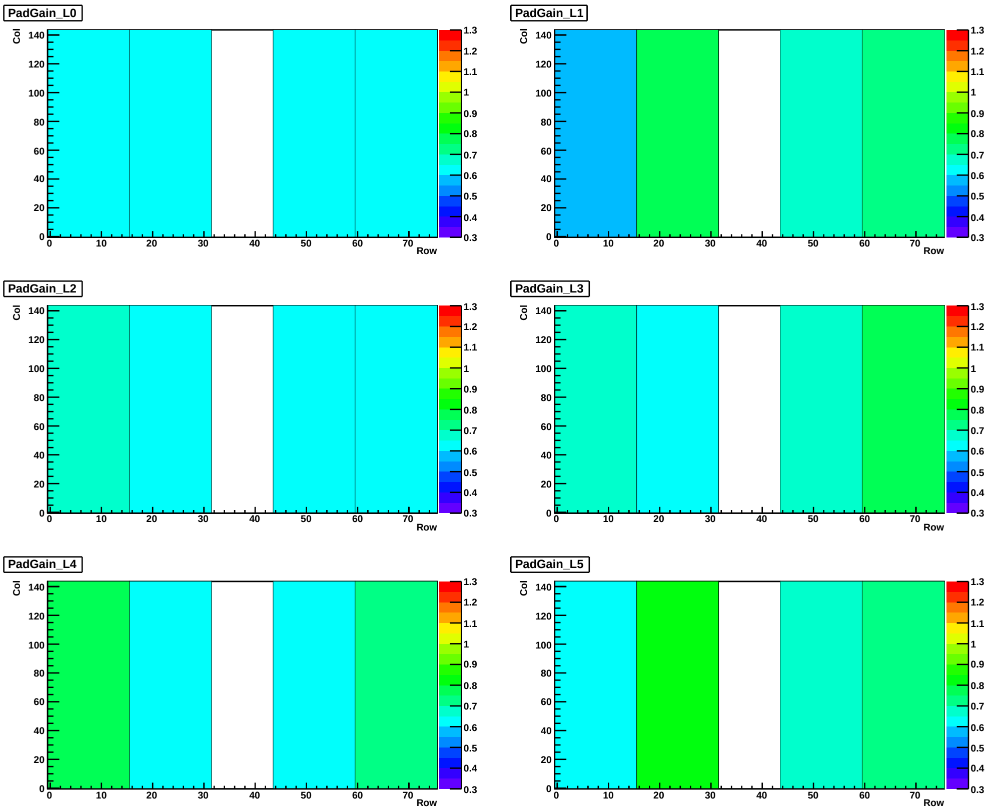

Figure 8.16: Relative gain factors from run 3082 at (0,0) granularity.

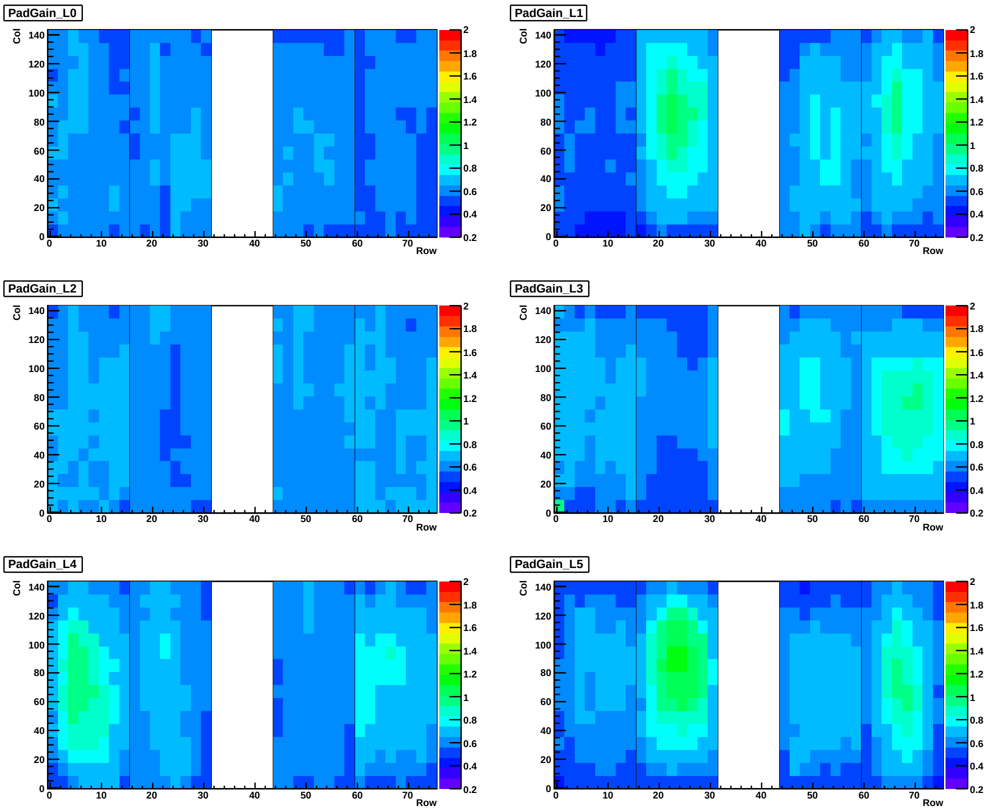

Figure 8.17: Relative gain factors from run 3083 at (3,4) granularity.

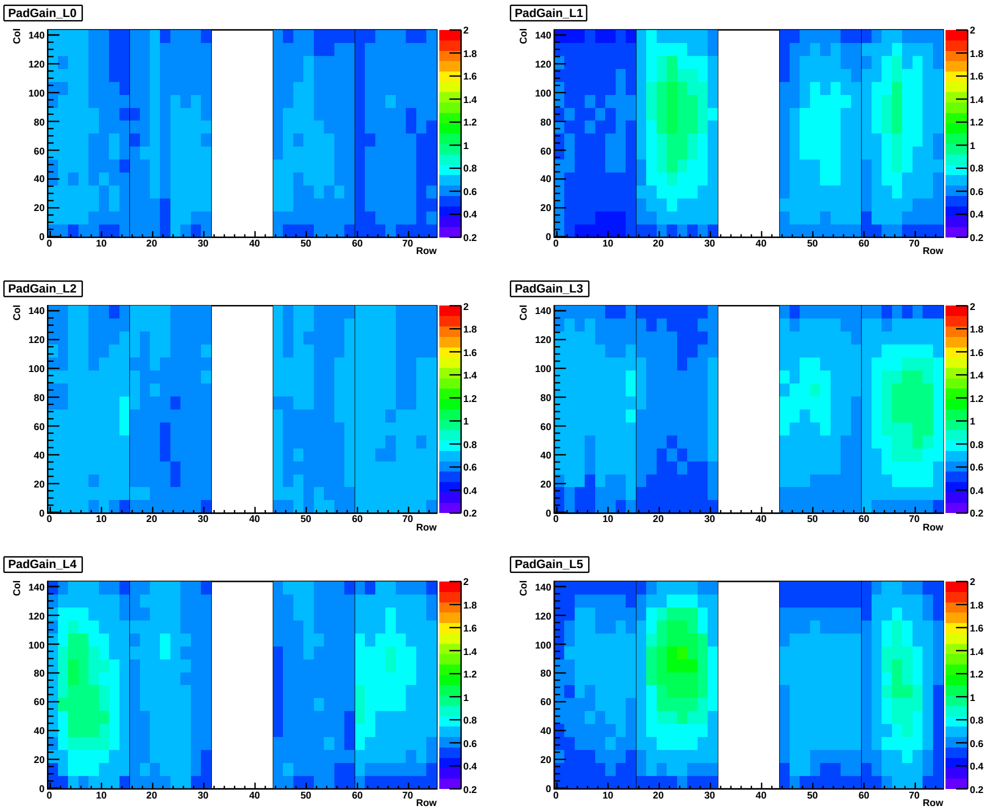

Figure 8.18: Relative gain factors from run 3084 at (3,4) granularity.

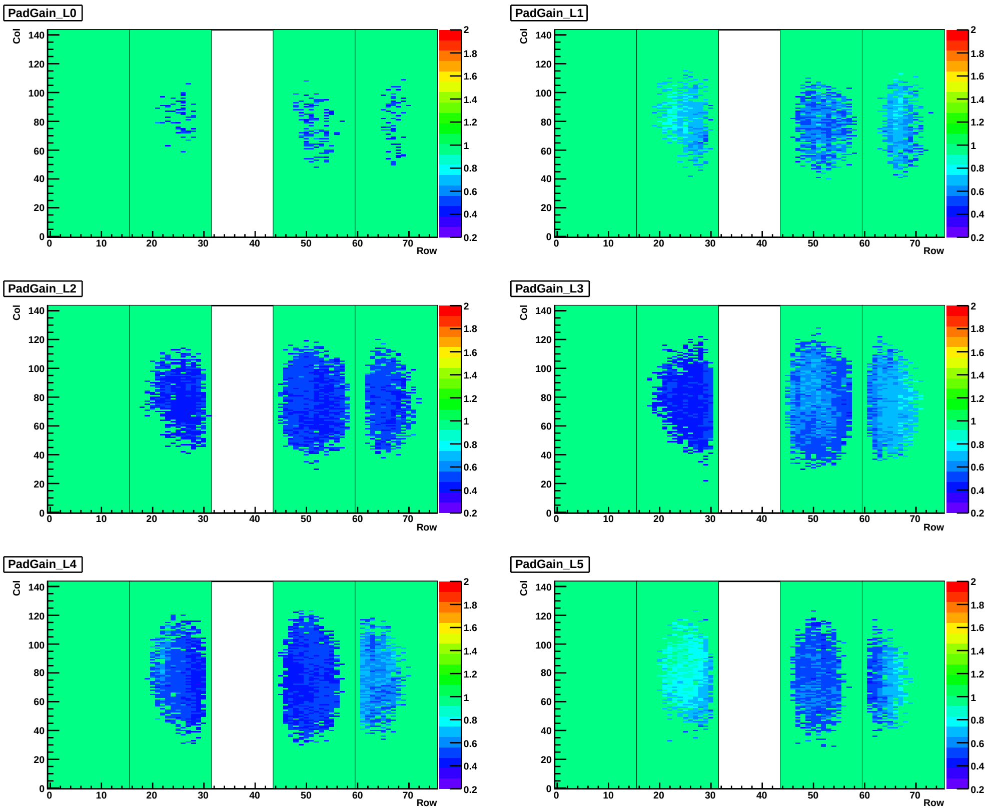

Figure 8.19: Relative gain factors from run 3085 at (4,6) granularity.

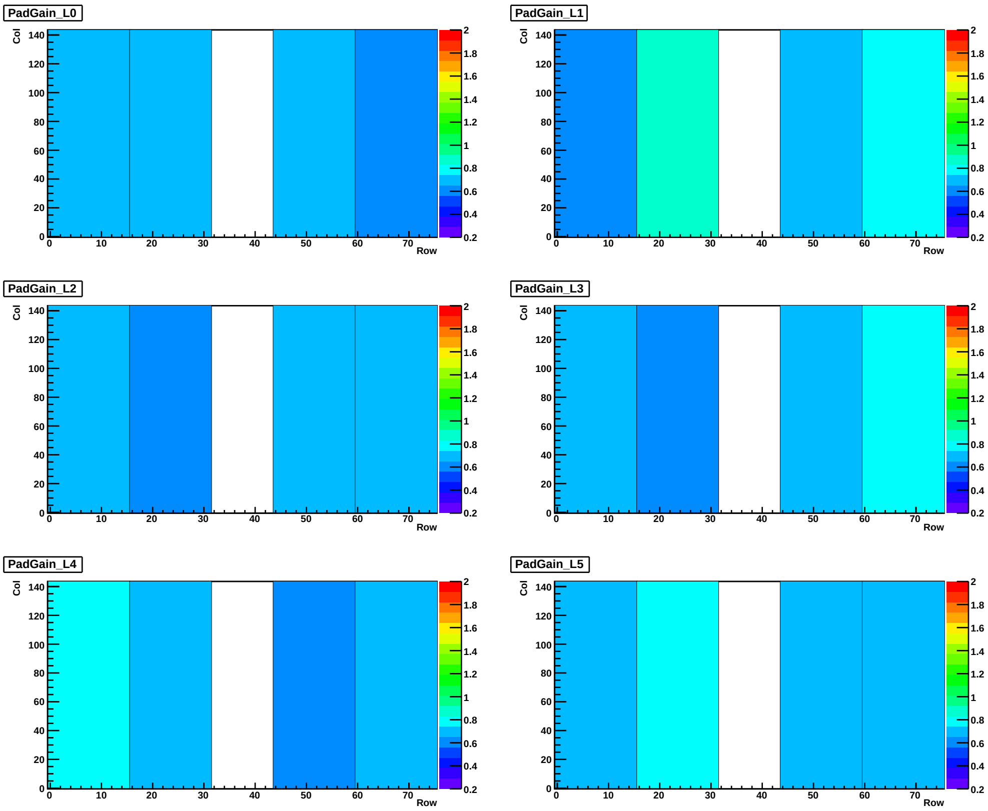

Figure 8.20: Relative gain factors from run 3086 at (0,0) granularity.

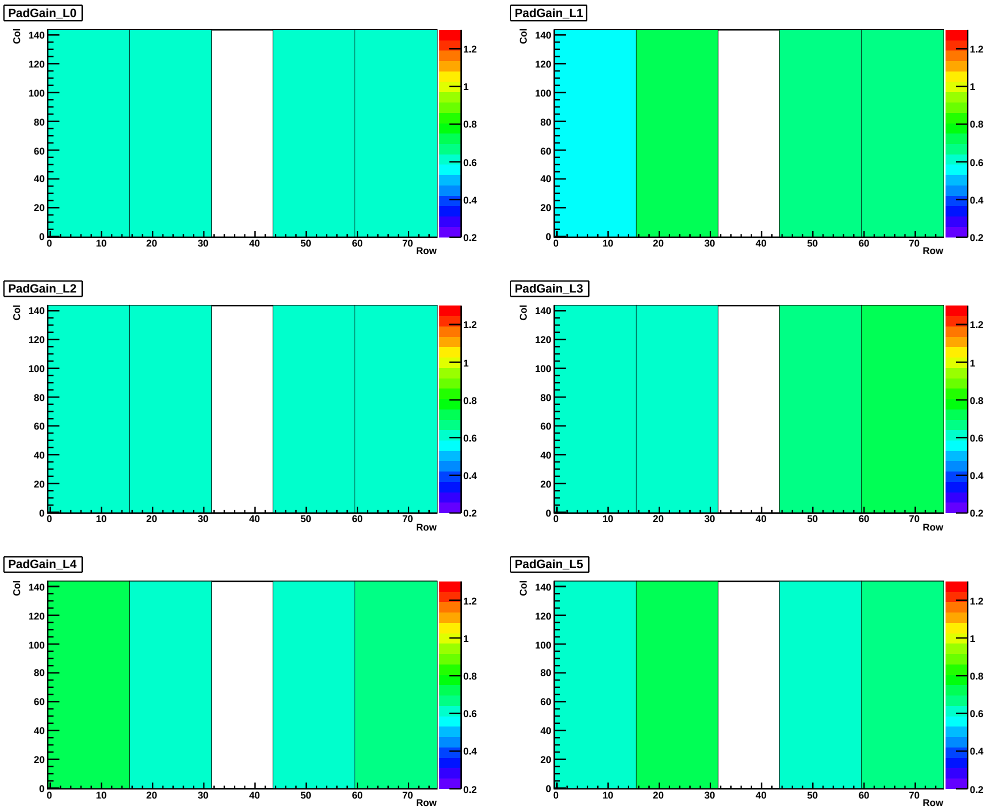

Figure 8.21: Relative gain factors from run 3093 at (0,0) granularity.

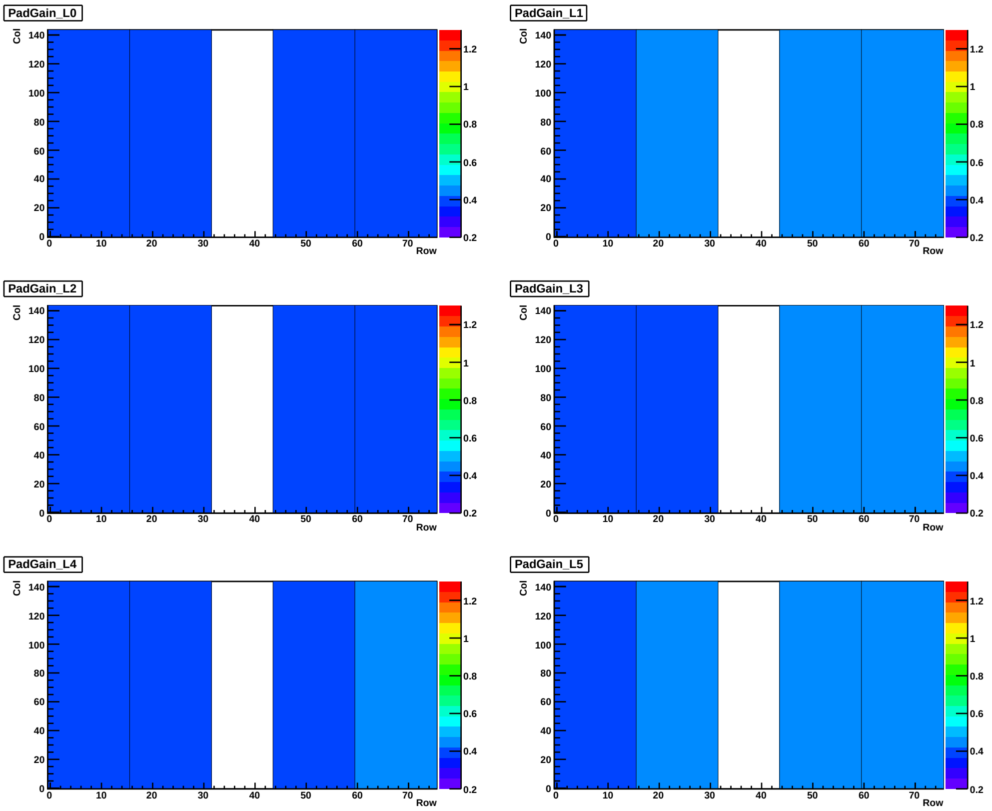

Figure 8.22: Relative gain factors from run 3094 at (0,0) granularity.

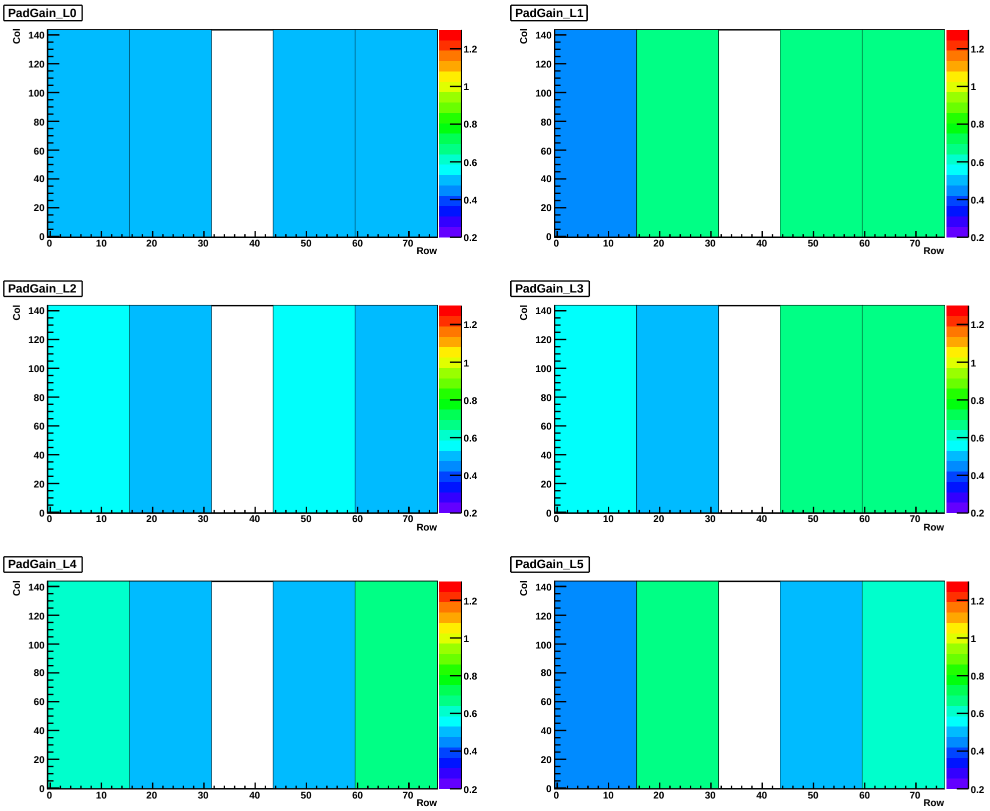

Figure 8.23: Relative gain factors from run 3095 at (0,0) granularity.

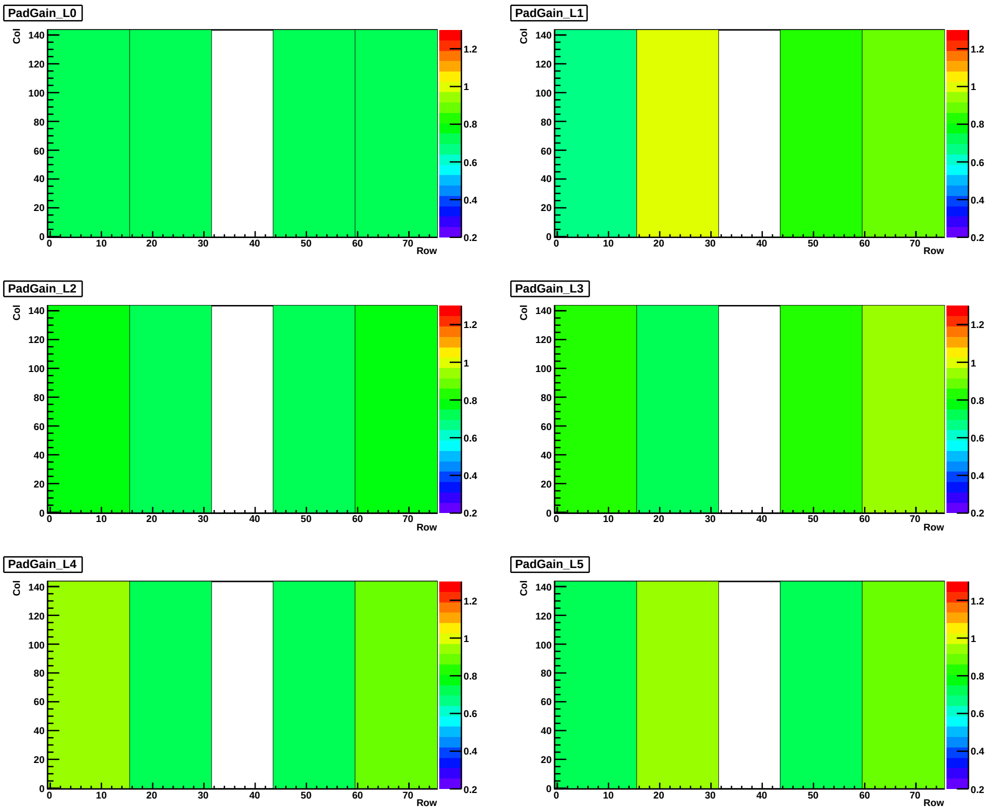

Figure 8.24: Relative gain factors from run 3096 at (0,0) granularity.

8.5 Drift Velocity Results

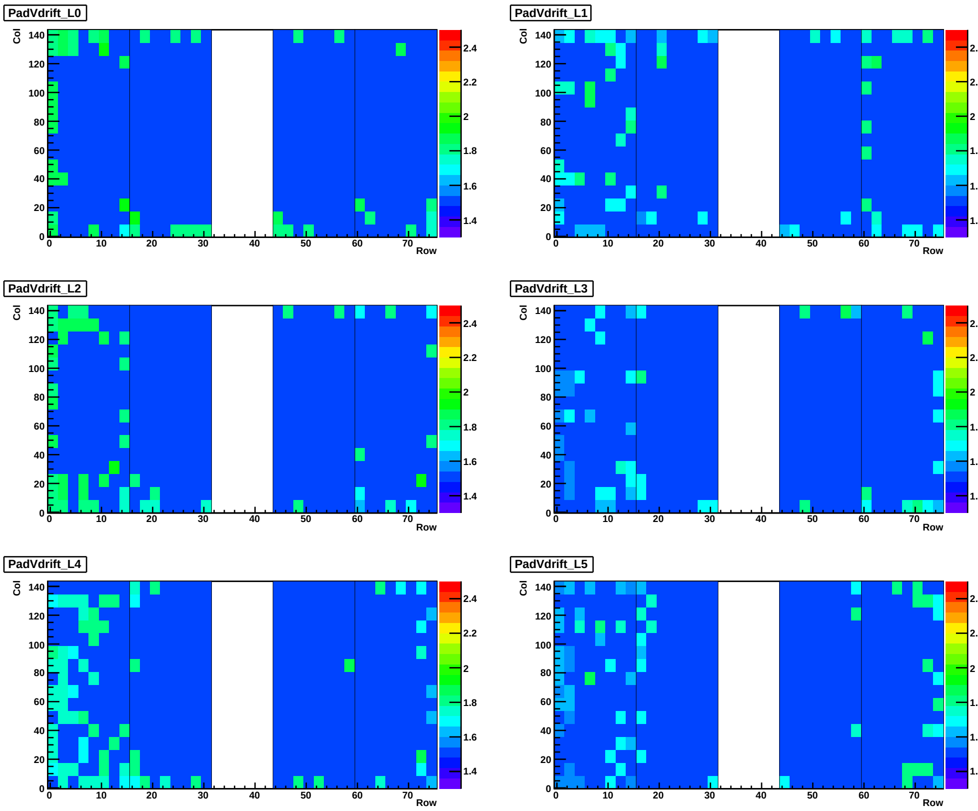

Figure 8.25: Drift velocity from run 3083 at (3,4) granularity.

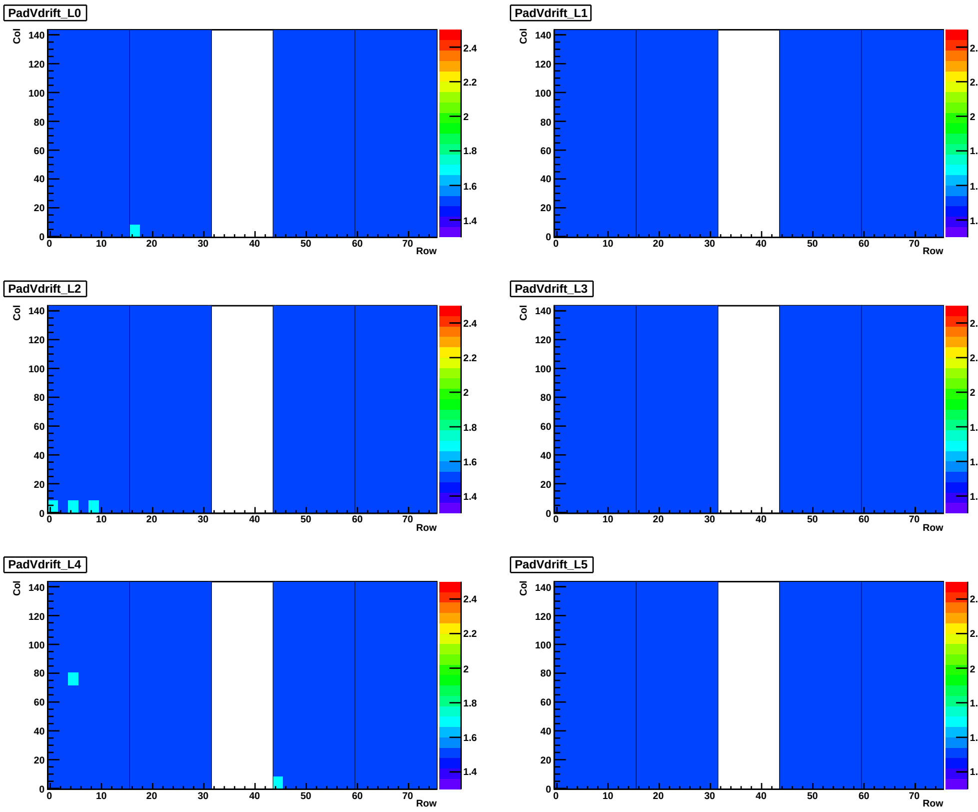

Figure 8.26: Drift velocity from run 3084 at (3,4) granularity.

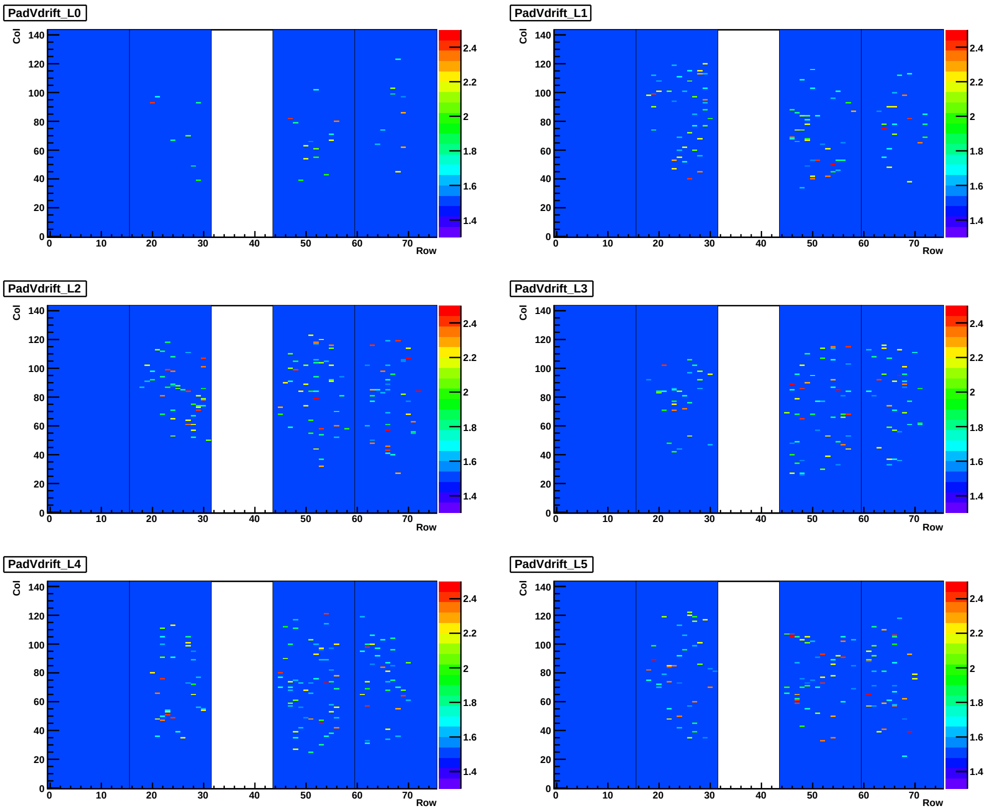

Figure 8.27: Drift velocity from run 3085 at (4,6) granularity.

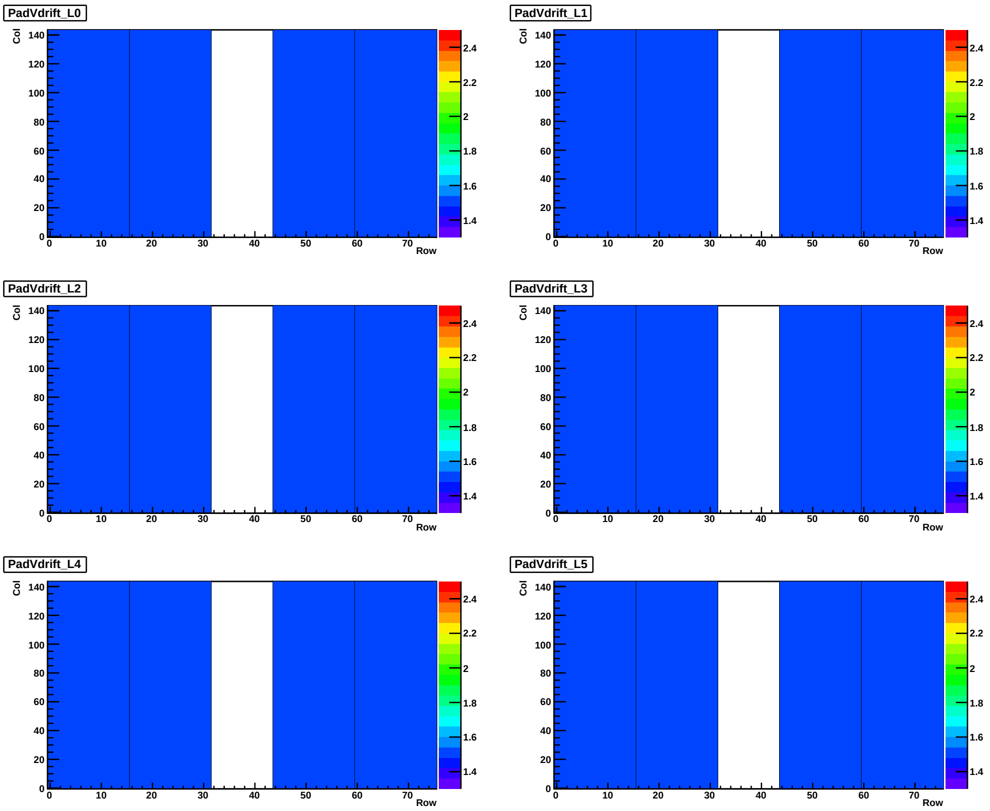

Figure 8.28: Drift velocity from run 3086 at (0,0) granularity.

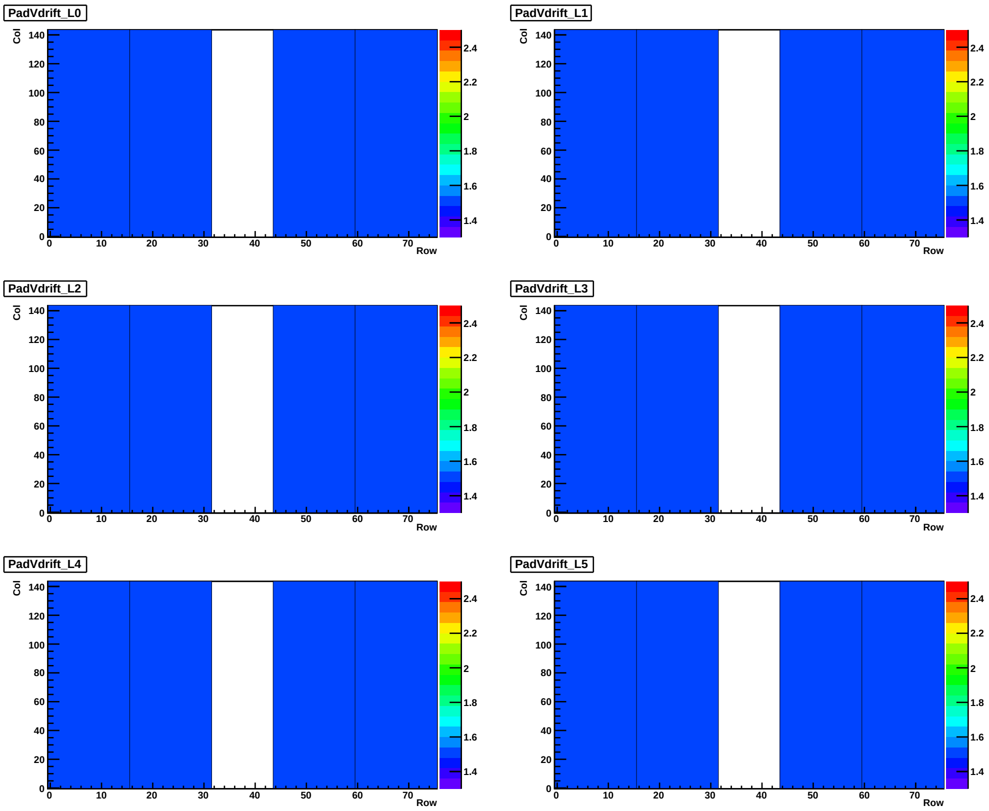

Figure 8.29: Drift velocity from run 3093 at (0,0) granularity.

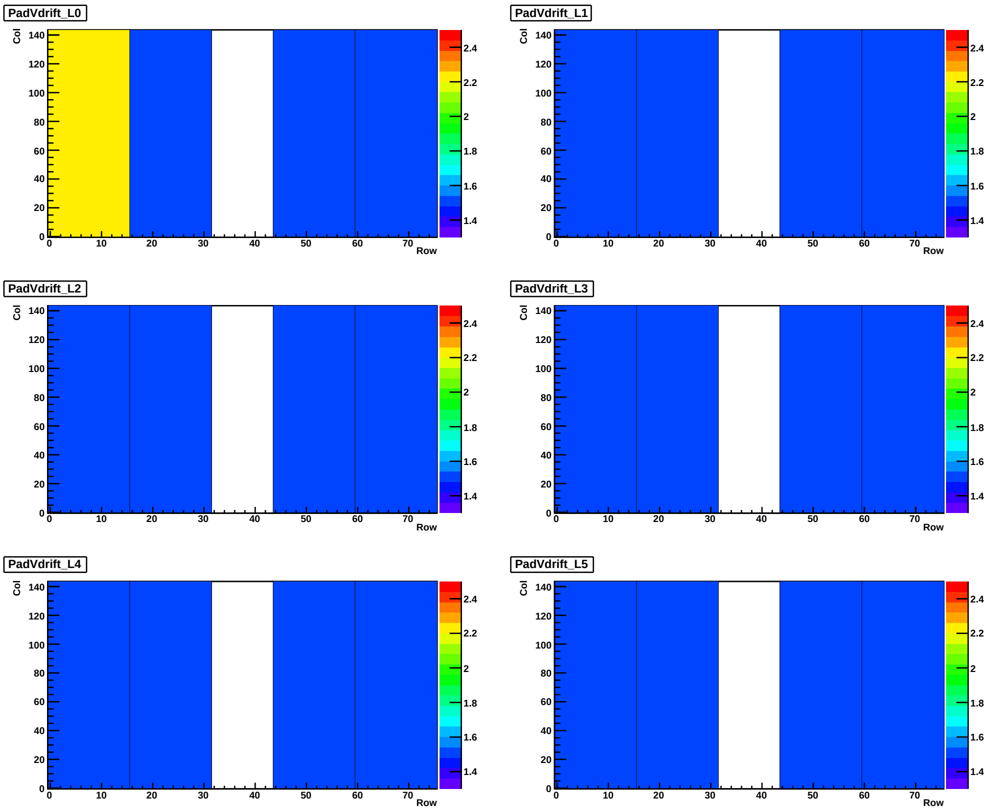

Figure 8.30: Drift velocity from run 3094 at (0,0) granularity.

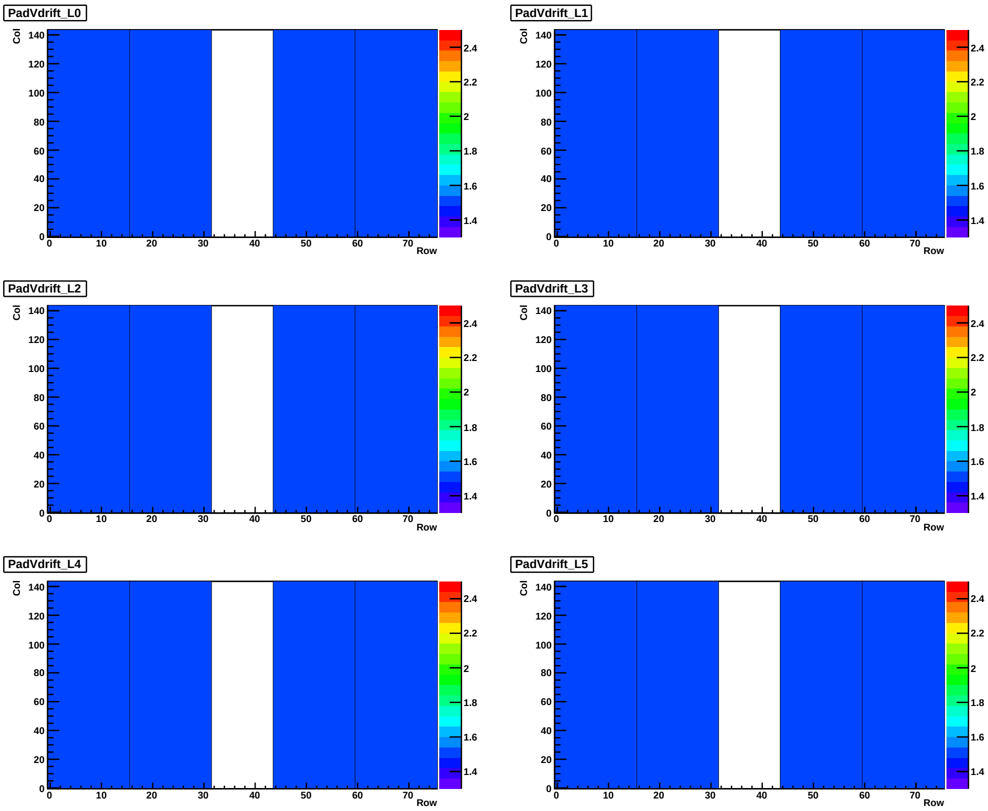

Figure 8.31: Drift velocity from run 3095 at (0,0) granularity.

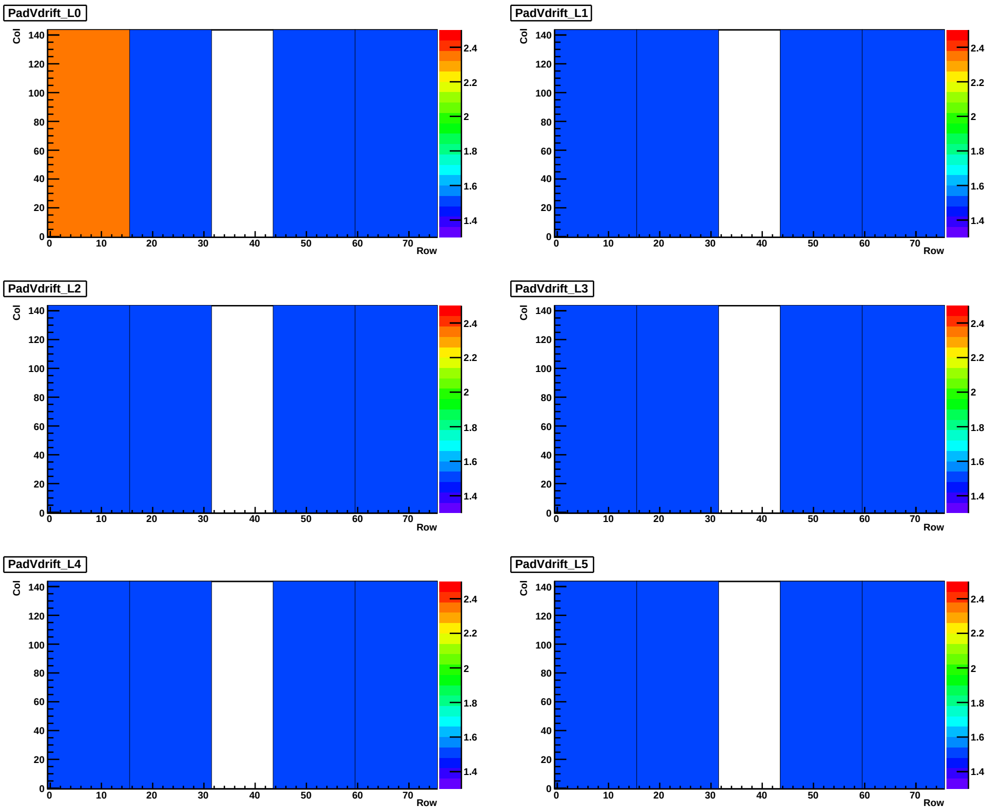

Figure 8.32: Drift velocity from run 3096 at (0,0) granularity.

9 Bibliography

[Alb10] B. Albrecht: *Gain Calibration of ALICE TRD Modules Using Cosmic Ray Data.* Diploma thesis, Westfälische Wilhelms-Universität Münster, 2010.

[ALI01] ALICE Collaboration: *ALICE - Technical Design Report of the Transition Radiation Detector.* 2001.

[ALI04] ALICE Collaboration: *ALICE: Physics Performance Report Vol. I + II.* 2004. Journal of Physics G: Nuclear And Particle Physics, 30, 2004.

[ALI08] ALICE Collaboration: *The ALICE experiment at the CERN LHC.* JINST 3 S08002.

[ALI12] ALICE Collaboration: *J/ψ suppression at forward rapidity in Pb-Pb collisions at $\sqrt{s_{NN}} = 2.76\ TeV$.* arXiv:1202.1383v2.

[AliOff] ALICE Offline Pages. URL: `http://aliweb.cern.ch/Offline/Activities/ConditionDB.html`.

[AliEn] AliEn: *AliEn - ALICE Environment.* URL: `http://alien2.cern.ch/index.php?option=com_content&view=category&layout=blog&id=1&Itemid=5`.

[AliPub] A Large Ion Collider Experiment: *The ALICE Experiment.* CERN, 2014. URL: `http://aliceinfo.cern.ch/Public/en/Chapter2/Chap2Experiment-en.html`.

[And04] A. Andronic et al.: *Drift Velocity and gain in argon- and xenon-based mixtures.* Gesellschaft für Schwerionenforschung, Darmstadt, Germany. Department of Physics, University of Liverpool, UK. 2004.

[Ani11] J. Anielski: *Entwicklng eines Triggersystems zum Testen und Kalibrieren der Supermodule des ALICE-TRD.* Diploma thesis, Westfälische Wilhelms-Universität Münster, 2011.

[AW11] A. Andronic, J. P. Wessels: *Transition Radiation Detectors.* Review. GSI Helmholtzzentrum für Schwerionenforschung, Darmstadt, Germany. Institut für Kernphysik, Universität Münster, Germany. European Organization for Nuclear Research CERN, Geneva, Switzerland. 2011.

[Bai09] R. Bailhache: *Calibration of the ALICE Transition Radiation Detector and study of Z^0 and heavy quark production in pp collisions at the LHC.* PhD thesis, Technische Universität Darmstadt, 2009.

[Bai14] R. Bailhache: Personal communication.

[Bat07] B. Bathen: *Aufbau eines Triggers für Testts der ALICE-TRD Supermodule mit kosmischer Strahlung.* Diploma thesis, Westfälische Wilhelms-Universität Münster, 2007.

[BC03] L. Betev, P. Chochula: *Definition of the ALICE Coordinate System and Basic Rules for Subdetector Components Numbering.* ALICE Offline, Geneva, 2003.

[Bet12] A. Bettini: *Introduction to Elementary Particle Physics.* Cambridge University Press, New York, 2012.

[BS64] M. J. Berger, S. M. Seltzer: *Tables of Energy Losses and Ranges of Electrons and Positrons.* National Bureau of Standards and NASA, Washington D.C., 1964. URL: `http://ntrs.nasa.gov/archive/nasa/casi.ntrs.nasa.gov/19650002905.pdf`.

[CERN13] CERN Document Server: *LHC Experiments. ALICE.* URL: `https://cds.cern.ch/collection/ALICE?ln=de`.

[CERN14] CERN: *The Large Hadron Collider.* URL: `http://home.web.cern.ch/topics/large-hadron-collider`.

[CERNPub] CERN press office: *First three-year LHC running period reaches a conclusion.* CERN, Geneva, 2013. URL: `http://press.web.cern.ch/press-releases/2013/02/first-three-year-lhc-running-period-reaches-conclusion`

[Dem10] W. Demtröder: *Experimentalphysik 4. Kern-, Teilchen- und Astrophysik.* 3rd Edition, Springer, 2010.

[ESA00] V. Egorytchev, V. Saveliev, S.J. Aplin: *Particle identification via transition radiation and detectors.* Moscow Engineering and Physics Institute, Russia. University of Portsmouth, Portsmouth, United Kingdom.

[Fas08] M. Fasel: *Hadronenproduktion in Proton-Proton Kollisionen.* Master Thesis, Technische Universität Darmstadt, Gesellschaft für Schwerionenforschung, 2008.

[Gat10] H. Gatz: *Calibration and Alignment of ALICE TRD Super Modules Using Cosmic Ray Data.* Diploma thesis, Westfälische Wilhelms-Universität Münster, 2010.

[Gru05] C. Grupen: *Astroparticle Physics.* Springer, Berlin Heidelberg, 2005.

[Hub11] S. Huber: *Ausrichtung des ALICE Übergangsstrahlungsdetektors sowie Zweiteilchenintensitätsinterferometrie identischer Pionen aus p+p Kollisionen bei LHC Energien von 900 GeV und 7.0 TeV.* PhD thesis, Technische Universität Darmstadt, 2011.

[KBö04] C. Klein-Bösing: *Production of Neutral Pions and Direct Photons in Ultra-Relativistic Au + Au Collisions.* PhD thesis, Westfälische Wilhelms-Universität Münster, 2004.

[Kno89] G. F. Knoll: *Radiation Detection and Measurement.* Wiley CH, 2nd Edition, Ann Arbor, Michigan, 1989.

[LHC08a] : L. Evans, P. Bryant: *LHC Machine. The CERN Large Hadron Collider: Accelerator and Experiments..* JINST 3 S08001.

[LHC08b] : L. Evans, P. Bryant: *The ATLAS Experiment at the CERN Large Hadron Collider. The CERN Large Hadron Collider: Accelerator and Experiments..* JINST 3 S08003.

[LHC08c] : L. Evans, P. Bryant: *The CMS experiment at the CERN LHC. The CERN Large Hadron Collider: Accelerator and Experiments..* JINST 3 S08004.

[LHC08d] : L. Evans, P. Bryant: *The LHCb Detector at the LHC. The CERN Large Hadron Collider: Accelerator and Experiments..* JINST 3 S08005.

[LHC08e] : L. Evans, P. Bryant: *The LHCf detector at the CERN Large Hadron Collider. The CERN Large Hadron Collider: Accelerator and Experiments..* JINST 3 S08006.

[LHC08f] : L. Evans, P. Bryant: *The TOTEM Experiment at the CERN Large Hadron Collider. The CERN Large Hadron Collider: Accelerator and Experiments..* JINST 3 S08006.

[PDG13a] J. Beringer et al. (Particle Data Group): *Cosmic Rays. Review of Particle Phyics.* Phys. Rev. D86, 010001 (2012) and 2013 partial update for the 2014 edition. URL: `http://pdg.lbl.gov/2013/reviews/rpp2013-rev-cosmic-rays.pdf`.

[PDG13b] J. Beringer et al. (Particle Data Group): *Light Unflavored Mesons. Review of Particle Physics.* Phys. Rev. D86, 010001 (2012) and 2013 partial update for the 2014 edition. `http://pdg.lbl.gov`.

[PRSZ09] B. Povh, K. Rith, C. Scholz, F. Zetsche: *Teilchen und Kerne*. 8th Edition, Springer, 2009.

[Ras10] T. B. Rascanu: *An Implementation of the ALICE TRD Online Reconstruction* . Diploma thesis, Goethe-Universität Frankfurt am Main, 2010.

[Roo07] R. Brun, F. Rademakers: *Root - User's Guide*. Geneva, 2007.

[Sch98] J. Schnapka: *Doppelspurerkennung unter Verwendung der Kathodenauslese am ZEUS-Übergangsstrahlungsdetektor*. Diploma Thesis. Bonn, 1998.

[Sic09] E. Sicking: *Alignment of ALICE TRD Modules Using Cosmic Ray Data*. Diploma thesis, Westfälische Wilhelms-Universität Münster, 2009.

[Wil04] A. Wilk: *Elektronen-Pionen-Separation im ALICE TRD*. Diploma thesis, Westfälische Wilhelms-Universität Münster, 2010.

[Wil10] A. Wilk: *Particle Identification Using Artificial Neural Networks with the ALICE Transition Radiation Detector*. PhD thesis, Westfälische Wilhelms-Universität Münster, 2010.

Danksagung

An dieser Stelle möchte ich all den Menschen danken, die mich während meines bisherigen Studiums und beim Schreiben dieser Bachelorarbeit unterstützt haben.

Zunächst danke ich Herrn Prof. Dr. J. P. Wessels für die Aufnahme in die Arbeitsgruppe und die interessante Themenstellung. Einen besonderen Dank möchte ich auch für Professor Wessels freundliche Unterstützung bei der Bewerbung für ein Auslandspraktikum aussprechen, zu deren Gelingen er maßgeblich beigetragen hat.

In diesem Zusammenhang möchte ich auch Prof. Dr. C. Weinheimer für die Unterstützung meiner Auslandspläne und die Übernahme des Zweitgutachtens danken.

Mein ausgesprochener Dank gilt Dr. Bastian Bathen für sein großes Engagement, seine Geduld und weitreichende Expertise bei der Betreuung dieser Bachelorarbeit. Bei Fragen war er stets die erste Anlaufstelle und nahm sich immer Zeit, um bei der Lösung auftretender Schwierigkeiten zu helfen. Seine Anregungen und Korrekturen waren für den Erfolg dieser Arbeit von wesentlicher Bedeutung.

Für die Beantwortung zahlreicher Fragen bezüglich der Gain- und Driftgeschwindigkeits-Kalibrierung danke ich Dr. Raphaëlle Bailhache.

Der gesamten Arbeitsgruppe möchte ich für das freundliche Willkommen danken, insbesondere Daniel Mühlheim, Hendrik Poppenborg und Philipp Kähler für die angenehme Arbeitsatmosphäre in der TRD-Halle. Katharina Garner und Pablo Sarazá Canflanca gilt mein Dank für gegenseitige Hilfe beim fortwährenden Kampf mit ROOT und für die gute Stimmung im Büro.

Alessandro Zannotti und Lorenz Josten gebührt großer Dank für das Durchsehen meiner Arbeit mitsamt zahlreicher Korrekturen und stilistischer Anregungen.

Auch Juliane danke ich für das gewissenhafte Durchsehen und den sprachlichen Feinschliff meiner Arbeit. Genau so, wie du mit mir Erfolge feierst, motivierst du mich, auch bei Schwierigkeiten weiterzumachen.

Zuletzt möchte ich von Herzen meinen Eltern, Beate und Volker Wittweg, und meiner Großmutter, Ursula Wehrmann, danken, die mir mit ihrem Vertrauen, ihrem Zuspruch und auch ihrer finanziellen Unterstützung das Studium erst ermöglicht haben.

Eigenständigkeitserklärung

Hiermit versichere ich, dass ich die vorliegende Arbeit mit dem Titel **Gas Gain Calibration of an ALICE TRD Supermodule Using Cosmic Rays** selbstständig verfasst habe, und dass ich keine anderen Quellen und Hilfsmittel als die angegebenen benutzt habe und dass die Stellen der Arbeit, die anderen Werken – auch elektronischen Medien – dem Wortlaut oder Sinn nach entnommen wurden, auf jeden Fall unter Angabe der Quelle als Entlehnung kenntlich gemacht worden sind.

Münster, den 24.06.2014

Christian Wittweg